Electronic Structure Characterization of Molecular Interactions in Clathrate Hydrates

A

thesis submitted

in partial fulfillment of the requirements for the degree of

DOCTOR OF PHILOSOPHY

by

K. R. Ramya

Roll No.: 20103060

Indian Institute of Science Education and Research, Pune

2014

Certificate

Certified that the work incorporated in the thesis entitled "*Electronic Structure Characterization of Molecular Interactions in Clathrate Hydrates*", submitted by *K. R. Ramya* was carried out by the candidate, under my supervision. The work presented here or any part of it has not been included in any other thesis submitted previously for the award of any degree or diploma from any other University or institution.

Date:

Dr. Arun Venkatnathan

(Supervisor)

Declaration

I declare that this written submission represents my ideas in my own words and where others' ideas have been included, I have adequately cited and referenced the original sources. I also declare that I have adhered to all principles of academic honesty and integrity and have not misrepresented or fabricated or falsified any idea/data/fact/source in my submission. I understand that violation of the above will be cause for disciplinary action by the Institute and can also evoke penal action from the sources which have thus not been properly cited or from whom proper permission has not been taken when needed.

Date: **K. R. Ramya**

Dedicated to my parents

Acknowledgement

I acknowledge Indian Institute of Science Education and Research, Pune for providing high quality research environment and graduate fellowship. I am grateful to Prof. K. N. Ganesh, Director, IISER Pune. I am deeply indebted to my thesis advisor Dr. Arun Venkatnathan for his enduring guidance, scholarly inputs and his consistent encouragement I received throughout the research work. The constant support from him has enhanced my communication skills, teaching ability, scientific writing and made me an independent thinker.

I thank my RAC members - Dr. Arun Venkatnathan, Dr. Arnab Mukherjee and Dr. Kumar Vanka for their scientific advice and guidance provided at every stage of my research work. I am grateful to Dr. Mukul Kabir for constructive discussions, great support, valuable suggestions and teaching new techniques. I thank Dr. Prasenjith Ghosh, Dr. Anirban Hazra, Dr. Pavan Kumar and Dr. Boomi Shankar for their help at various stages of my research.

I thank my colleagues Anurag, Minal, Praveen and Rakesh for their constant support, suggestions, care and affection. I would like to thank Saikat, Nandha Kumar, Sappati Subrahmanyam, and Adwittey for helping me at various stages of research. I thank all my computational colleagues who made the research environment enjoyable. I am fortunate to have friends like Padma, Smita, Resmi, Mayur, Abhishek and Mandar who constantly supported me a lot.

I thank Neeta, Suresh, Sachin, Abhijeet and Pradeep for IT support. I thank Dr. Umeshareddy and Anuradha for providing us excellent library support throughout my research work. I thank specially Dr. V. S. Rao, Anil Jadhav, Prabhas, Nivruti, Mayuresh, Suvarna, and Mahesh for their administrative support.

My research career would have not been possible without the active support of my family. I thank my mother, father and sister for their love, support and encouragement all

the time. I owe a lot to my parents, who encouraged and helped me at every stage of my personal and academic life, and longed to see this achievement come true.

This thesis would have not been possible without the help and support by many individuals whom I met during my PhD life at IISER, Pune. I would like to thank American Chemical Society, American Physics Society, Science, Nature, Proceedings of National Academy of Science for permissions to include tables and photographs from copyrighted articles.

IISER, PUNE **K. R. Ramya**

List of Publications

1. **K. R. Ramya** and Arun Venkatnathan,
Stability and Reactivity of Methane Clathrate Hydrates: Insights from Density Functional Theory,
J. Phys. Chem. A **116**, 7742 (2012).

2. **K. R. Ramya**, G. V. Pavan Kumar and Arun Venkatnathan,
Raman spectra of vibrational and librational modes in methane clathrate hydrates using density functinal theory,
J. Chem. Phys **136**, 174305 (2012).

3. **K. R. Ramya** and Arun Venkatnathan,
Vibrational Raman spectra of hydrogen clathrate hydrates from density functional theory,
J. Chem. Phys **138**, 124305 (2013).

4. **K. R. Ramya** and Arun Venkatnathan,
Density Functional Theory study of oxygen clathrate hydrates,
Indian Journal of Chemistry A **52A**, 1061 (2013).

5. **K. R. Ramya** and Arun Venkatnathan,
Characterization of interaction energy and vibrational Raman spectra of nitrogen clathrate hydrates,
Comput. Theor. Chem. **1023**, 1, (2013).

6. **K. R. Ramya**, Rohit Kumar and Arun Venkatnathan,
Energy and spectral characteristics of hydrogen occupied pure and tetrahydrofuran doped water cages,
Comput. Theor. Chem. **1039**, 28, (2014).

7. **K. R. Ramya**, Arun Venkatnathan and Mukul Kabir,
Understanding the microscopic mechanism of methane clathrate hydrates,
(Manuscript under preparation).

8. **K. R. Ramya**, Praveen Kumar, Ashish Kumar and Arun Venkatnathan,
Interplay of phase separation, tail aggregation, micelle formation in the nanostructured organization of hydrated imidazolium ionic liquid,
(Under Revision).

9. **K. R. Ramya**, Praveen Kumar and Arun Venkatnathan,
Effect of anionic size and temperature dependence on the structural and dynamical properties on 1-hexyl, 3-methyl imidazolium ionic liquid,
(Manuscript under preparation).

10. **K. R. Ramya**, Praveen Kumar and Arun Venkatnathan,
Atomistic simulation study on dynamics of hydrated imidazolium ionic liquid,
(Manuscript under preparation).

Contents

Certificate i

Declaration ii

Acknowledgement iv

List of Publications vi

List of Figures xii

List of Tables xvi

Abbrevations xix

Abstract xx

1 Introduction **1**

1.1 Clathrate hydrates: An Overview 1

1.2 Crystallographic structures and stability 2

1.2.1 Structure 2

1.2.2 Molecular structure of clathrate hydrates 4

1.3 Brief description of previous literature 5

1.4 Theoretical background 7

1.4.1 Density Functional Theory (DFT) 9

1.4.1.1 The Local Density Approximation (LDA) 10

1.4.1.2 The Generalized Gradient Approximation (GGA) . . . 10

1.4.2 Reaction mechanism pathways: Application of numerical methods 12

1.4.2.1 Nudged Elastic Band method 13

1.4.3 Free Energy 15

1.4.4 Reactivity indices . . . 16
1.4.5 Vibrational Raman Spectra . . . 17
1.5 Methodology . . . 17
1.5.1 Calculation details . . . 17
1.6 Outline of this work . . . 18

2 Stability and Reactivity of methane clathrate hydrates 21
2.1 Introduction . . . 21
2.2 Computational details . . . 24
2.3 Results and Discussion . . . 26
2.3.1 Cage radius . . . 26
2.3.2 Dependence of interaction energy on Basis sets . . . 26
2.3.3 Effect of pressure and temperature on thermodynamic stability . . . 29
2.3.4 Reactivity Indices . . . 30
2.4 Conclusions . . . 31

3 Raman spectra of vibrational and librational modes in methane clathrate hydrates 33
3.1 Introduction . . . 33
3.2 Results and Discussion . . . 35
3.2.1 Effect of functionals on spectral properties . . . 35
3.2.2 High frequency region . . . 35
3.2.3 Mid frequency region . . . 38
3.2.4 Low frequency region . . . 39
3.3 Conclusions . . . 41

4 Reaction mechanism of methane clathrate hydrates 43
4.1 Introduction . . . 43
4.2 Computational details . . . 44
4.3 Results and discussion . . . 44

4.3.1 Structure and Energetics 44
4.3.2 Activation energy of diffusion of the CH_4 in 5^{12} and $5^{12}6^2$ cages . 46
4.3.2.1 Diffusion of CH_4 via the pentagonal gate of 5^{12} and $5^{12}6^2$ cages 47
4.3.2.2 Diffusion of the CH_4 via the hexagonal gate of the $5^{12}6^2$ cage 47
4.3.3 Activation energy of diffusion of CH_4 in fused water cages 51
4.4 Conclusions 53

5 Hydrogen storage in pure and tetrahydrofuran doped clathrate hydrates 55
5.1 Introduction 55
5.2 Computational details 57
5.3 Results and Discussion 61
5.3.1 Interaction energy 61
5.3.2 Free energy 62
5.4 Conclusions 66

6 Raman spectroscopy of pure and tetrahydrofuran doped hydrogen clathrate hydrates 67
6.1 Introduction 67
6.2 Computational details 69
6.3 Results and Discussion 70
6.3.1 Geometry 70
6.3.2 Spectral properties of single occupancy 70
6.3.2.1 Effect of dispersion on spectral properties 70
6.3.2.2 High frequency modes 71
6.3.2.3 Mid and low frequency modes 73
6.3.3 Spectral properties on multiple occupancy 75
6.3.3.1 H-H symmetric stretch 76

6.3.3.2 Water vibrational modes . . . 77
6.3.4 Deformation Energies . . . 80
6.4 Conclusions . . . 82

7 Interaction energy and vibrational Raman spectra of nitrogen clathrate hydrates 83
7.1 Introduction . . . 83
7.2 Computational details . . . 84
7.3 Results and discussion . . . 85
7.3.1 Interaction Energy . . . 85
7.3.2 Vibrational Raman Spectra . . . 87
7.4 Conclusions . . . 89

8 Interaction energy and vibrational Raman spectra of oxygen clathrate hydrates 90
8.1 Introduction . . . 90
8.2 Computational details . . . 91
8.3 Results and discussion . . . 92
8.3.1 Interaction Energy . . . 92
8.3.2 Vibrational Raman spectra . . . 93
8.4 Conclusions . . . 96

9 Summary 97
9.1 Conclusions . . . 97
9.2 Future directions . . . 99
9.2.1 Extraction of methane from clathrate hydrates using replacement mechanism of CO_2: Insights from *ab initio* MD simulations . . . 99
9.2.2 Tuning storage capacity of hydrogen clathrate hydrates . . . 102
9.2.3 Nucleation mechanism of clathrate hydrates . . . 102
Appendix A . . . 106

Appendix B 110
Bibliography 118

List of Figures

1.1 Structural forms and cages of clathrate hydrate structures I, II and H. (Adapted from Struzhkin et. al. [16]. Copyright (2014) from American Chemical Society) . . . 3

1.2 Crystal structure of Bernal-Fowler ice Ih. Red (white) balls give the positions of the oxygen (hydrogen) atoms. The crystallographic c-axis is in the vertical direction. (Adapted from Isaacs et. al. [20]. Copyright (2014) from American Physics Society.) . . . 5

1.3 Schematic representation of hydrogen bonding interactions in cages of clathrate hydrates. . . . 13

1.4 Schematic representation of Minimum Energy Pathway. . . . 15

1.5 Schematic representation of sI hydrate lattice and its constituent polyhedral water cages. . . . 18

2.1 Optimized structures of 5^{12}, $5^{12}6^2$, $5^{12}CH_4$ and $5^{12}6^2CH_4$ cages. . . . 25

3.1 The symmetric and asymmetric stretch vibrations of 5^{12} and $5^{12}CH_4$ cages. 37

3.2 The symmetric and asymmetric stretch vibrations of $5^{12}6^2$ and $5^{12}6^2CH_4$ cages. . . . 37

3.3 Mid-frequency Raman spectra of 5^{12} and $5^{12}CH_4$ cages. . . . 40

3.4 Mid-frequency Raman spectra of $5^{12}6^2$ and $5^{12}6^2CH_4$ cages. . . . 40

3.5 Low frequency Raman spectra of 5^{12} and $5^{12}CH_4$ cages. . . . 41

3.6 Low frequency Raman spectra of $5^{12}6^2$ and $5^{12}6^2CH_4$ cages. . . . 42

4.1 Schematic representation of reactants and products. 46
4.2 Schematic representation of diffusion of CH_4 via the pentagonal and hexagonal gate. 46
4.3 Activation energy of diffusion of CH_4 via the pentagonal gate of the 5^{12} cage. 48
4.4 Activation energy of diffusion of CH_4 via the pentagonal gate of the $5^{12}6^2$ cage. 49
4.5 Activation energy of diffusion of CH_4 via the hexagonal gate of the $5^{12}6^2$ cage. 50
4.6 Schematic representation of fused water cages. 52
4.7 Activation energy of diffusion of CH_4 in fused water cages. 53

5.1 Phase diagram and stability regions of pure H_2 hydrate, pure THF hydrate and binary H_2/THF hydrate. (Adapted Florusse et. al. [163]. Copyright (2014) from Science) 56
5.2 Structure of multiple occupancy of H_2 in the 5^{12} cage. 59
5.3 Structure of multiple occupancy of H_2 in $5^{12}6^4$ cages. 59
5.4 Structure of multiple occupancy of THF in pure and H_2 doped $5^{12}6^4$ cages. 60
5.5 Change in free energies of formation of hydrogen occupied (a, d) 5^{12} cage, (b, e) $5^{12}6^4$ cage, (c, f) THF doped $5^{12}6^4$ cage. 65

6.1 Symmetric stretch of pure and THF doped 5^{12} and $5^{12}6^4$ cages. 73
6.2 The symmetric and asymmetric stretch vibrations in a) 5^{12} and $5^{12}(H_2)$ cages, b) $5^{12}6^4$, $5^{12}6^4(H_2)$ and $5^{12}6^4(H_2)$.THF cages. 74
6.3 Mid-frequency and low frequency Raman spectra in a) 5^{12} and $5^{12}(H_2)$ cages, b) $5^{12}6^4$, $5^{12}6^4(H_2)$ and $5^{12}6^4(H_2)$.THF cages. 75
6.4 Hydrogen bond length vs. Raman vibrational H-H symmetric stretching frequency. 77
6.5 Statistically averaged Raman spectra of $5^{12}(H_2)_{n=0-2}$ cages. 78

6.6 Statistically averaged Raman spectra of $5^{12}6^4(H_2)_{n=0-4}$ and $5^{12}6^4(H_2)_{n=1,2}$.THF cages. 78

7.1 Structure of $5^{12}(N_2)_{n=1,2}$ and $5^{12}6^4(N_2)_{n=1-3}$ cages. 85

7.2 N-N symmetric stretch, asymmetric stretch, symmetric stretch and bending overtone modes of water molecules in $5^{12}(N_2)_{n=1,2}$ and $5^{12}6^4(N_2)_{n=1-3}$ cages. 87

8.1 Optimized structures of $5^{12}(O_2)$, and $5^{12}(O_2)_2$ cages. 92

8.2 Optimized structures of $5^{12}6^4(O_2)$, $5^{12}6^4(O_2)_2$ and $5^{12}6^4(O_2)_3$ cages. . . . 92

8.3 Vibrational Raman spectra in $5^{12}(O_2)$ and $5^{12}(O_2)_2$ cages. 94

8.4 Vibrational Raman spectra in $5^{12}6^4(O_2)$, $5^{12}6^4(O_2)_2$ and $5^{12}6^4(O_2)_3$ cages. 95

9.1 Schematic diagram of CH_4 + C_2H_6 hydrate replaced with CO_2. (Adapted from Park et. al. [229]. Copyright (2014) from Proc. Natl. Acad. Sci.) . . 101

9.2 A snapshot of the 2x2x2 unit cell replica of the sI CO_2L/CH_4S mixed clathrate hydrates left. A close-up of a small cage with the CH_4 guest and large cage with CO_2 guest are also shown right. The oxygen atoms of the clathrate water framework are connected by lines. (Adapted from Dorman et. al. [231]. Copyright (2014) from American Physics Society) 101

9.3 H_2 gas content as a function of THF concentration and schematic diagram of H_2 distribution in the cages of THF+H_2 hydrate. In region III, H_2 gas is stored only in small cages and THF is stored in large cages. In region I and II H_2 can be stored in small and large cages. (Adapted from Lee et. al. [164]. Copyright (2014) from Nature) 103

9.4 (a-f) Snapshots at different times from one nucleation trajectory. Water molecules belonging to the largest cluster are shown in red and white (for oxygen and hydrogen, respectively), and those in the second largest cluster are shown in blue. The orange spheres in panel a are methane molecules. (g-i) Snapshots in g, h, and i panels are the same as d, e, and f shown in a different rendering. The largest cluster is shown in red and the second largest cluster is in blue. (Adapted from Sarupria et. al. [234]. Copyright (2014) from American Chemical Society) 104

List of Tables

1.1 Structural features of clathrate hydrates [7] 4

2.1 Radius (Å) of the 5^{12}, $5^{12}6^2$, $5^{12}CH_4$ and $5^{12}6^2CH_4$ cages. 26
2.2 Interaction energies (kcal/mol) calculated from total energies using the M05-2X functional. 28
2.3 Interaction energies from DFT and MP2 methods. 29
2.4 ΔH (kcal/mol), TΔS (kcal/mol), ΔG (kcal/mol) using the M05-2X functional and cc-pVQZ basis set. 30
2.5 Electro-negativity (χ), Hardness (η), and Electro-philicity (ω) using the M05-2X functional and cc-pVQZ basis set. 31

3.1 Raman peak assignments (cm^{-1}) in 5^{12}, $5^{12}CH_4$, $5^{12}6^2$ and $5^{12}6^2CH_4$ cages (reference: free H_2O and free CH_4). 38

4.1 Average bond distances (Å) and bond angles (°) for the reactant and products. Standard deviations are given in parenthesis. 45
4.2 Adsorption energies (kcal/mol) of CH_4 in 5^{12} and $5^{12}6^2$ cages. 45
4.3 Structural properties of the pentagonal gate in the 5^{12} cage. 48
4.4 Structural properties of the pentagonal gate in the $5^{12}6^2$ cage. 49
4.5 Structural properties of the hexagonal gate in the $5^{12}6^2$ cage. 50
4.6 Activation energy (kcal/mol) of diffusion of CH_4 in 5^{12} and $5^{12}6^2$ cages. . 51
4.7 Activation energy (kcal/mol) of diffusion of CH_4 in single and fused cages. 53

5.1 Average interaction energy (includes BSSE and ZPVE) in kcal/mol for each occupancy of hydrogen in 5^{12} and $5^{12}6^4$ cages. ZPVE (kcal/mol) contributions to interaction energy in parenthesis. 63

5.2 Weight percentage of hydrogen in pure and THF doped hydrogen clathrate hydrates. 64

6.1 Raman peak assignments (cm^{-1}) in 5^{12}, $5^{12}(H_2)$, $5^{12}6^4$, $5^{12}6^4(H_2)$ and $5^{12}6^4(H_2)$.THF cages (reference: isolated H_2). Frequencies are calculated using the B97-D and B97-1 functionals (in parenthesis). 72

6.2 Raman peak assignments (cm^{-1}) in $5^{12}6^4$.THF and $5^{12}6^4(H_2)$.THF cages. . 76

6.3 Statistically averaged Raman peak assignments (cm^{-1}) in $5^{12}(H_2)_{n=0-2}$, $5^{12}6^4(H_2)_{n=0-4}$ and $5^{12}6^4(H_2)_{n=1,2}$.THF cages. (Values in parenthesis represent the scaled frequencies only for the H-H symmetric stretch). 79

6.4 Deformation energies (kcal/mol) of pure and THF doped 5^{12} and $5^{12}6^4$ cages of hydrogen clathrate hydrates. 81

7.1 Interaction energy (kcal/mol) and Deformation energy (kcal/mol). Contributions from ZPVE to interaction energy is shown in parenthesis. . . . 86

7.2 Raman peak assignments (cm^{-1}) in $5^{12}(N_2)_{n=0-2}$ and $5^{12}6^4(N_2)_{n=0-3}$ cages. 88

8.1 Interaction energies (IE) (kcal/mol) of varying occupancies of O_2 molecules in 5^{12} and $5^{12}6^4$ cages. 93

8.2 Raman frequencies (cm^{-1}) peak assignment in the $5^{12}(O_2n = 0 - 2)$ and $5^{12}6^4(O_2)_{n=0-3}$ cages (reference: isolated O_2). 95

B2-1 Total energies (a.u.) using the DFT/M05-2X functional. 110

B3-1 Raman frequencies (cm^{-1}) peak assignments from B97-D and M05-2X (in parenthesis). 111

B5-1 Total energies (a.u.) from five structures of 5^{12} and $5^{12}6^4$ cages. 112

B5-2 Interaction energy (includes BSSE and ZPVE) in kcal/mol for each occupancy of hydrogen in 5^{12} and $5^{12}6^4$ cages. For each cage, structures S1 - S5 differ in the orientation of protons. ZPVE (kcal/mol) contributions to interaction energy in parenthesis. 113
B6-1a Raman peak assignments (cm^{-1}) of 5^{12} cage. 114
B6-1b Raman peak assignments (cm^{-1}) of $5^{12}(H_2)$ cage. 114
B6-1c Raman peak assignments (cm^{-1}) of $5^{12}(H_2)_2$ cage. 114
B6-1d Raman peak assignments (cm^{-1}) of $5^{12}6^4$ cage. 115
B6-1e Raman peak assignments (cm^{-1}) of $5^{12}6^4(H_2)$ cage. 115
B6-1f Raman peak assignments (cm^{-1}) of $5^{12}6^4(H_2)_2$ cage. 115
B6-1g Raman peak assignments (cm^{-1}) of $5^{12}6^4(H_2)_3$ cage. 116
B6-1h Raman peak assignments (cm^{-1}) of $5^{12}6^4(H_2)_4$ cage. 116
B6-1i Raman peak assignments (cm^{-1}) of $5^{12}6^4(H_2)$.THF cage. 116
B6-1j Raman peak assignments (cm^{-1}) of $5^{12}6^4(H_2)_2$.THF cage. 117

Abbreviations

HF	:	Hartree-Fock
MP2	:	Möller-Plesset Perturbation Theory (2nd order)
DFT	:	Density Functional Theory
AIMD	:	*Ab initio* Molecular Dynamics
MD	:	Molecular Dynamics
NEB	:	Nudge Elastic Band method
MEP	:	Minimum Energy Pathway
TS	:	Transition State
PAW	:	Projector Augmented Wave method
5^{12}	:	Dodecahedron
$5^{12}6^{2}$	:	Tetrakaidecahedron
$5^{12}6^{4}$	:	Hexakaidecahedron
$5^{12}6^{8}$	:	Icosahedron
$4^{3}5^{6}6^{3}$	:	Irregular dodecahedron
χ	:	Electronegativity
η	:	Hardness
ω	:	Electrophilicity
IE	:	Interaction Energy
BSSE	:	Basis Set Superposition Error
ZPVE	:	Zero Point Vibrational Energy

Abstract

Clathrate hydrates are crystalline solids which consist of gas molecules encapsulated in various polyhedral water cages. The formation of these hydrates requires conditions of low temperature and high pressure. These hydrates have potential applications in energy storage, carbon dioxide sequestration, hydrogen storage and biomedical applications. Various molecules such as Ar, Kr, oxygen, nitrogen, carbon monoxide, methane, ethane, propane and carbon dioxide are known to exist in the form of clathrate hydrates. The thesis focuses on the structure, energy, stability, mechanism of formation and spectral properties of cages of various clathrate hydrates using Density Functional Theory (DFT). Some examples are methane, hydrogen, nitrogen and oxygen clathrate hydrates.

Methane clathrate hydrates are known to have potential applications as an alternate source of energy due to its abundance. The characterization of interaction energy, thermodynamic stability and vibrational Raman spectra with encapsulation of methane in various cages of clathrate hydrates is presented. The dependence of interaction energies on basis sets and functionals is also discussed. The mechanism of diffusion of methane in various cages is characterized using the Climbing Image Nudged Elastic Band method. The activation energy of diffusion in these cages and fused cages is also examined. Clathrate hydrates containing hydrogen are potential sources of energy, where addition of tetrahydrofuran reduces the thermodynamic conditions of formation of hydrogen clathrate hydrates. The stability, hydrogen storage capacity and vibrational Raman spectra of multiple occupancy of hydrogen molecules in pure and tetrahydrofuran doped cages of hydrogen clathrate is calculated and compared with experiments. The energy and spectral properties of cages of nitrogen and oxygen clathrate hydrates is also presented. A characterization of methane replacement by carbon dioxide in the cages of clathrate hydrates using *Ab initio* Molecular Dynamics simulations and an examination of hydrogen clathrate hydrate formation and nucleation is presented as one of the future activities.

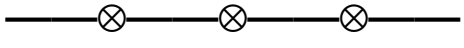

Chapter 1

Introduction

1.1 Clathrate hydrates: An Overview

Clathrate hydrates are crystalline solids which consist of gas molecules encapsulated in various polyhedral water cages [1–9]. These hydrates are formed when water and gas molecules react at low temperature and high pressure [7, 8]. During this reaction, water molecules crystallize into a network of hydrogen-bonded cages in which various gas molecules like CH_4, C_2H_6, CO_2 etc., are encapsulated. Clathrate hydrates was first discovered by Humphrey Davy and Faraday [10] in 1810, when the authors observed that an aqueous solution of chloride transformed into a crystalline solid during cooling. However, interest in clathrate hydrates received attention only in 1934, after its discovery as an obstructive byproducts in oil production pipelines by Hammerschimdt [11]. Research in clathrate hydrates intensified after the discovery of large deposits of methane clathrate hydrates by Makogon [12] in the Siberian permafrost regions. Based on current energy requirements, methane clathrate hydrates could provide energy for the entire world for the next 200 years [7]. However, the dissociation of these hydrates could lead to serious impact on global warming and affect in climate change [2, 13]. Clathrate hydrates have also been explored as a possible hydrogen storage material, where H_2 molecules can be stored in various water cages to form hydrogen clathrate hydrates. Hydrogen clathrate hydrates have been synthesized and characterized by several experiments. However, its ability to serve as a promising source of energy still continues to pose challenges due to its forma-

tion at extreme thermodynamic conditions. Clathrate hydrates have also been considered as materials for carbon dioxide (CO_2) sequestration. Further, clathrate hydrates consisting of gas molecules such as Ar, Kr, O_2, N_2, CO hydrates have also been synthesized and characterized for several applications. For example, Ar, Kr and Xe clathrate hydrates have been used as a tracer to detect molecular, elemental and isotopic composition of the atmosphere [14]. CO serves as a therapeutic agent to treat sickle cell disease (SCD), systemic inflammation and cardiovascular diseases [7]. The encapsulation of CO in clathrate hydrates could be a promising alternative for storage and delivery of CO for biomedical applications. In the next section, the structural characteristics of clathrate hydrates is presented.

1.2 Crystallographic structures and stability

1.2.1 Structure

Clathrate hydrate structures was first characterized by von Stackelberg and co-workers (in the late 1940s and 1950s) using X-ray diffraction studies [15]. Structurally, the naturally occurring hydrates are divided into three categories - sI, sII and sH. A schematic representation of these structures (sI, sII and sH) with its constituent building blocks (polyhedral water cages) are shown in Figure **1.1**. As seen in Figure **1.1**, the mathematical representation of polyhedral water cages (5^{12}, $5^{12}6^2$, $5^{12}6^4$, $4^35^66^3$ and $5^{12}6^8$) shows oxygen atoms at the vertices of these cages. The structural features of these clathrate hydrates are shown in Table **1.1**. The sI hydrate lattice consist of two 5^{12} (dodecahedron water cage consists of 20 water molecules with 12 pentagonal faces) and six $5^{12}6^2$ (tetrakaidecahedron water cage consists of 24 water molecules which have 12 pentagonal faces and 2 hexagonal faces) interconnected cages. The sI hydrate is a cubic lattice with a space group Pm3n and a lattice constant **a** ~ 12.0 Å. The sI hydrate lattice can encapsulate gas molecules with vdW diameters between 4.2 Å and 6 Å. Examples of such gas molecules are CH_4, C_2H_6, CO_2 and H_2S. The sII hydrate lattice consist of sixteen 5^{12} cages and eight $5^{12}6^4$ cages (hexakaidecahedral water cage consists of 28 water molecules with 12 pentagonal

faces and 4 hexagonal faces). The sII hydrate is a cubic lattice with a space group Fd3m and lattice constant **a** ~ 17.3 Å. The sII hydrate lattice can encapsulate gas molecules with vdW diameter below 4.2 Å and between 6 Å and 7 Å. For example, N_2, O_2, H_2, C_3H_8 and C_4H_{10} can form sII hydrate lattice. The sH hydrate lattice consist of three 5^{12} cages, two $4^3 5^6 6^3$ cages (irregular distorted dodecahedron water cage consists of 20 water molecules) and one $5^{12}6^8$ cage (icosahedron water cage consists of 36 water molecules with 12 pentagonal faces and 8 hexagonal faces). The sH hydrate is a hexagonal lattice with a space group P6/mmm and lattice constants of **a** ~ 12 Å, and **c** ~ 10 Å. The sH hydrate lattice can encapsulate gas molecules with vdW diameters between 7 Å and 9 Å. For example, C_5H_{12}, $(CH_3)_3CCH_2CH_3$) or smaller molecules like CH_4, H_2S, N_2 etc. can be accommodated in a sH hydrate lattice. While, sI, sII and sH are naturally occurring structures, other hydrate structures have also been proposed by theoretical methods [17] and experiments [18].

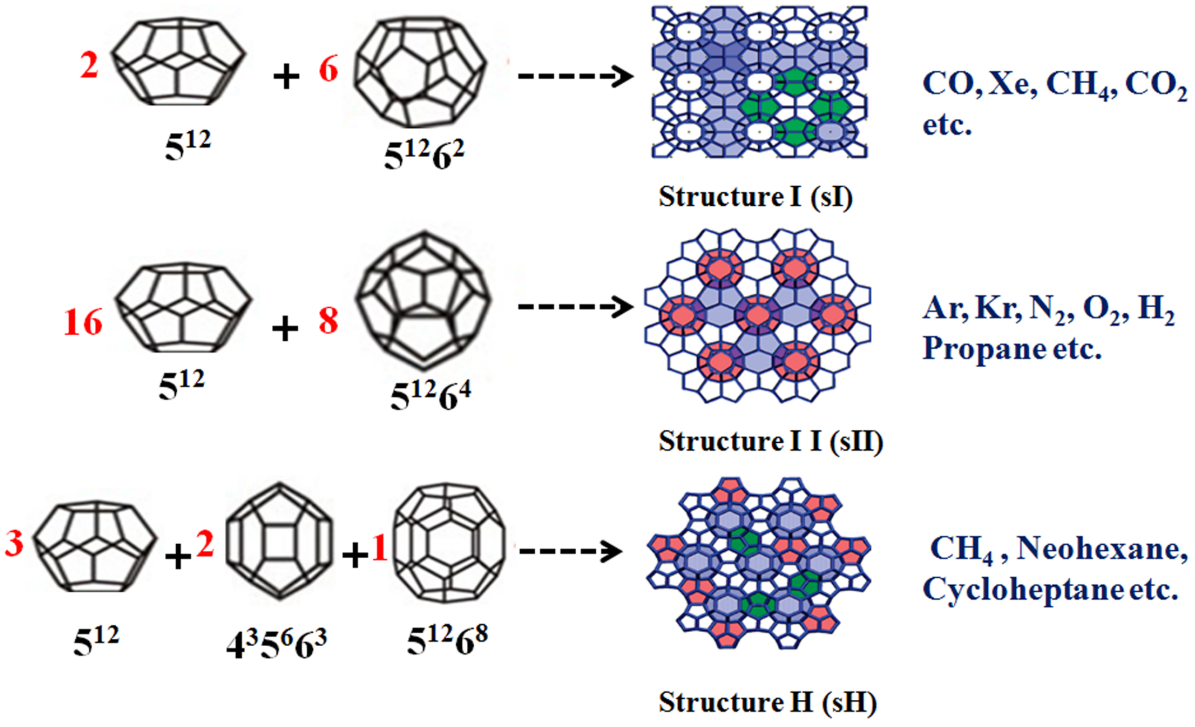

Figure 1.1: Structural forms and cages of clathrate hydrate structures I, II and H. (Adapted from Struzhkin et. al. [16]. Copyright (2014) from American Chemical Society)

Table 1.1: Structural features of clathrate hydrates [7]

Properties	**sI**		**sII**		**sH**		
Cage	Small	Large	Small	Large	Small	Medium	Large
Description	5^{12}	$5^{12}6^2$	5^{12}	$5^{12}6^4$	5^{12}	$4^35^66^3$	$5^{12}6^4$
Cages per unit cell	2	6	16	8	3	2	1
Average cage radius (Å)	3.95	4.33	3.91	4.73	3.91	4.06	5.71
Water molecules per cage	20	24	20	28	20	20	36
Water molecules per unit cell	46		136		34		

1.2.2 Molecular structure of clathrate hydrates

The structural properties of clathrate hydrates resemble Bernal and Fowler's ice rules [19]. These rules are based on a statistical model and shows the following features (see Figure 1.2):

1. Each oxygen atom is covalently bonded to two hydrogen atoms with a O-H distance of 0.95 Å.

2. The orientation of each water molecule is such that two hydrogen atoms of a water molecule will face two of the four neighbouring oxygen atoms to form a tetrahedral configuration.

3. Between two adjacent water molecules there exist only one hydrogen bonded atom which lies in the plane of oxygen atoms.

4. A large number of configurations for ice can exist due to various orientations of the non-bonded hydrogen atoms with respect to the oxygen atoms.

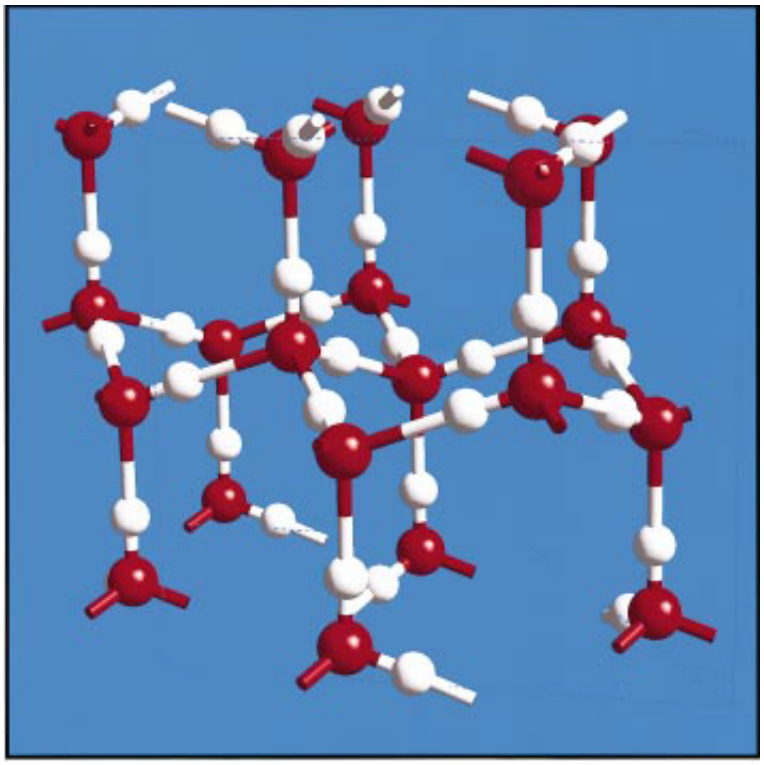

Figure 1.2: Crystal structure of Bernal-Fowler ice Ih. Red (white) balls give the positions of the oxygen (hydrogen) atoms. The crystallographic c-axis is in the vertical direction. (Adapted from Isaacs et. al. [20]. Copyright (2014) from American Physics Society.)

1.3 Brief description of previous literature

Experimental studies using Powder X-Ray Diffraction (XRD), Nuclear Magnetic Resonance spectroscopy (NMR), Raman spectroscopy techniques have been employed to determine the phase transformation, thermodynamic stability and spectral properties of clathrate hydrates. For example, Qiang et. al. [21] studied the phase transformation of CH_4 hydrates at T= 323 K and P= 880 Mpa and observed that the sI hydrate transforms to form a sH hydrate. The authors also observed that at T = 348 K and P = 960 Mpa, sH hydrate decomposes to form CH_4 and water. Sloan and co-workers [22, 23] employed Raman spectroscopy to characterize CH_4 and CO_2 clathrate hydrates and showed the occupancy of the guest molecules in different water cages obtained from the sea floor was in good agreement with measurements from the laboratory synthesized natural hydrates. Mao et. al. [24, 25] employed Raman spectroscopy to determine the storage capacity of

pure H_2 clathrate hydrates. The authors observed that the storage capacity of H_2 clathrate hydrates to be 5.3 wt%. Koh et. al. [26] employed Raman spectroscopy to determine the storage capacity hydrogen by tuning the cage dimension in clathrate hydrates. The authors observed that by tuning the cage dimension by 1%, it makes thermodynamically favourable for the double occupancy of H_2 in the 5^{12} cage. Similarly, Hallbrucker et al. [27] employed Raman spectroscopy to monitor the formation and cage occupancy of oxygen clathrate hydrates. Davidson et. al. [28] characterized CO clathrate hydrates using low temperature XRD and observed that CO is encapsulated in a sI hydrate. Desando et. al. [29] performed dielectric measurements and NMR spectroscopy. The authors observed that CO remains encapsulated in 5^{12} and $5^{12}6^2$ cages of sI hydrate. Dartois [30] characterized the stretching modes of CO clathrate hydrates using Infrared (IR) spectroscopy.

Molecular Dynamics (MD) simulations and *ab initio* calculations have also been employed to understand the microscopic mechanisms and formation of these hydrates. For example, Rodger and co-workers [31–33] performed MD simulations to study the nucleation of methane clathrate hydrates from a methane/water system. The authors could not observe the complete crystallization process since the simulation time was confined to a few nanoseconds. Hawtin et. al. [34] employed MD simulations on a methane/water interface system and concluded that nucleation proceeds via a formation of a tetrahedral network of water molecules that resembles a 5^{12} cage. Guo et. al. [35] performed MD simulations at water-methane interface and observed that the stochastic model is required as the formation and agglomeration of the water clusters was not observed. The authors performed microsecond MD simulations [36] to observe the formation of methane clathrate hydrates. Alavi et. al. [37] employed MD simulations to characterize the effect of gas molecules in the 5^{12} cage and its influence on hydrogen bonding between Tetrahydrofuran (THF) and water molecules. Uddin et. al. [38] employed MD simulations to determine the kinetics of dissociation of CH_4 and CO_2 clathrate hydrates. Hiratsuka et. al. [39] employed *ab initio* MD simulations to determine the vibrational modes of methane in sH clathrate hydrates. The authors observed that elongation of C-H bond length was larger when CH_4 was encapsulated in the $4^3 5^6 6^3$ cage, compared to the 5^{12} cage. Plat-

tner et. al. [40] employed classical and quantum dynamics to characterize the vibrational frequency shifts of H_2 clathrate hydrates. Based on spectroscopic signatures, the authors concluded that the double occupancy of H_2 in the 5^{12} cage to be unfavourable.

Ab initio calculations have also been employed to characterize the stability and occupancy of various gas molecules on the cages of clathrate hydrates. Tse et. al. [41] employed Density Functional Theory (DFT) and Möller-Plesset perturbation second order (MP2) theory to characterize the stability of H_2 clathrate hydrates. Similarly, Chattaraj et. al. [42] also investigated the storage capacity of H_2 clathrate hydrates using DFT. Kumar et. al. [43] employed the MP2 method to characterize gas-water cage interactions in various clathrate hydrates. Srivatsava et. al. [44] investigated the occupancy of CO_2 inside various cages of sI, sII and sH hydrate. The authors concluded that CO_2 uptake for the 5^{12} cage was the least favorable. Kumar et. al. [45] employed various DFT functionals and MP2 method to understand the interactions between the gas molecules with the water molecules of the cages. The authors concluded that interaction energies obtained using the BLYP-D3 functional was in agreement with the MP2 method. Cao et. al. [46] employed DFT with dispersion corrected B97-D functional to characterize the storage capacity of CH_4 and CO_2 in several cages of clathrate hydrates. In this thesis, *ab initio* methods is employed to characterize structure, energy, stability and spectral properties in the cages of various clathrate hydrates. In the next section, the theoretical background of *ab initio* methods is presented.

1.4 Theoretical background

Ab initio methods deals with the solution of the time independent and non-relativistic Schrödinger equation [47] and can be written as:

$$\hat{H}\Psi_i = E_i\Psi_i \tag{1.1}$$

Ψ_i is the wave function for any chemical system in its i^{th} state. E_i is the energy of the system in the i^{th} state. $\hat{H}$ is the Hamiltonian operator for any chemical system which

consists of M nuclei and N electrons, where:

$$\hat{H} = -\frac{1}{2}\sum_{i=1}^{N}\nabla_i^2 - \frac{1}{2}\sum_{A=1}^{M}\frac{1}{M_A}\nabla_A^2 - \sum_{i=1}^{N}\sum_{A=1}^{M}\frac{Z_A}{r_{iA}} + \sum_{i=1}^{N}\sum_{j>i}^{N}\frac{1}{r_{ij}} + \sum_{A=1}^{M}\sum_{B>A}^{M}\frac{Z_A Z_B}{R_{AB}} \tag{1.2}$$

The first and second terms represents the kinetic energy of the N electrons and M nuclei respectively. The third term represents the electron-nuclei attraction, fourth and fifth terms represents the electron-electron and nuclei-nuclei repulsion respectively. Since the mass of the nuclei is heavier than the mass of the electrons, the nuclei are assumed to be fixed in space, where electrons can move in the field generated by the nuclei. Thus, the nuclear kinetic energy term is neglected and the nuclei-nuclei repulsion term is kept as constant. This is known as the Born-Oppenheimer approximation [47] and the resultant Hamiltonian can be written as:

$$\hat{H} = -\frac{1}{2}\sum_{i=1}^{N}\nabla_i^2 - \sum_{i=1}^{N}\sum_{A=1}^{M}\frac{Z_A}{r_{iA}} + \sum_{i=1}^{N}\sum_{j>i}^{N}\frac{1}{r_{ij}} \tag{1.3}$$

$$\hat{H}_{elec} = T + V_{Ne} + V_{ee} \tag{1.4}$$

$\hat{H}_{elec}$ is called as electronic Hamiltonian operator. V_{Ne} is the attractive potential and referred as an external potential (V_{ext}) in DFT. The Schrödinger equation can now be written as [47]:

$$\begin{aligned} \hat{H}_{elec}\Psi_{elec} &= E_{elec}\Psi_{elec} \\ E_{total} &= E_{elec} + E_{nucl} \end{aligned} \tag{1.5}$$

While methods like DFT [48], Configuration interaction [47, 49], Coupled Cluster theory [47, 49], MP2 [47, 49] methods can be employed to study many electron systems, this thesis focusses only on DFT due to the computational tractability to investigate large molecular systems like clathrate hydrates. In the next section, a brief description of DFT is presented.

1.4.1 Density Functional Theory (DFT)

Density Functional Theory was first developed by Walter Kohn and co-workers [48, 50–52]. Conceptually, DFT is similar to other *ab initio* methods, where the electron density, $\rho(r)$, plays a key role. According to Hohenberg-Kohn's theorem, the ground state energy (E_0) of a system can be defined as:

$$E_0 \leq E_v[\rho] = \int \rho(r) V_{ext}(r) dr - \frac{1}{2} \sum_{i=1}^{N} < \psi_i | \nabla_i^2 | \psi_i > + \frac{1}{2} \int \int \frac{\rho(r)\rho(r')}{|r - r'|} dr dr' + E_{xc}[\rho(r)] \tag{1.6}$$

The first term contains an external effective potential, ($V_{ext}(r)$). The second term is the kinetic energy of a non-interacting system. The third term is the classical expression of the interaction energy. The last term (E_{xc}) is called as an exchange correlation energy. Using the variational principle, where $\int \rho(r) dr = N$, E_0 is calculated by a minimization of $E_v[\rho]$. Alternatively, the variational principle applied to the Kohn-Sham orbitals (ψ_i) in Eqn 1.6, leads to the following eigen value equation:

$$[-\frac{1}{2}\nabla^2 + v(r) + \int \frac{\rho(r)}{|r - r'|} dr' + V_{xc}(r)]\psi_i = \epsilon_i \psi_i \tag{1.7}$$

Eqn 1.7 is called as Kohn-Sham equation [52]. ϵ_i is the i^{th} orbital energy. The exchange-correlation potential, $V_{xc}(r)$ is written as:

$$V_{xc} = \frac{\partial E_{xc}[\rho(r)]}{\partial \rho(r)} \tag{1.8}$$

E_{xc} contains the kinetic correlation energy (difference in the kinetic energy functional between the real and the non-interacting reference system), the exchange energy (due to the antisymmetric requirement of wavefunctions), coulombic energy (arises from inter-electronic repulsion) and a self-interaction correction. Hence, any source of error arises only due to the choice of E_{xc}. The exchange-correlation functionals is divided into two categories: The Local Density Approximation (LDA) and Generalized Gradient Approximation (GGA).

1.4.1.1 The Local Density Approximation (LDA)

The assumption of LDA is seen from a local density treated as an uniform electron gas, where the density, $\rho(r)$, varies slowly with r. The exchange-correlation energy [53–58] is written as:

$$E_{xc}^{LDA}[\rho] = \int \rho(r)\epsilon_{xc}^{LDA}(\rho(r))dr \tag{1.9}$$

where ϵ_{xc}^{LDA} is the exchange plus correlation energy per electron in a homogeneous electron gas with electron density. For systems where density varies slowly, LDA tends to perform well with accurate prediction of chemical properties. However, in strongly correlated systems, the assumption of a homogeneous electron gas leads to an inaccurate prediction of chemical properties using LDA.

1.4.1.2 The Generalized Gradient Approximation (GGA)

The exchange correlation functional depends on the density and its gradient and is written as:

$$E_{xc}^{GGA}[\rho(r)] = \int \rho(r)\ \epsilon_{xc}^{GGA}(\rho(r),\ |\Delta\rho(r)|)\ dr \tag{1.10}$$

Some examples of GGA functionals are: Perdew and Wang [59], Perdew, Burke and Ernzerhof (PBE) [60] and Becke's [61] formula for the exchange combined with Perdew's 1986 [62] formula for correlation. Other popular exchange correlation functionals used in computational chemistry are: B3LYP (Becke's 3 Lee Yang and Parr) [61, 63], M05 [64], M05-2X [64], M06-2X [65], B97-D (Becke's 97 Dispersion) [66] etc. For the sake of completeness, a brief description of some of the hybrid exchange correlation functionals used in this thesis is presented below.

B3LYP exchange correlation functional:

The exchange correlation energy of the B3LYP functional [61, 63] can be written as :

$$E_{xc}^{B3LYP} = (1-a)E_x^{LSDA} + aE_x^{exact} + b\Delta E_x^{B88} + (1-c)E_c^{LSDA} + cE_c^{LYP} \tag{1.11}$$

The description of the energy terms which contribute to the E_{xc}^{B3LYP} functional is described in Reference [61, 63].

Minnesota exchange correlation functionals:

The Minnesota suite of exchange correlation functionals [64,65] are designed to characterize non-covalent interactions in molecular systems. The Minnesota exchange correlation energy can be written as:

$$E_{xc}^{hyb} = \frac{X}{100} E_x^{HF} + \left(1 - \frac{X}{100}\right) E_x^{DFT} + E_c^{DFT} \tag{1.12}$$

where, E_x^{HF} is the non-local Hartree - Fock exchange energy, x is the percentage of Hartree - Fock exchange, E_x^{DFT} is the local DFT correlation energy and E_c^{DFT} is the dynamic correlation energy.

Dispersion corrected functionals:

Dispersion interactions play an important role in the stability of clathrate hydrates. The origin of these dispersion interactions arise when the encapsulated gas molecules interact with water cages via weak vdW interactions (dispersive forces). These interactions reduces the free energy of the water molecules and makes the clathrate hydrates stable when sufficient number of water cages are filled with gas molecules. Depending on the encapsulated gas molecules, dispersion interactions can also include contributions from dipole-dipole interactions dipole-induced dipole and London dispersive forces. Some examples of dispersion corrected functionals are: B97-D [66], vdW-D3 [67], vdw-DF1 [68], vdw-DF2 [69] etc. As an example, the total energy (E_0) calculated using the B97-D functional [66] can be written as:

$$E_0 = E_{KS-DFT} + E_{disp} \tag{1.13}$$

where, E_{KS-DFT} is the self-consistent Kohn-Sham energy as obtained from the chosen density functional and E_{disp} is an empirical dispersion correction.

$$E_{disp} = -S_6 \sum_{i=1}^{N_{at}-1} \sum_{j=i+1}^{N_{at}} \frac{C_6^{ij}}{R_6^{ij}} f_{dmp}(R_{ij}) \tag{1.14}$$

$$C_6^{ij} = \sqrt{C_6^i C_6^j} \tag{1.15}$$

where, N_{at} is the number of atoms in the system, C_6^{ij} denotes the dispersion coefficients for atoms i and j, S_6 is the global scaling factor, R_{ij} is an inter-atomic distance. The near-singularities for small R_{ij} is avoided by using a damping function f_{dmp} which is given by,

$$f_{dmp}(R_{ij}) = \frac{1}{1 + e^{-d(R_{ij}/R_r - 1)}} \tag{1.16}$$

where, R_r is the sum of the atomic vdW radii.

Exchange correlation functionals for clathrate hydrates:

Non-covalent interactions (weak interactions, hydrogen bonding, dispersive interactions, etc.) stabilize the framework of water cages of clathrate hydrates. For example, a schematic representation of hydrogen bonding interactions in the cages of clathrate hydrates is shown in Figure **1.3**. In clathrate hydrates, the presence of hydrogen bonding between the encapsulated gas molecules and the water cages have been reported by Kumar et. al. [43], Alavi et. al. [71] and Buch et. al. [72]. The exchange-correlation functionals in LDA and some GGA functionals (e.g. B3LYP) lack description of non-covalent interactions which exist in clathrate hydrates. Hence, dispersion corrected functionals are obvious choices for electronic structure characterization of molecular interactions in clathrate hydrates.

1.4.2 Reaction mechanism pathways: Application of numerical methods

The mechanism of encapsulation of gas molecules in cages of clathrate hydrates can also be examined using numerical methods. The commonly known numerical methods [49,70] are based on surface walking and interpolation. The surface walking method involves computation of local gradient and Hessian matrix [73–76]. Further, this method uses the reactant configuration to predict the formation of products and saddle points. This algorithm performs poorly for unimolecular reactions with several low frequency vibrational modes (e.g. clathrate hydrates). The interpolation based methods [79–87] uses input configurations of reactants and products to generate a series of intermediate configurations

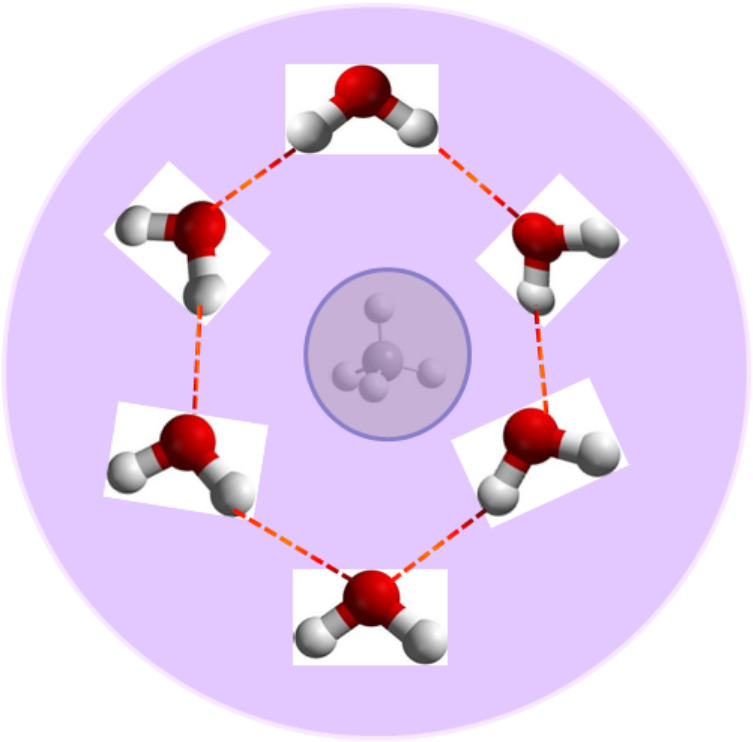

Figure 1.3: Schematic representation of hydrogen bonding interactions in cages of clathrate hydrates.

(also called as images). Among several interpolation methods, the Nudge Elastic-Band method (NEB) [85–87] is widely used to determine the MEP and is discussed in the next section.

1.4.2.1 Nudged Elastic Band method

The NEB method [85–87] is employed to characterize the MEP of a reaction when both the reactant (**R**) and product (**P**) configurations are known. A linear interpolation method [88] is employed to generate a set of images between **R** and **P**. These images are connected together by elastic springs to form a discrete path from the **R** to **P**. The images are independently relaxed by an optimization procedure to obtain the MEP. The total force acting on the i^{th} image is a sum of spring force (in the direction of the local tangent at the i^{th} image) and a force perpendicular to the local tangent at i^{th} image. The total force can

be written as:

$$F_i = F_i^S|_{\|} - \nabla E(R_i)|_{\perp} \tag{1.17}$$

where, F_i^S is the spring force which connects two neighbouring images and can be defined as:

$$F_i^S|_{\|} = k(|R_{i+1} - R_i| - |R_i - R_{i-1}|)\hat{\tau}_i \tag{1.18}$$

where, k is the spring constant. $\hat{\tau}_i$ is the normalized local tangent at image i. The true force ($\nabla E(R_i)$) acting on each image and can be defined as:

$$\nabla E(R_i)|_{\perp} = \nabla E(R_i) - \nabla E(R_i).\hat{\tau}_i \tag{1.19}$$

E is the total energy of the system. R_i contains the atomic positions corresponding to the i^{th} image.

While NEB is a popular method for determination of MEP, the quick convergence of this method does not lead to the exact saddle point. This is corrected by using a Climbing Image NEB (CI-NEB) [76] method. The CI-NEB method uses the MEP generated using the NEB method. Subsequently, the image with the highest energy (i_{max}) from the MEP is identified. This image is climbed up to the saddle point till no spring force is observed. At this point, the true force along the local tangent is inverted and maximized in perpendicular direction and minimized in all other directions to obtain an exact saddle point. The force acting on i_{max} is written as:

$$\begin{aligned} F_{i_{max}} &= -\nabla E(R_{i_{max}}) + 2\nabla E(R_{i_{max}})|_{\|} \\ &= -\nabla E(R_{i_{max}}) + 2\nabla E(R_{i_{max}}).\hat{\tau}_{i_{max}}.\hat{\tau}_{i_{max}} \end{aligned} \tag{1.20}$$

where $\hat{\tau}_{i_{max}}$ is the tangent along the path. A schematic representation of MEP obtained using NEB and CI-NEB is shown in Figure **1.4**. In the next section free energies and reactivity indices calculated from *ab intio* methods is presented.

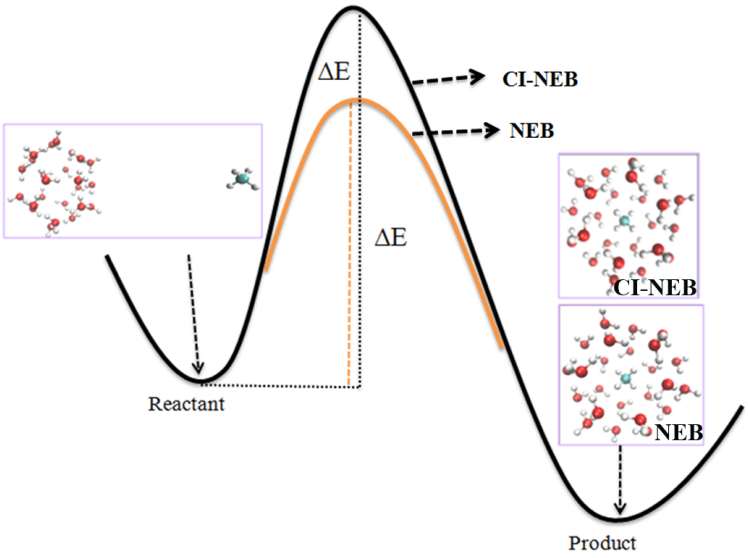

Figure 1.4: Schematic representation of Minimum Energy Pathway.

1.4.3 Free Energy

All thermodynamic quantities are calculated using a standard statistical mechanical approach [97]. The enthalpy of reaction is defined as follows:

$$\Delta H = \sum(\mathcal{E}_o + H_{corr})_{products} - \sum(\mathcal{E}_o + H_{corr})_{reactants} \tag{1.21}$$

where $\mathcal{E}_o$ is the total energy (obtained from geometry optimization). H_{corr} is the correction to the enthalpy due to the internal energy (obtained from frequency calculation). The entropy of the reaction is calculated, such that

$$\Delta S = \sum(S)_{products} - \sum(S)_{reactants} \tag{1.22}$$

The free energy of reaction is defined as:

$$\Delta G = \Delta H - T\Delta S \tag{1.23}$$

1.4.4 Reactivity indices

Parr and co-workers [48, 98, 99] defined an electronic chemical potential (μ) as:

$$\mu = \left(\frac{\partial \mathrm{E}}{\partial \mathrm{N}}\right)_{\nu} \tag{1.24}$$

where, E is the electronic energy, N is number of electrons, ν is an external potential due to the nuclei. The chemical potential, (μ), is an instantaneous slope determined using the method of finite differences. Alternatively, the chemical potential, μ, can be written as:

$$\mu = -\left[\frac{E(N-1) - E(N+1)}{2}\right] \quad or\, \mu \approx \left(\frac{I+A}{2}\right) \tag{1.25}$$

$$\left(\frac{I+A}{2}\right) = \chi_m = -\mu \tag{1.26}$$

where, χ_m is the Mulliken electronegativity. The stability of a chemical system can be described by a hardness parameter (η), defined as the measure of resistance to change in electronic distribution. Parr and Pearson [99] defined chemical hardness (η) as:

$$\eta = \frac{1}{2}\left[\frac{\partial^2 E}{\partial N^2}\right]_{\nu} \quad or\, \eta = (I - A) \tag{1.27}$$

I and A are calculated using the Koopman's theorem and is defined as:

$$I = -E_{HOMO} \;\; and \;\; A = -E_{LUMO} \tag{1.28}$$

For any chemical system, the electro-philicity index (ω) is defined as:

$$\omega = \frac{\chi^2}{2\eta} \tag{1.29}$$

where, ω describes the reactivity of the system. Hence, the reactivity of cages of clathrate hydrates is characterized by a calculation of parameters like electro-negativity (χ), hardness (η) and electro-philicity (ω). Similar to the work of Chattaraj et. al. [100], the

reactivity indices were calculated as:

$$\chi = \frac{I + A}{2} = -\frac{E_{LUMO} + E_{HOMO}}{2}, \quad \eta = I - A = E_{LUMO} - E_{HOMO}, \quad \omega = \frac{\chi^2}{2\eta} \tag{1.30}$$

1.4.5 Vibrational Raman Spectra

The Vibrational Raman spectra of clathrate hydrates is calculated using a harmonic approximation [49, 101]. The Raman intensity is calculated as:

$$\text{Raman intensity} \propto \left(\frac{\partial \alpha}{\partial q}\right)^2 \propto \left(\frac{\partial^3 E}{\partial R \partial F^2}\right)^2 \tag{1.31}$$

where, α is the polarizability, q is the normal coordinate, E is the potential energy, R is the nuclear geometry and F is an external electric field.

1.5 Methodology

1.5.1 Calculation details

The GAUSSIAN [89,90] and Vienna *ab initio* Simulation Package (VASP) [91] programs are used for calculations. In this thesis, the M05-2X [64], B97-D [66], D3 [67], vdW-DF1 [68] and vdW-DF2 [69] exchange correlation functionals is chosen due to large number of hydrogen bonding sites and dispersion interactions present in the cages of clathrate hydrates. The coordinates for the construction of hydrate lattice was taken from the McMullan et. al. [92]. The polyhedral water cages were extracted from the constructed hydrate lattice. For example, a full sI hydrate lattice was constructed. The input configurations of 5^{12} and $5^{12}6^2$ cages were extracted from the hydrate lattice (see Figure **1.5**). The optimization of input configurations was performed using an opt=tight (cutoff: Root Mean Square (RMS) force = 10^{-5} a.u., Maximum force = 1.5 x 10^{-5} a.u., RMS displacement = 4 x 10^{-5} a.u., Maximum displacement = 6 x 10^{-5} a.u.) convergence criteria using a Berny algorithm [93, 94]. The numerical computation of two-electron integrals

was performed using an ultrafine grid [89, 90]. The optimized geometry of 5^{12} and $5^{12}6^2$ cages in cartesian co-ordinates is shown in **Appendix A**.

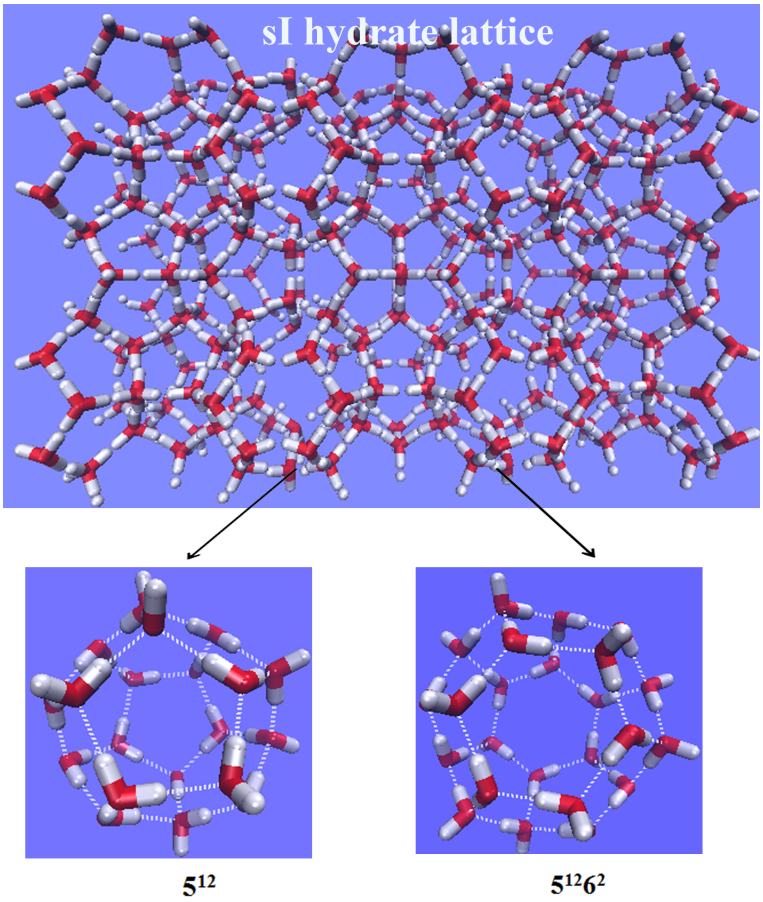

Figure 1.5: Schematic representation of sI hydrate lattice and its constituent polyhedral water cages.

1.6 Outline of this work

In this thesis, various properties of the cages of methane, hydrogen, nitrogen and oxygen clathrate hydrates is characterized using DFT. A brief description of the following chapters is as follows:

Chapter 2 describes the thermodynamic stability and reactivity of cages of methane clathrate hydrates. The effect of basis set and functionals is investigated to demonstrate its influence on interaction energies. A thermodynamic study performed at various tem-

peratures to determine the free energy of formation of the cages on the encapsulation of CH_4 molecule. The computed reactivity indices of the cages is also determined.

Chapter 3 describes a characterization of the changes in vibrational modes which occur with the encapsulation of CH_4 in these cages. The effect of functionals (M05-2X and B97-D functionals) on vibrational Raman spectra is examined. The changes which occur with the encapsulation of CH_4 in the different frequency regions is characterized. The changes in the high and mid frequency spectra on encapsulation of CH_4 is investigated. The low frequency vibrational modes which are collective motion of the water molecules and CH_4 in these cages is also investigated.

Chapter 4 describes the mechanism of diffusion of CH_4 in 5^{12} and $5^{12}6^2$ cages. In this study, three exchange correlation functionals (D3, DF1 and DF2) and Nudge Elastic Band method is employed to determine the MEP. The activation energy and kinetics of diffusion of CH_4 in 5^{12} and $5^{12}6^2$ cages is calculated and compared. The activation energy associated with the diffusion of CH_4 in fused cages is also examined.

Chapter 5 describes an investigation of thermodynamic stability and hydrogen storage capacity in cages of pure and THF doped hydrogen clathrate hydrates. The interaction energy and free energy of formation of multiple occupancies of H_2 in dodecahedron (5^{12}) and hexakaidecahedron ($5^{12}6^4$) water cages of pure and THF doped hydrogen clathrate hydrates is characterized.

Chapter 6 describes the vibrational changes which occur with the multiple encapsulation of H_2 in cages of pure and THF doped dodecahedron (5^{12}) and hexakaidecahedron ($5^{12}6^4$) water cages. In this study, vibrational Raman spectral analysis is performed to probe vibrational changes on encapsulation of H_2 in 5^{12} and $5^{12}6^4$ cages. The trends observed from the calculated Raman vibrational modes are compared with previous experimental findings. The deformation energy of the cages is also calculated.

Chapter 7 and **8** describes the stability and vibrational Raman spectra of cages of nitrogen and oxygen clathrate hydrates. These hydrates exist in abundance in the solar

system and in interstellar space. The interaction energy and vibrational Raman spectra of multiple occupancy of N_2 and O_2 in 5^{12} and $5^{12}6^4$ water cages is characterized. The interaction energies and spectral shifts are compared with the experimental observations.

Chapter 9 summarizes the salient results of the structure, stability, free energy and the mechanism of formation of cages of clathrate hydrates. A characterization of CH_4 replacement by CO_2 in the cages of clathrate hydrates using Ab Initio Molecular Dynamics (AIMD) simulations and an examination of H_2 clathrate hydrate formation is presented as one of the future activities.

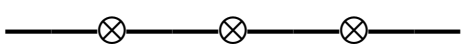

Chapter 2

Stability and Reactivity of methane clathrate hydrates

2.1 Introduction

Methane clathrate hydrates have attracted attention due to its abundance and potential to serve as an energy resource due to its relatively low emissions compared to fossil fuels [5, 7–9]. These hydrates also exist as obstructive byproduct in fuel transportation pipelines. Methane clathrate hydrates are crystalline solids, where methane gas molecules are trapped inside various polyhedral water cages [6, 17, 102]. A unit cell [103, 104] of sI methane clathrate hydrate consists of two 5^{12} and six $5^{12}6^2$ cages, where a CH_4 molecule is trapped in the center of the 5^{12} and $5^{12}6^2$ cages. The resultant cages are called as $5^{12}CH_4$ and $5^{12}6^2CH_4$ cages respectively. These cages are formed when methane gas derived from a biogenic or a thermo-genic origin interact with water molecules under suitable thermodynamic conditions [105]. Experimental characterization of the individual cages is extremely challenging due to the small size of the hydrate nuclei [9]. However, computational methods like MD simulations and *Ab initio* methods have been employed to understand the mechanism of nucleation and growth of these hydrates.

A large number of studies [12, 31–34, 106–122] from MD simulations has been employed to understand the mechanism of nucleation and growth of methane clathrate hy-

drates. Rodger et. al. [31–33, 119] performed a series of MD simulations to study the nucleation of methane clathrate hydrates from a CH_4/H_2O system. The authors described the hydrate nucleation mechanism using a labile cluster hypothesis and a local structuring hypothesis. The authors performed MD simulations at different temperatures to observe the formation of the cages. However, the authors could not observe the complete crystallization process since the simulation time scales was confined to a few nanoseconds. Hawtin et. al. [34] employed MD simulations on a CH_4/H_2O interface system and observed a spontaneous nucleation. The authors concluded that nucleation proceeds via a formation of a tetrahedral network of H_2O and CH_4 molecules that resembles a 5^{12} cage. Guo et. al. [35] also performed constrained MD simulations in a simple CH_4/H_2O system and studied the probability of formation and lifetime of 5^{12} cages. The authors showed that the H_2O cages around CH_4 molecules have a relatively long life time ($\sim$ 100 picoseconds). Further, the authors found that the 5^{12} cage adsorbs CH_4 strongly and the adsorption interaction is independent of the concentration of CH_4 molecules. Walsh et. al. [36] performed microsecond simulations and observed that the hydrate nuclei lack long-range crystalline order. Vatamanu et. al. [123] studied the homogeneous nucleation of methane clathrate hydrates from a bulk solution. The authors showed that the areas locally rich in CH_4 will nucleate spontaneously.

While, there has been sufficient understanding on the nucleation and growth of sI structures using MD simulations, there has been very limited work to characterize the stability and reactivity of $5^{12}CH_4$ and $5^{12}6^2CH_4$ cages which are the building blocks of the sI methane clathrate hydrates. The *ab initio* calculations of Arshad Khan [124] showed that compared to the $(H_2O)_{21}$ cage, the 5^{12} cage is most likely to form a natural hydrate structure. The molecular potential energies of $5^{12}CH_4$ cages have been studied by Q. S. Du et. al. [125] using DFT and B3LYP/TZVP functional. The authors concluded that a functional better than B3LYP is required to describe dispersion interactions accurately for large molecular clusters like these cages. The substitution of CH_4 by CO_2 in 5^{12} and $5^{12}6^2$ cages have been studied by Geng et. al. [126] using DFT and B3LYP functional. The authors reported that the CH_4 molecule inside the 5^{12} cage is stable, whereas CO_2 is found

to be stable inside the $5^{12}6^2$ cage. Roman-Perez et. al. [127] and Li et. al. [128] studied the interaction energy of CH_4 in various cages of the hydrate lattice using the vdW-DF functional. The authors observed that the stabilization of CH_4 in the $5^{12}6^2$ cage is more compared to the 5^{12} cage. Kumar et. al. [43] investigated a single occupancy of various gases in 5^{12} cages using the MP2 method to show the dependence of interaction energies on basis sets. The authors observed that the interaction energies of CH_4 in the 5^{12} cage calculated from different basis sets show a variation of 6.14 - 10.82 kcal/mol. However, the authors performed a single point energy calculation on the cages using larger basis sets to calculate the interaction energy with their investigation limited to the 5^{12} cage. Sastry and co-workers [44] demonstrated that the MP2 method and DFT functionals like M05-2X [64, 65] and B97-D [66] provide similar interaction energies.

Based on previous studies [43,44], the M05-2X [64, 65] functional has been employed to demonstrate the dependence of interaction energies on basis sets in the present study. The suite of Pople basis, correlation consistent and augmented correlation consistent basis sets are used to demonstrate basis set dependence on energies. Among the Pople basis sets, the 6-311++G(d,p) is the largest basis set with 720 basis functions for the 5^{12} cage, 770 basis functions for the $5^{12}CH_4$ cage, 864 basis functions for the $5^{12}6^2$ cage, and 914 basis functions for the $5^{12}6^2CH_4$ cage. Among the correlation consistent basis sets, the cc-pVQZ is the largest basis set with 2300 basis functions for the 5^{12} cage, 2475 basis functions for the $5^{12}CH_4$ cage, 2760 basis functions for the $5^{12}6^2$ cage, and 2935 basis functions for the $5^{12}6^2CH_4$ cage. Further, at large basis sets, interaction energies have been calculated using the B97-D [66] functional and compared with other DFT functionals and other methods. The free energies associated with the encapsulation of CH_4 in 5^{12} and $5^{12}6^2$ cages and the corresponding computed reactivity indices are calculated using the M05-2X [64, 65] functional. The design of inputs and details of DFT calculations are described in Section 2.2. The interaction energies, free energies and reactivity indices from the DFT calculations are presented in the Section 2.3. A summary of salient results concludes this chapter.

2.2 Computational details

The identification of the optimized configurations was done as follows: There are 30,026 [129–131] configurations for the 5^{12} cages and 30,43,836 configurations for the $5^{12}6^2$ cages which follow the ice-rules (also known as Bernal-Fowler rules) [19]. Among the 30,026 symmetry distinct configurations of 5^{12} cages, the optimized configurations of the 5^{12} ($5^{12}CH_4$ cages) were found to belong to the family of 12 lowest lying energy isomers with 10 dangling hydrogen atoms, 21 strong hydrogen bonds and 9 weak hydrogen bonds and is consistent with the work of Kirkov et. al. [130] Similarly, among the 30,43,836 configurations of $5^{12}6^2$ ($5^{12}6^4CH_4$) cages, the optimized configurations are found to belong to the family I structures which are the lowest lying energy minima as seen in work of Yoo et. al. [131] The difference in configurations arise due to various possible orientations of hydrogen atoms of the water cages. Yoo et. al. [131] employed a "bottom-up" approach to study the formation of the periodic hydrate lattice starting from the energy minimized water cages. The authors showed that the resultant hydrate lattice has a reduced number of possible configurations and it consists of 46 water molecules.

The optimized configurations corresponding to the 5^{12}, $5^{12}6^2$, $5^{12}CH_4$ and $5^{12}6^2CH_4$ cages are shown in Figure **2.1**. Frequency calculations on the optimized geometries of the cages did not generate any imaginary frequencies. The Basis Set Superposition Error (BSSE) was calculated using the counterpoise method [132, 133] at the optimized geometry. The interaction energies (IE) corresponding to the respective cages are calculated as follows:

$$\begin{aligned} IE1 &= E[5^{12}] - 20E[H_2O] \\ IE2 &= E[5^{12}CH_4] - E[5^{12}] - E[CH_4] \\ IE3 &= E[5^{12}6^2] - 24E[H_2O] \\ IE4 &= E[5^{12}6^2CH_4] - E[5^{12}6^2] - E[CH_4] \end{aligned} \tag{2.1}$$

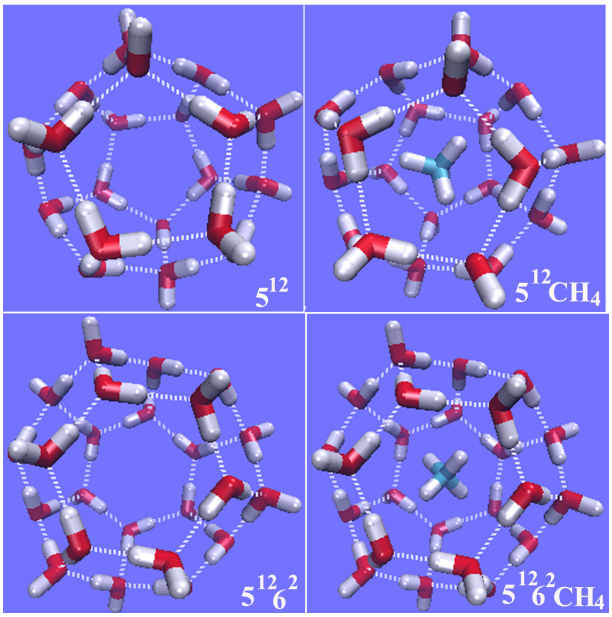

Figure 2.1: Optimized structures of 5^{12}, $5^{12}6^2$, $5^{12}CH_4$ and $5^{12}6^2CH_4$ cages.

where, the total energy (E) includes corrections from BSSE. E[5^{12}] and E[$5^{12}6^2$] is the total energy of 5^{12} and $5^{12}6^2$ cages respectively. E[H_2O] is the total energy of single water molecule. E[$5^{12}CH_4$] and E[$5^{12}6^2CH_4$] is the total energy of the $5^{12}CH_4$ and $5^{12}6^2CH_4$ cages respectively. The hydrogen bond strength of the cages (5^{12} and $5^{12}6^2$) has been calculated and is written as follows:

$$\begin{aligned} \text{IE1H} &= \text{IE1}/\text{nH1} \\ \text{IE3H} &= \text{IE2}/\text{nH2} \end{aligned} \tag{2.2}$$

where, nH1 = 30 and nH2 = 36 represents the number of hydrogen bonds in 5^{12} and $5^{12}6^2$ cages respectively.

To investigate the spontaneity of formation of the $5^{12}CH_4$ and $5^{12}6^2CH_4$ cages from the 5^{12} and $5^{12}6^2$ cages respectively, free energy calculations have been performed at T = 1 K, 50 K, 100 K, 200 K, 250 K, 273 K and 298 K, at P = 1 bar. In order to compare with experimental conditions, [23, 134] free energy calculations has been performed at high pressures (P = 77 bar and 100 bar), at 273 K and 298 K.

2.3 Results and Discussion

2.3.1 Cage radius

The radius of cavity calculated (using the cc-pVQZ basis set) for the optimized 5^{12}, $5^{12}6^2$, $5^{12}CH_4$ and $5^{12}6^2CH_4$ cages is shown in Table 2.1. An inclusion of a CH_4 molecule in the 5^{12} cage shows an expanded $5^{12}CH_4$ cage. However, the radius for a $5^{12}6^2$ cage is 4.63 Å, whereas the radius of the $5^{12}6^2CH_4$ cage is 4.33 Å. The inclusion of a CH_4 molecule inside the $5^{12}6^2$ cage favors a contraction of the cage leading to the formation of $5^{12}6^2CH_4$ cage. The calculated radius of the $5^{12}CH_4$ and $5^{12}6^2CH_4$ cages are in excellent agreement with experimental data [7].

Table 2.1: Radius (Å) of the 5^{12}, $5^{12}6^2$, $5^{12}CH_4$ and $5^{12}6^2CH_4$ cages.

Cage	This work	Expt [7]
5^{12}	3.72	-
$5^{12}CH_4$	3.95	3.98
$5^{12}6^2$	4.63	-
$5^{12}6^2CH_4$	4.33	4.37

2.3.2 Dependence of interaction energy on Basis sets

The total energies (includes corrections from BSSE) at the optimized geometries for the 5^{12}, $5^{12}6^2$, $5^{12}CH_4$ and $5^{12}6^2CH_4$ cages using different basis sets are shown in Appendix (see Table B2-1). As expected, the total energies show a decrease with increasing basis set size for the suite of Pople and correlation consistent basis sets.

The interaction energies calculated from the total energies using the M05-2X functional is shown in Table 2.2. The effect of basis set on interaction energies is seen from an examination of the IE1 and IE3 energies. The difference in IE1/IE3 energies calculated between the 6-31G(d,p) and 6-31G basis sets is 128.18/167.6 kcal/mol. The difference in IE1/IE3 energies calculated between the 6-31++G(d,p) and 6-31G(d,p) basis sets is

19.02/24.25 kcal/mol. Compared to diffuse functions, polarization functions have a larger impact on interaction energies. However, both diffuse and polarization functions have a significant impact when Dunning type basis functions are used. For example, the difference in IE1/IE3 energy from cc-pVTZ and cc-pVDZ basis sets is 64.96/49.31 kcal/mol, and the aug-cc-pVDZ and cc-pVDZ basis sets is 86.04/60.05 kcal/mol. Similar trends are also seen from the IE2 and IE4 energies. An examination of the difference between IE2 and IE4 for all basis sets, show that the formation of the $5^{12}CH_4$ cage is more favored compared to the $5^{12}6^2CH_4$ cage. For example, the IE2-IE4 energy from the cc-pVQZ basis set is -1.30 kcal/mol. A clear understanding on the stability of the cages is provided by the calculation of hydrogen bonding energy. For example, the IE1H energy represents the average hydrogen bond energy in the 5^{12} cage. The hydrogen bond energy calculated using the cc-pVQZ basis set is -4.17 kcal/mol. This shows that hydrogen bond interactions play a dominant role in the formation of 5^{12} cages. Similar to the IE1H energy, the IE3H energy calculated using the cc-pVQZ basis set is -4.55 kcal/mol which shows that the hydrogen bond interaction contribute significantly to the formation of the $5^{12}6^2$ cages.

A comparison of interaction energies from the M05-2X and B97-D functional with previous theoretical data is shown in Table **2.3**. It is known [135] that depending on the orientation of the hydrogen atoms of the water molecules of the cages, the IE1 energy can show a variation of upto 70 kcal/mol. Further, the choice of method (DFT or MP2), different functionals employed in DFT and quality of basis set used in the calculations can strongly influence the determination of interaction energies. For example, Goddard and co-workers [136] reported IE1 energies of -191.73 kcal/mol (B3LYP), -204.43 kcal/mol (X3LYP) and -199.54 kcal/mol (M06) from the 6-311++G(d,p) basis set. Sotiris and co-workers [137] reported IE1 energy of -200.10 kcal/mol using the MP2 method and Complete Basis Set. Sotiris and co-workers [137] also reported an IE1 energy of -212.10 kcal/mol using the MP2 method with the aug-cc-pVDZ basis set and found a global minimum energy configuration.

The IE1 energies from M05-2X and B97-D functional (in this chapter) are -212.60 kcal/mol and -188.74 kcal/mol respectively. While, differences in IE1 energies from M05-

Table 2.2: Interaction energies (kcal/mol) calculated from total energies using the M05-2X functional.

Basis set	IE1	IE2	IE3	IE4
6-31G	-387.66	-6.59	-495.26	-6.09
6-31G(d,p)	-259.48	-7.24	-327.66	-6.70
6-31++G(d,p)	-240.46	-7.56	-303.41	-6.90
6-311G	-231.43	-8.31	-277.71	-7.26
6-311++G(d,p)	-212.60	-9.16	-269.21	-7.49
cc-pVDZ	-292.45	-7.09	-312.69	-6.77
cc-pVTZ	-227.49	-7.99	-263.38	-7.14
cc-pVQZ	-196.45	-9.45	-217.04	-8.15
aug-cc-pVDZ	-206.41	-8.61	-252.64	-7.73

2X and B97-D functional may appear large, they still remain in the range of IE1 energies reported from other DFT functionals and MP2. The IE2 energies calculated using the M05-2X and B97-D functional are -9.16 and -9.89 kcal/mol respectively. As seen in Table **2.3**, the B3LYP calculations of Loboda et. al. [138] produce very large IE2 energies and this could be the inability of B3LYP functional to include interactions present between the encapsulated CH_4 molecule and water. Such differences are due to the calculation of interaction energies using single point energy calculation of the cages.

The trends in IE3 energies are similar to IE1 energies, where lower energies are obtained from the B97-D functional compared to M05-2X. The trends in IE4 energies are similar to IE2 energies. For example, the IE4 energies obtained from the M05-2X and B97-D functionals is -7.49 and -7.87 kcal/mol respectively (see Table **2.3**). The IE3 and IE4 energies are reported for the first time in this study and can be validated from correlated *ab initio* methods like MP2 or experiment.

Table 2.3: Interaction energies from DFT and MP2 methods.

Method	Functional/Basis set	IE1	IE2	IE3	IE4
DFT	[a]M05-2X/6-311++G(d,p)	-212.60	-9.16	-269.21	-7.49
	[a]B97-D/6-311++G(d,p)	-188.74	-9.89	-247.68	-7.87
	B3LYP /6-311++G(d,p)	-191.73[b]	-11.05[c]	-	-
	[b]X3LYP /6-311++G(d,p)	-204.43	-	-	-
	[b]M06 /6-311++G(d,p)	-199.54	-	-	-
MP2	/aug-cc-pVDZ	-212.10[d]	-	-	-
	/Complete Basis Set	-200.10[e]	-6.14[f]	-	-

[a]this work, [b]Ref [136], [c]Ref [138], [d]Ref [130], [e]Ref [137], [f]Ref [43]

2.3.3 Effect of pressure and temperature on thermodynamic stability

An understanding of the stability of these cages is complemented from an examination of free energies of formation of various cages. The enthalpy, entropy and free energy change associated with the formation of $5^{12}CH_4$ cage (relative to the interaction of a CH_4 molecule inside the 5^{12} cage) and the formation of $5^{12}6^2CH_4$ cage (relative to the interaction of a CH_4 molecule in the $5^{12}6^2$ cage) are shown in Table **2.4**. As seen, for all temperatures and pressure the enthalpy change shows that the process of formation of the $5^{12}CH_4$ and $5^{12}6^2CH_4$ cages is an exothermic reaction.

An examination of free energies shows that formation of the $5^{12}CH_4$ and $5^{12}6^2CH_4$ cages is spontaneous at temperature below 200 K (P = 1 bar). The effect of pressure on the free energies shows that the formation of $5^{12}CH_4$ and $5^{12}6^2CH_4$ cage is spontaneous at 273 K at 77 and 100 bar. The high pressure calculations shows that the formation of these cages can be spontaneous even at ambient temperatures. For example, the spontaneity of formation for the $5^{12}CH_4$ cages occurs at 298 K with a pressure of 100 bar. Similar to the interaction energy, free energies show that the formation of the $5^{12}CH_4$ cage is relatively more favored compared to the $5^{12}6^2CH_4$ cage.

Table 2.4: ΔH (kcal/mol), TΔS (kcal/mol), ΔG (kcal/mol) using the M05-2X functional and cc-pVQZ basis set.

T (K)	P (bar)	ΔH_A	$T\Delta S_A$	ΔG_A	ΔH_B	$T\Delta S_B$	ΔG_B
298	1	-5.66	-8.28	2.62	-4.59	-7.15	2.56
298	77	-5.64	-5.87	0.23	-4.89	-5.78	0.89
298	100	-5.64	-5.54	-0.10	-4.89	-5.63	0.74
273	1	-5.71	-7.64	1.93	-4.67	-6.63	1.96
273	77	-5.73	- 5.30	-0.43	-4.68	-4.26	-0.42
273	100	-5.73	-4.94	-0.79	-4.68	-4.12	-0.56
250	1	-5.78	-7.05	1.27	-4.73	-6.12	1.39
200	1	-5.91	-5.78	-0.13	-4.87	-5.02	0.15
150	1	-6.02	-4.42	-1.60	-4.99	-3.88	-1.11
100	1	-6.08	-2.99	-3.09	-5.10	-2.66	-2.44
50	1	-5.98	-1.42	-4.56	-5.10	-1.32	-3.78
1	1	-5.65	-0.01	-5.64	-4.83	-0.01	-4.82

$\Delta H_A = H(5^{12}CH_4) - H(5^{12}) - H(CH_4)$
$\Delta S_A = S(5^{12}CH_4) - S(5^{12}) - S(CH_4)$
$\Delta G_A = \Delta H_A - T\Delta S_A$
$\Delta H_B = H(5^{12}6^2CH_4) - H(5^{12}6^2) - H(CH_4)$
$\Delta S_B = S(5^{12}6^2CH_4) - S(5^{12}6^2) - S(CH_4)$
$\Delta G_B = \Delta H_B - T\Delta S_B$

2.3.4 Reactivity Indices

The computed reactivity indices (calculated using Eqn.**1.30**) is shown in Table **2.5**. The reactivity parameters are compared between the 5^{12} and $5^{12}CH_4$ cages, $5^{12}6^2$ and $5^{12}6^2CH_4$ cages. The difference in χ between the $5^{12}CH_4$ and the 5^{12} cages is 0.045 eV (1.04 kcal/mol), which shows that the inclusion of a CH_4 molecule in the 5^{12} cage makes the $5^{12}CH_4$ cage slightly more electro-negative compared to 5^{12} cage. Similarly, the difference in η between the $5^{12}CH_4$ and the 5^{12} cages is 0.002 eV (0.05 kcal/mol) which shows that the inclusion of CH_4 molecule inside the 5^{12} cage causes an insignificant change in the

hardness of the $5^{12}CH_4$ cage. The difference in ω between the $5^{12}CH_4$ and the 5^{12} cages is 0.018 eV (0.42 kcal/mol) which shows that inclusion of a CH_4 molecule in the 5^{12} cage to form the $5^{12}CH_4$ cage makes it slightly more electro-philic. Thus the computed reactivity indices of the 5^{12} and $5^{12}CH_4$ cages are very similar. The difference in χ between

Table 2.5: Electro-negativity (χ), Hardness (η), and Electro-philicity (ω) using the M05-2X functional and cc-pVQZ basis set.

Cage	χ**(eV)**	η**(eV)**	ω**(eV)**
5^{12}	4.203	10.203	0.866
$5^{12}CH_4$	4.248	10.205	0.884
$5^{12}6^2$	4.534	11.515	0.893
$5^{12}6^2CH_4$	4.628	11.309	0.947

the $5^{12}6^2CH_4$ and the $5^{12}6^2$ cages is 0.094 eV (2.17 kcal/mol) which shows that inclusion of a CH_4 molecule in the $5^{12}6^2$ cage to form the $5^{12}6^2CH_4$ cage makes it significantly more electro-negative compared to $5^{12}6^2$ cage. The difference in η between the $5^{12}6^2CH_4$ and the $5^{12}6^2$ cages is -0.206 eV (-4.75 kcal/mol) which shows that the inclusion of CH_4 molecule inside the $5^{12}6^2$ cage dramatically reduces the hardness of the $5^{12}6^2CH_4$ cage. The difference in ω between the $5^{12}6^2CH_4$ and $5^{12}6^2$ cages is 0.054 eV (1.25 kcal/mol) which shows that inclusion of a CH_4 molecule in the $5^{12}6^2$ cage to form the $5^{12}6^2CH_4$ cage makes it significantly more electro-philic which suggests that the $5^{12}6^2CH_4$ cage is reactive, relatively with respect to $5^{12}6^2$ cage.

2.4 Conclusions

The results presented in this chapter suggest that high quality basis sets like cc-pVQZ along with an exchange correlation functional like the B97-D, M05-2X are required for the accurate determination of interaction energies, free energies and reactivity of the cages which are formed during the process of nucleation of methane clathrate hydrates. The

interaction energies are found to be strongly dependent on basis sets. The interaction energies show that the formation of the $5^{12}6^2$ cage is more favorable compared to the 5^{12} cage. However, on formation of the 5^{12} and $5^{12}6^2$ cages, the formation of the $5^{12}CH_4$ cage is more favored compared to the $5^{12}6^2CH_4$ cage. The IE1 energies calculated using the M05-2X and B97-D functionals (from large basis sets) are in the range of interaction energies calculated using the MP2 method. The free energies of formation of the cages provide an understanding of the thermodynamic conditions required for the spontaneous process of nucleation. The spontaneous formation of the $5^{12}CH_4$ cage occurs at 273 K and $P \geq 77$ bar, $5^{12}6^2CH_4$ cage at 298 K and 100 bar, and for both cages at T <200 K and P = 1 bar. The spontaneity of formation of the $5^{12}CH_4$ cage is more compared to the $5^{12}6^2CH_4$ cage. The computed reactivity indices show that the $5^{12}CH_4$ cage is as reactive as the 5^{12} cage, though the $5^{12}6^2CH_4$ cage is found to be more reactive than the $5^{12}6^2$ cage. In the next chapter, the spectral properties of methane clathrate hydrates is discussed.

Chapter 3

Raman spectra of vibrational and librational modes in methane clathrate hydrates

3.1 Introduction

The vibrational degrees of freedom of the CH_4 molecule encapsulated in the nano cavity of water cages are known to be perturbed compared to free CH_4 molecules [139, 140]. Depending upon the perturbation in the nano-cavity, the vibrational modes of the encapsulated CH_4 molecule can show changes in position and intensity compared to its free state [141]. Vibrational spectroscopy techniques such as Raman spectroscopy are useful [142–144] to characterize the effect of confinement of the CH_4 molecules trapped in these cages. Unlike Infrared spectroscopy, the advantage of using Raman spectroscopy lies in the ability to record spectra from very low frequency ($\sim 10\ cm^{-1}$) to high frequency ($\sim 4000\ cm^{-1}$) without varying any experimental parameters. Raman scattering have also been employed to investigate temperature and pressure dependant phase transitions in extended molecular structures [142, 144–147], to extract vital information about phases, nucleation and growth mechanism of host-guest complex structures [145].

For example, Sloan and co-workers [9] recorded the Raman spectra of gas molecules

like CH_4, CO_2 and their mixtures in different cages of the hydrate lattice. The authors observed a change in peak position and band shape upon variation of guest molecules encapsulated inside the cages of the hydrate lattice and suggested that Raman spectra can also be employed to monitor the formation of these hydrates. Sloan and co-workers [23] also showed that the occupancy of the guest molecules in different water cages obtained from the sea floor was in good agreement with measurements from laboratory synthesized natural clathrate hydrates. Ohno et. al. [148] experimentally characterized the Raman symmetric stretching vibration of CH_4 in clathrate hydrates. The authors observed that the symmetric stretching modes of CH_4 in the $5^{12}6^2CH_4$ cages were located at a lower frequency compared to $5^{12}CH_4$ cages. Complementary to experimental work, computational methods like MD simulations have been employed to characterize the vibrational modes in these hydrates. For example, Itoh et. al. [149] performed MD simulations using a Kumagai Kawamura and Yokokawa forcefield on the hydrate lattice and observed that the Raman stretching modes of CH_4 present in the $5^{12}6^2CH_4$ cages were observed at a lower frequency compared to the $5^{12}CH_4$ cage. Subsequently, Greathouse et. al. [150] performed MD simulations using a consistent valence force field and found results qualitatively similar to the work of Itoh et. al. [149]

However, experiments and MD simulations have used only the hydrate lattice as a model for study. Further, these studies have characterized only the C-H vibrations in the cages of the hydrate lattice and there have been limited information on the effect of CH_4 confinement in these cages on the vibrational modes of water molecules. The characterization of vibrational modes on the explicit cages (in contrast to the hydrate lattice) has never been investigated. The study of explicit cages has been received attention because these cages are formed during the initial stages of nucleation and further interconnect to form the hydrate lattice. The accurate determination of spectral properties in the explicit cages can be achieved by using quantum mechanical methods. In the present chapter, M05-2X and a dispersion corrected B97-D [66] functionals along with cc-pVQZ basis set [151] has been employed to investigate the effect of confinement of CH_4 in $5^{12}CH_4$ and $5^{12}6^2CH_4$ cages, with 5^{12} and $5^{12}6^2$ cages and free CH_4. The effect of vibrations of

the water molecules on the confinement of CH_4 is also probed. The results on the effect of CH_4 confinement via a characterization of vibrational Raman spectra is presented in Section 3.2. A summary of salient results concludes this chapter.

3.2 Results and Discussion

The calculated frequencies has been classified based on various modes of vibrations which occur in different regions: A low frequency region (<1000 cm^{-1}), mid-frequency region (1000 - 2100 cm^{-1}), and a high frequency region (2900 - 4100 cm^{-1}). The phrase "red-shift" and "blue-shift" represents a shift of various vibrational modes to lower and higher wave-numbers (or frequencies) respectively.

3.2.1 Effect of functionals on spectral properties

A comparison of Raman frequencies calculated using M05-2X [64, 65] and B97D [66] functionals is shown in Table **B3-1**. The ν_5 mode calculated using M05-2X functional appears at 3077 cm^{-1} for the free CH_4, 3067 cm^{-1} for CH_4 in the $5^{12}CH_4$ cage and 3061 cm^{-1} for CH_4 in the $5^{12}6^2CH_4$ cage. The magnitude of red-shift in the ν_5 mode is slightly higher compared to the B97-D functional. This is due to the exclusion of dispersion interactions which exists between the water molecules in the cages and CH_4 in the $5^{12}CH_4$ and $5^{12}6^2CH_4$ cages leading to larger red-shift. Similar trends are observed for all the modes using the M05-2X functional. The peak frequencies obtained from the B97-D functional shows excellent agreement with experimental data. Hence, the B97-D functional has been chosen for further analysis of various vibrational modes which occur in the cages of the hydrate lattice.

3.2.2 High frequency region

The high frequency Raman spectrum is shown in Figure **3.1** and **3.2**. A characteristic mode of vibration is the symmetric stretch (ν_5) of CH_4 (Table **3.1**, row 5). The symmetric stretch (ν_5) mode appears at 2928 cm^{-1} for the free CH_4 molecule, 2939 cm^{-1} for CH_4 in

the $5^{12}CH_4$ cage and 2918 cm^{-1} for CH_4 in the $5^{12}6^2CH_4$ cage. There are two implications from this observation: i) upon enclosure of CH_4 in the water cages, the ν_5 mode in the $5^{12}CH_4$ cage shows a blue-shift compared to the ν_5 mode of free CH_4. The trend of blue shift in the ν_5 mode is due to the dispersive interactions which exist between CH_4 and water molecules of the cages. ii) The ν_5 mode in $5^{12}6^2CH_4$ cage shows a red shift compared to $5^{12}CH_4$. This is due to reduced dispersion interaction between the CH_4 molecule and water molecules in the $5^{12}6^2CH_4$ cage. Similar trends are observed for the asymmetric stretch (ν_6) of CH_4, where the $5^{12}CH_4$ cage show a 16 cm^{-1} blue-shift compared to free CH_4. However, the ν_6 mode of CH_4 in the $5^{12}6^2CH_4$ cage show a 5 cm^{-1} red-shift compared to $5^{12}CH_4$ cage. As seen in Table **3.1**, the trends seen in the calculated ν_5 and ν_6 modes from the present results are qualitatively similar with the experimental work of Sloan and co-workers [23], Ohno et. al. [148] and MD simulations [149, 150] on the hydrate lattice.

The bending mode of H_2O (1587 cm^{-1}) is in excellent agreement with modes obtained using the vdW- DF functional [152] (1586 cm^{-1}) and experiment [153] (1592 cm^{-1}). The symmetric and asymmetric stretch in free H_2O is in agreement with the vdW- DF, though the deviation of calculated frequencies from experiment can be reduced by inclusion of corrections from an-harmonicity. Nevertheless, the calculated frequencies of free H_2O serve as an excellent benchmark for comparison with water molecules of the cages. The symmetric (ν_7) and asymmetric stretch (ν_8) modes of free H_2O molecule appear at 3739 cm^{-1} and 3855 cm^{-1}, respectively. The ν_7 and ν_8 modes of water molecules in the 5^{12}, $5^{12}CH_4$, $5^{12}6^2$ and the $5^{12}6^2CH_4$ cages show a significant red-shift compared to free H_2O molecule, due to the presence of hydrogen bonding in the cages. The ν_7 and ν_8 modes of water molecules in the $5^{12}CH_4$ and $5^{12}6^2CH_4$ cages shows a red-shift compared to 5^{12} and $5^{12}6^2$ cages respectively. This shows that the vibrational modes of the encapsulated CH_4 molecule are coupled to the vibrational modes of water molecules in the cages. Similar to trends seen in the vibrational modes of CH_4, the ν_7 and ν_8 modes of water molecules in the $5^{12}6^2CH_4$ cage shows a red-shift compared to the $5^{12}CH_4$ cage.

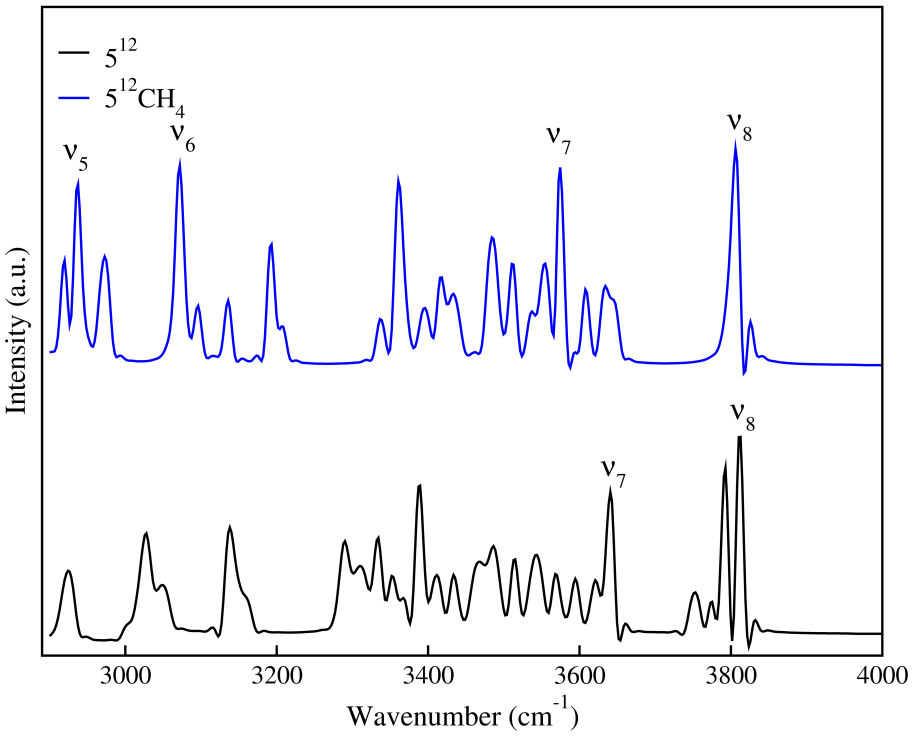

Figure 3.1: The symmetric and asymmetric stretch vibrations of 5^{12} and $5^{12}CH_4$ cages.

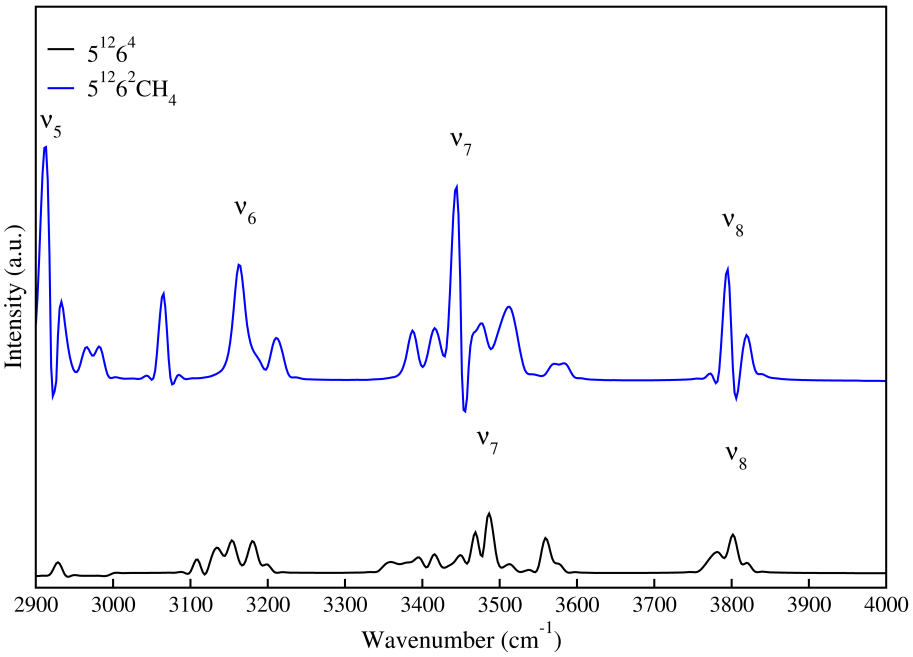

Figure 3.2: The symmetric and asymmetric stretch vibrations of $5^{12}6^2$ and $5^{12}6^2CH_4$ cages.

Table 3.1: Raman peak assignments (cm^{-1}) in 5^{12}, $5^{12}CH_4$, $5^{12}6^2$ and $5^{12}6^2CH_4$ cages (reference: free H_2O and free CH_4).

Modes	**H_2O**	**CH_4**	**5^{12}**	**$5^{12}CH_4$**	**$5^{12}6^2$**	**$5^{12}6^2CH_4$**
Libration (ν_1)	-	-	27-859	14-876	37-897	20-941
Bend (ν_2)	-	1306	-	1315	-	1308
						1255[a]
						1255[b]
						1304[c]
Rock (ν_3)	-	1518	-	1526	-	1517
						1395[a]
						1395[b]
						1520[c]
Bend (ν_4)	1587	-	1629	1627	1626	1625
Symmetric stretch (ν_5)	-	2928	-	2939	-	2918
				2915[a]		2905[a]
				3000[b]		2990[b]
				2842[c]		2826[c]
Asymmetric stretch (ν_6)	-	3055	-	3071	-	3066
				3085[b]		2986[b]
				3000[c]		3075[c]
Symmetric stretch (ν_7)	3739	-	3643	3572	3484	3449
Asymmetric stretch (ν_8)	3855	-	3811	3808	3802	3797

[a]Ref [23], [b]Ref [148], [c]Ref [149]

3.2.3 Mid frequency region

The mid-frequency Raman spectrum is shown in Figure **3.3** and **3.4**. The modes of vibration observed in this region are the bending (ν_2) and rocking (ν_3) modes of CH_4 and the bending (ν_4) mode of H_2O. The ν_2 mode of free CH_4 is observed at 1306 cm^{-1} which shows a blue-shift of 9 cm^{-1} in the $5^{12}CH_4$ cage and 2 cm^{-1} in the $5^{12}6^2CH_4$ cage (Table

3.1, row 2). The shift of the ν_2 mode of encapsulated CH_4 in the $5^{12}CH_4$ cage is larger than the $5^{12}6^2CH_4$ cage. This is due to more dispersion interaction between the CH_4 molecule and water molecules of the $5^{12}CH_4$ cage, which has a smaller radius of 3.92 Å, compared to a large radius of 4.31 Å in the $5^{12}6^2CH_4$ cage. Further, the magnitude of shift in bending modes of CH_4 in both the cages is smaller than their corresponding high frequency vibrational modes, which illustrates that bending modes are relatively less perturbed on encapsulation of CH_4 in these cages. The ν_3 mode of free CH_4 at 1518 cm^{-1} shows a slight blue-shift by 8 cm^{-1} in the $5^{12}CH_4$ cage and a red-shift of 1 cm^{-1} in the $5^{12}6^2CH_4$ cage (Table **3.1**, row 3). However, the shifts in the rocking modes are much lower than the bending modes which suggest that rocking modes are less affected by the encapsulation of CH_4 molecules in the cages. The ν_4 mode of water molecules in the $5^{12}CH_4$ and $5^{12}6^2CH_4$ cages shows a blue-shift (Table **3.1**, row 4) compared to free H_2O due to the presence of strong hydrogen bonding interactions among water molecules in the cages. The ν_4 mode of water molecules in the $5^{12}6^2CH_4$ cage shows a larger blue-shift compared to the $5^{12}CH_4$ cage due to more number of hydrogen bonded interactions among water molecules in the $5^{12}6^2CH_4$ cage.

3.2.4 Low frequency region

The low frequency vibrations correspond to collective vibrations of water molecules in the cages which twist (or rotate) about their equilibrium lattice positions. These collective vibrations are called as librational modes and are known to offer vital information about the nucleation and growth mechanisms of clathrate hydrates [154, 155]. The librational spectrum region for various cages is shown in Figure **3.5** and **3.6**. The frequency range of the librational modes ν_1 in various cages is shown in row 1 of Table **3.1**. The encapsulation of CH_4 in the $5^{12}CH_4$ and $5^{12}6^2CH_4$ cages shows an increase in the range of the frequencies compared to the corresponding 5^{12} and $5^{12}6^2$ cages and this could be due to the vibrational motion of the encapsulated CH_4 in these cages. While the librational modes are largely driven by the collective motions of a large number of water molecules in these cages,

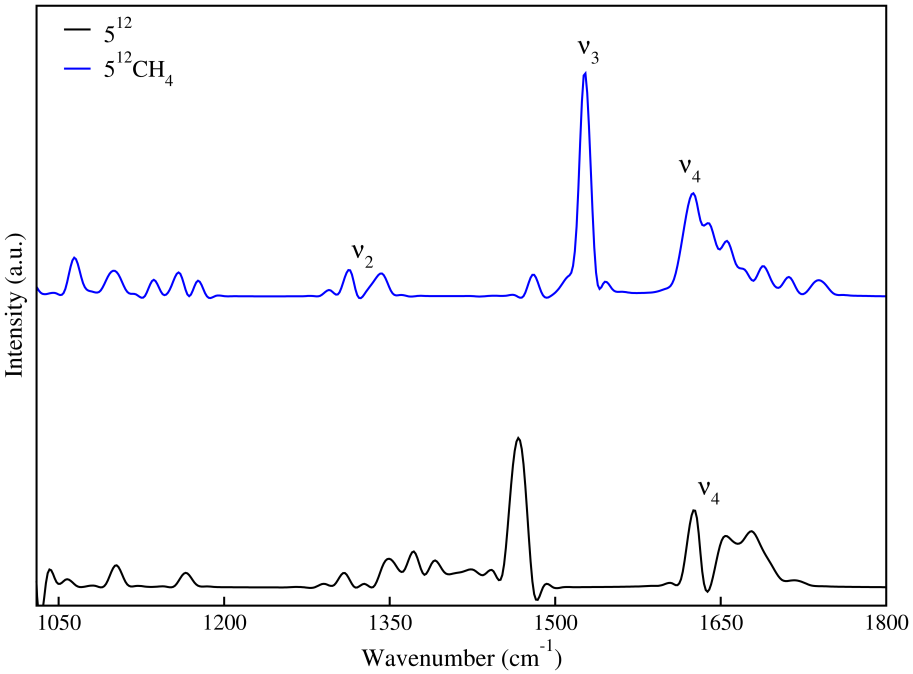

Figure 3.3: Mid-frequency Raman spectra of 5^{12} and $5^{12}CH_4$ cages.

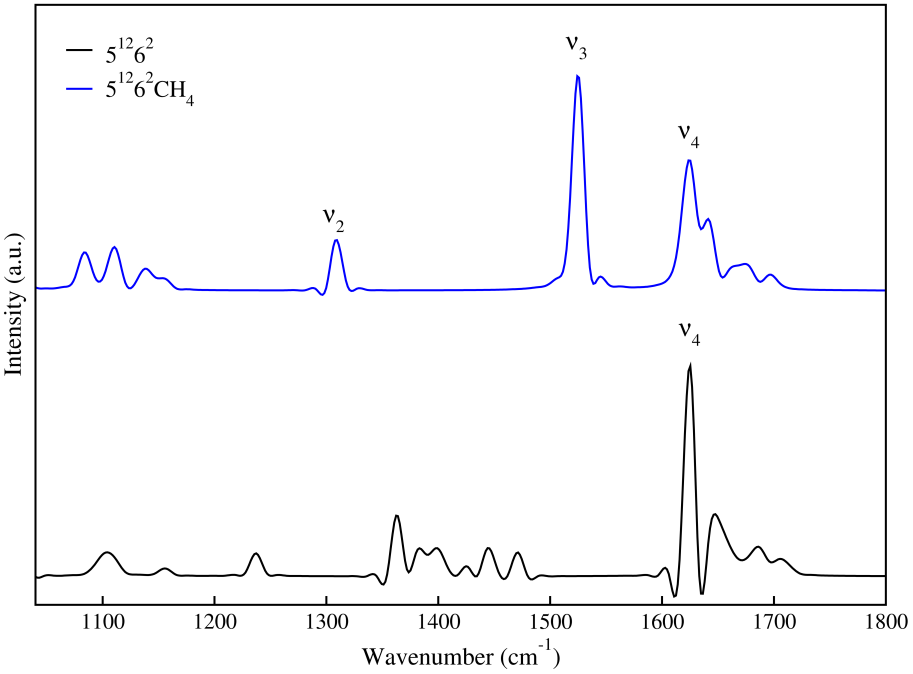

Figure 3.4: Mid-frequency Raman spectra of $5^{12}6^2$ and $5^{12}6^2CH_4$ cages.

some of these modes also show the vibrational motion of the encapsulated CH_4 molecule. For example, in the $5^{12}CH_4$ cage, the librational modes at 14 cm^{-1} and 190 cm^{-1} show CH_4 and water modes become a collective motion of water molecules. Similar trends in librational modes are seen in the $5^{12}6^2CH_4$ cage. The broad span of frequencies from the librational modes suggest that these cages come together to form a hydrate lattice.

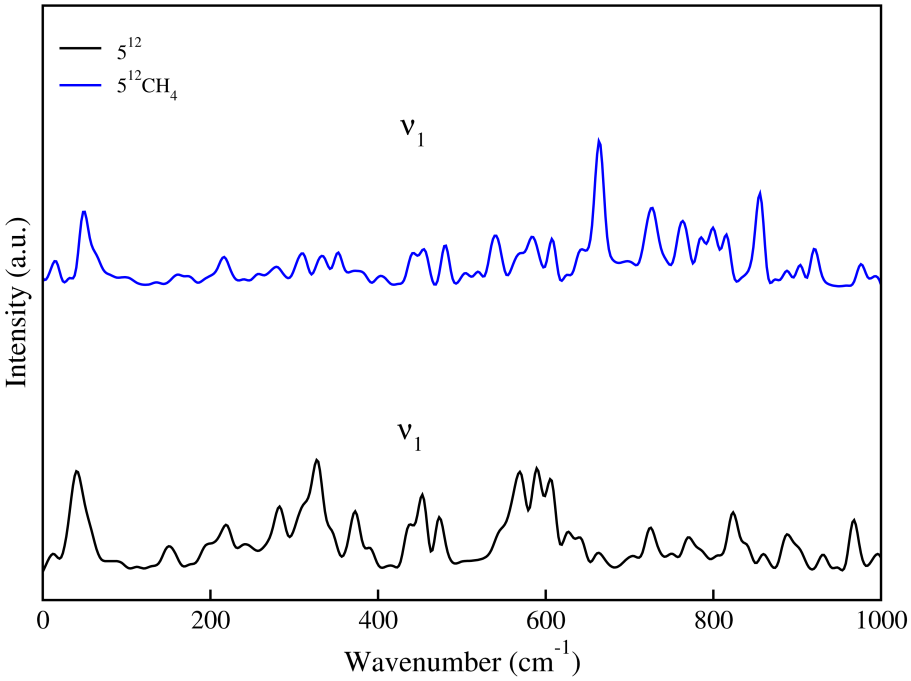

Figure 3.5: Low frequency Raman spectra of 5^{12} and $5^{12}CH_4$ cages.

3.3 Conclusions

The various modes of vibrations in 5^{12} and $5^{12}6^2$ cages of methane clathrate hydrates has been characterized using the DFT method. It has been observed that the high frequency vibrational modes of water molecules in the $5^{12}CH_4$ and $5^{12}6^2CH_4$ cages are red-shifted. The bending modes in the $5^{12}CH_4$ and $5^{12}6^2CH_4$ cages are blue shifted though the magnitude of shift is lower than the shifts in the high frequency region. Further, the rocking modes are less affected by the encapsulation of CH_4 molecule. All vibrational modes of CH_4 in the $5^{12}6^2CH_4$ cage are red shifted compared to the $5^{12}CH_4$ cage due to the larger

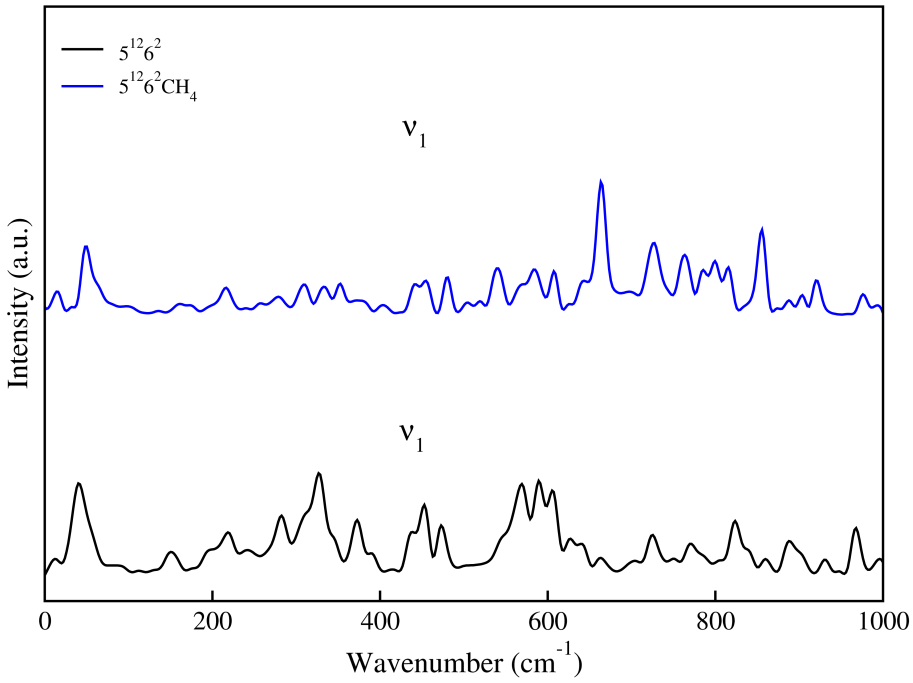

Figure 3.6: Low frequency Raman spectra of $5^{12}6^2$ and $5^{12}6^2CH_4$ cages.

cavity radii which reduces the dispersive interactions between the encapsulated CH_4 and water molecules of the cages. The broad span of frequencies from librational modes of CH_4 and water molecules in these cages suggest that this could be the driving force behind the formation of the hydrate lattice. In the next chapter, the reaction mechanism involved in the formation of methane clathrate hydrates is discussed.

Chapter 4

Reaction mechanism of methane clathrate hydrates

4.1 Introduction

A large number of MD simulations [12, 31–34, 106–122] are devoted to the nucleation and formation of clathrate hydrates. However, whether the formation of clathrate hydrates requires the presence of gas molecules still remains a debatable issue [7]. Matsumoto et. al. [116] observed the formation of clathrate hydrates in the absence of gas molecules. However, recent MD simulations have shown the formation of clathrate hydrates also occur in the presence of gas molecules [31–34, 110, 118–122]. Roman-Perez et. al. [127] and Li et. al. [128] characterized the energetics and kinetics of clathrate hydrates using DFT and CI-NEB method. The authors observed that the activation energy is large for diffusion of CH_4 in fused cages of clathrate hydrates. Further, the authors provided limited qualitative insights into various pathways of diffusion of CH_4 in the 5^{12} and $5^{12}6^2$ cages. The objective of this work is to examine the structural effects, energetics, kinetics of diffusion of CH_4 molecule via the pentagonal and hexagonal gates of 5^{12} and $5^{12}6^2$ cages. Additionally the diffusion of CH_4 in various fused cages (a cage formed from two cages) is also examined. In this chapter the word "diffusion" refers to the translational motion of a methane molecule via two possibilities: A) from a non-interacting state to the center

of the cage, B) from a center of one cage to the center of an adjacent cage (fused cages). The computational details are described in Section 4.2. The various properties associated with diffusion of CH_4 in various cages presented in the Section 4.3. A summary of salient results concludes this chapter.

4.2 Computational details

The calculations were performed using the projector augmented wave pseudopotential [156] and dispersion corrected D3 [67], vdw-DF1 [68] and vdw-DF2 [69] functionals. The cages considered for diffusion of CH_4 are 5^{12}, $5^{12}6^2$ and fused cages. The fused cages are: $5^{12}6^2 \overset{Pen}{\longleftrightarrow} 5^{12}$ ($5^{12}6^2$ and 5^2 cages fused via the pentagonal gate). $5^{12}6^2 \overset{\text{Pen}}{\longleftrightarrow} 5^{12}6^2$ (two $5^{12}6^2$ cages fused via the pentagonal gate). $5^{12}6^2 \overset{\text{Hex}}{\longleftrightarrow} 5^{12}6^2$ (two $5^{12}6^2$ cages fused via the hexagonal gate). Geometry optimization was performed on all the polyhedral water cages until force on each atom was less than 0.005 eV per Å. The kinetic-energy cutoff chosen was 500 eV and reciprocal space integrations were performed at the Γ point. A schematic representation of reactants and products is shown in Figure **4.1**. The reactant is defined as a CH_4 molecule non interacting with the polyhedral water cage. The product is defined as the CH_4 encapsulated in the center of the polyhedral water cage. The MEP for the diffusion of CH_4 in various cages is calculated using the CI-NEB method [85].

4.3 Results and discussion

4.3.1 Structure and Energetics

The structural characteristics of reactants and products is compared with experimental data [157] and previously reported theoretical data (see Table **4.1**). An overall examination shows that all bond lengths and angles of reactants and products are in agreement with theoretical data (DF) and the experimental work of Kirchner et. al. [157]. The optimized reactants and products shows similar O-H covalent bond lengths which suggest that the inclusion of CH_4 molecule does not distort the cages significantly. The experimental distances (d_{O-H}) differ from theoretical calculations due to the difficulty of accu-

rate determination of hydrogen atom positions from XRD. Further, small deviations in the non-bonded lengths and angles can be attributed to the various exchange correlation functionals used in this study.

In order to characterize the effect of diffusion of CH_4 in these cages, we define the ad-

Table 4.1: Average bond distances (Å) and bond angles (°) for the reactant and products. Standard deviations are given in parenthesis.

Functionals	$d_{O..H}$ (b)	$d_{O..H}$(nb)	$d_{O..O}$(nb)	<H-O-H (nb)	<O-O-O (nb)
			Reactant		
D3	0.980 (0.010)	1.716 (0.100	2.749 (0.064)	108.8 (1.3)	109.3 (4.4)
DF1	0.981 (0.007)	1.820 (0.113)	2.817 (0.101)	108.6 (2.3)	107.7 (2.6)
DF2	0.981 (0.007)	1.817 (0.101)	2.810 (0.092)	108.2 (2.4)	108.8 (3.7)
			Product		
D3	0.984 (0.010)	1.716 (0.100)	2.748 (0.062)	109.1 (1.7)	107.7 (2.5)
DF1	0.980 (0.006)	1.860 (0.110)	2.848 (0.103)	108.9 (2.1)	107.7 (2.5)
DF2	0.981 (0.007)	1.819 (0.100)	2.810 (0.091)	108.6 (2.8)	108.8 (3.4)
DF[a]	0.994 (0.001)	1.790 (0.014)	2.781 (0.010)	107.1 (1.0)	108.6 (4.0)
Experiment[b]	0.861 (0.031)	1.911(0.022)	2.761 (0.020)	109.3 (3.0)	108.7 (3.7)

b - Bonded hydrogen, nb - non-bonded hydrogen
[a]Ref - [128], [b]Ref - [157]

Table 4.2: Adsorption energies (kcal/mol) of CH_4 in 5^{12} and $5^{12}6^2$ cages.

Functionals	Adsorption Energy	Adsorption Energy
D3	-7.84	-6.46
DF1	-9.92	-8.07
DF2	-8.07	-6.92
DF[a]	-9.22	-8.07

[a]Ref - [128]

sorption energy as the energy difference between the product and the reactant. A negative value of adsorption energy implies that CH_4 encapsulated in the cage is more stable compared to CH_4 with the non-interacting water cage. As seen in the Table **4.2**, an adsorption

energy of CH_4 in the 5^{12} cage shows more stability compared to $5^{12}6^2$ cage (for all functionals). The adsorption energies (CH_4 in 5^{12} and $5^{12}6^2$ cages) from D3 and DF2 functionals are in close agreement, whereas DF1 functional predicts a higher adsorption energy. However, all adsorption energies are in agreement with a previously reported calculation (using DF functional) [128]. Since no experimental data is available, the calculated adsorption energy can serve as a valuable tool for any possible experimental investigation. The activation energy and rate constants for diffusion of CH_4 molecule via various gates of 5^{12} and $5^{12}6^2$ cages is described in the next section.

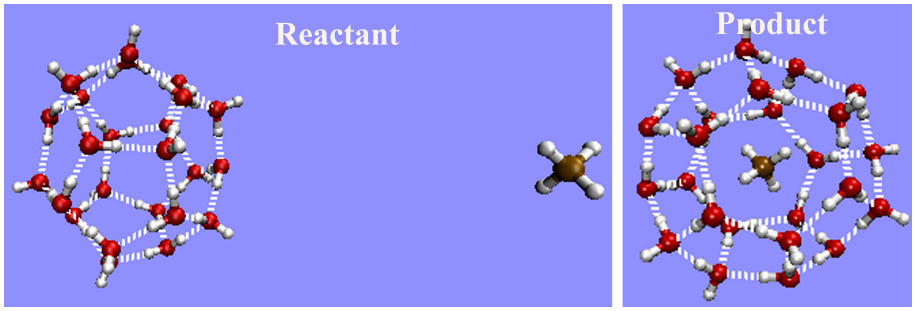

Figure 4.1: Schematic representation of reactants and products.

4.3.2 Activation energy of diffusion of the CH_4 in 5^{12} and $5^{12}6^2$ cages

The activation energy for the diffusion of CH_4 molecule can be examined via three pathways: i) via the pentagonal gate of the 5^{12} cage. ii) via the pentagonal gate of the $5^{12}6^2$ cage. iii) via the hexagonal gate of the $5^{12}6^2$ cage. A schematic representation of diffusion of CH_4 via the pentagonal and hexagonal gate is shown in Figure **4.2**.

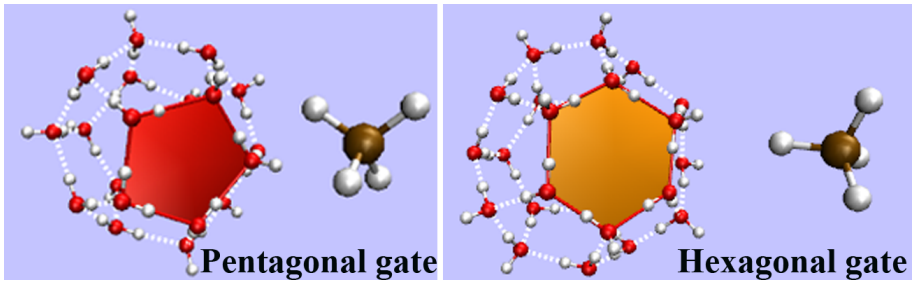

Figure 4.2: Schematic representation of diffusion of CH_4 via the pentagonal and hexagonal gate.

4.3.2.1 Diffusion of CH_4 via the pentagonal gate of 5^{12} and $5^{12}6^2$ cages

The MEP for the diffusion of CH_4 via the pentagonal gate of the 5^{12} and $5^{12}6^2$ cages are shown in Figure 4.3. A closer examination of MEP shows an interacting state and transition state (see Figures 4.3 and 4.4). The structural parameters of the reactant, product, interacting state and transition state is shown in Tables 4.3 (5^{12} cage) and 4.4 ($5^{12}6^2$ cage), respectively. At the interacting state, the CH_4 molecule is at a distance of $\sim$ 3.6 Å from the center of the pentagonal gate in the 5^{12} cage, and at a distance of $\sim$ 2.7 Å from the center of the pentagonal gate in the $5^{12}6^2$ cage. In the transition state, the CH_4 molecule is located in the center of the pentagonal gate for both cages. An examination of the area of the pentagonal gate (of 5^{12} and $5^{12}6^2$ cages) and the average O-H (nb) distance which forms the pentagonal gate in various states (reactant, product, interacting state and transition state) shows the following trends: The reactant and product show similarity in the pentagonal area which suggest that these cages are relaxed. Compared to the reactant and product, the interacting state shows a slight increase in the area of the pentagonal gate and average O-H (nb) distance which suggest that CH_4 molecule is in line of interaction with the pentagonal gate. In the transition state, the pentagonal area of the 5^{12} cage increases by a factor of 1.08 - 1.16 and O-H (nb) length by a factor of 1.13, compared to the interacting state. However, the diffusion of CH_4 molecule via the pentagonal gate of the $5^{12}6^2$ cage, shows an increase in pentagonal area by a factor of 1.97 - 2.11 and O-H (nb) length by a factor of 1.25, in the transition state, compared to the interacting state. This suggest that at the transition state, the pentagonal gate (of 5^{12} and $5^{12}6^2$ cages) fully expands to allow the incoming CH_4 molecule to diffuse (see right panel of Figures 4.3 and 4.4 respectively).

4.3.2.2 Diffusion of the CH_4 via the hexagonal gate of the $5^{12}6^2$ cage

The MEP for the diffusion of CH_4 molecule via the hexagonal gate for the $5^{12}6^2$ cage is shown in Figure 4.5. The structural parameters of the reactant, product, interacting state and transition state is shown in Table 4.5. Similar to the trends seen in the diffusion of CH_4 via the pentagonal gate in the 5^{12} and $5^{12}6^2$ cages, the diffusion of CH_4 via the hexagonal

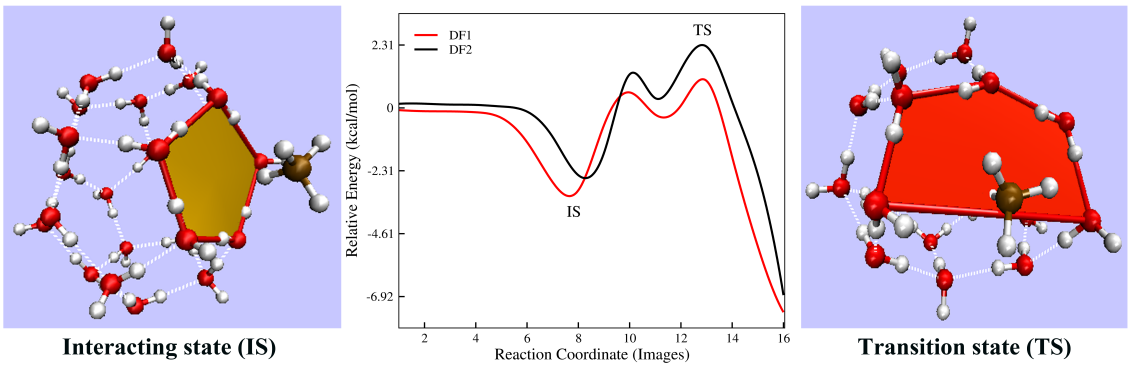

Figure 4.3: Activation energy of diffusion of CH_4 via the pentagonal gate of the 5^{12} cage.

Table 4.3: Structural properties of the pentagonal gate in the 5^{12} cage.

Structure	**Area of the pentagon (Å^2)**	**d_{O-H}(nb) (Å)**
	DF1	
Reactant	19.93	1.77
Product	19.81	1.76
Interacting state	19.99	1.87
Transition state	21.63	2.11
	DF2	
Reactant	19.25	1.78
Product	19.23	1.76
Interacting state	19.27	1.87
Transition state	22.31	2.13

gate shows the hexagonal area of reactant and product are very similar. Similarly, the interacting state shows a slight increase in the hexagonal area and the average O-H (nb) distance, compared to the reactant and product. In the transition state, the hexagonal area (see right panel of Figure 4.5) of the $5^{12}6^2$ cage increases by a factor of 1.65 - 1.39 and the O-H (nb) length by a factor of 1.36 - 1.24, compared to the interacting state.

The activation energy of diffusion of CH_4 in 5^{12} and $5^{12}6^2$ cages are shown in Table 4.6. The D3 functionals predicts higher activation energy compared to DF1 and DF2

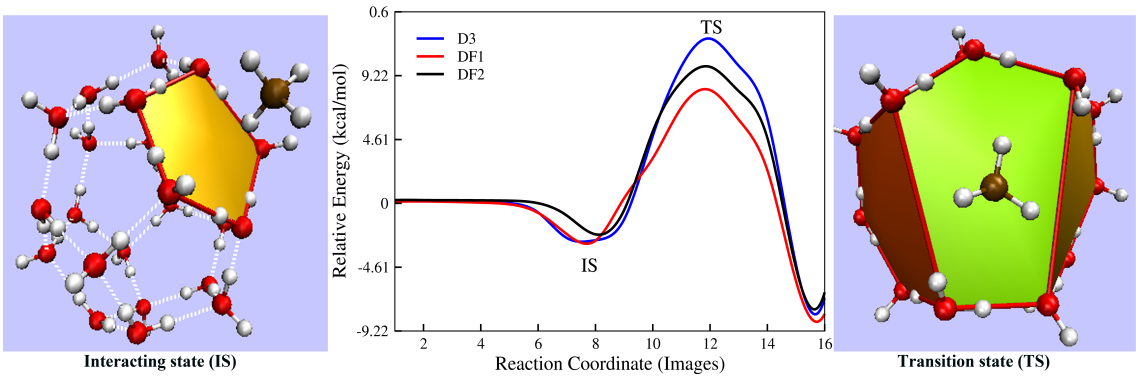

Figure 4.4: Activation energy of diffusion of CH_4 via the pentagonal gate of the $5^{12}6^2$ cage.

Table 4.4: Structural properties of the pentagonal gate in the $5^{12}6^2$ cage.

Structure	**Area of the pentagon (Å^2)**	**d_{O-H}(nb)** (Å)
	D3	
Reactant	12.69	1.76
Product	12.66	1.75
Interacting state	13.22	1.87
Transition state	27.12	2.34
	DF1	
Reactant	13.85	1.77
Product	13.82	1.76
Interacting state	14.14	1.87
Transition state	27.83	2.25
	DF2	
Reactant	13.66	1.76
Product	13.61	1.76
Interacting state	13.71	1.87
Transition state	28.97	2.25

functionals, where these energies differ by a maximum of 4 kcal/mol between DF1 and DF2 functionals. The lowest activation energy are seen from the diffusion of CH_4 via the

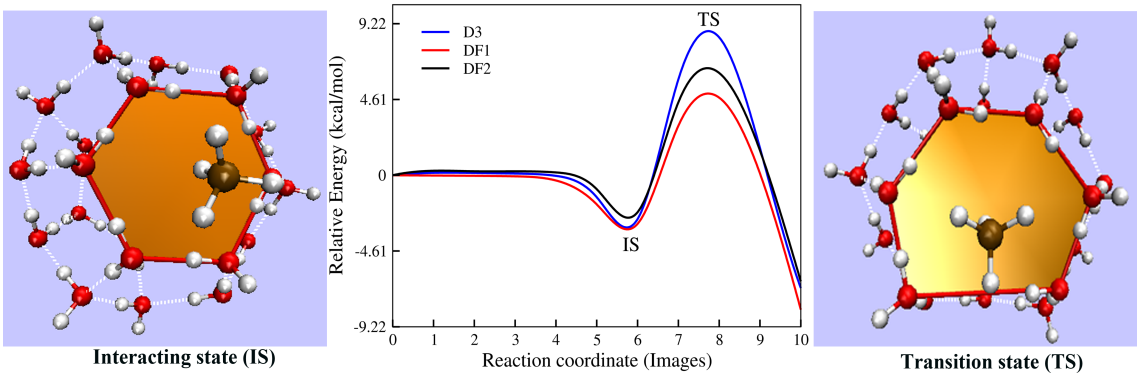

Figure 4.5: Activation energy of diffusion of CH_4 via the hexagonal gate of the $5^{12}6^2$ cage.

Table 4.5: Structural properties of the hexagonal gate in the $5^{12}6^2$ cage.

Structure	**Area of the hexagon ($Å^2$)**	**d_{O-H}(nb)** (Å)
	D3	
Reactant	18.38	1.65
Product	18.37	1.65
Interacting state	18.28	1.65
Transition state	25.74	2.05
	DF1	
Reactant	19.87	1.78
Product	20.33	1.81
Interacting state	20.29	1.82
Transition state	28.25	2.43
	DF2	
Reactant	19.62	1.77
Product	19.65	1.77
Interacting state	19.88	1.79
Transition state	32.91	2.43

pentagonal gate of the 5^{12} cage (0.99 - 2.24 kcal/mol), and the highest activation energy is observed from the diffusion of CH_4 via the pentagonal gate of the $5^{12}6^2$ cage (8.07 - 11.99

Table 4.6: Activation energy (kcal/mol) of diffusion of CH_4 in 5^{12} and $5^{12}6^2$ cages.

Functionals	5^{12} (Pentagonal gate)	$5^{12}6^2$ (Pentagonal gate)	$5^{12}6^2$ (Hexagonal gate)
D3	-	11.99	8.30
DF1	0.99	8.07	4.61
DF2	2.24	9.68	6.23

kcal/mol). An intermediate activation energy (6.23 - 8.30 kcal/mol) is observed for the diffusion of CH_4 via the hexagonal gate of the $5^{12}6^2$ cage. The differences in activation energy can be mathematically understood from the difference in area of the transition state and the reactant of the corresponding cages. This is illustrated by choosing a DF2 functional. In the 5^{12} cage, the difference in area of the pentagonal gate is 3.06 Å^2, whereas in the $5^{12}6^2$ cage, the difference in area of the pentagonal gate is 15.31 Å^2. In the $5^{12}6^2$ cage, the difference in area of the hexagonal gate is 13.28 Å^2. Similar trends are also seen from the use of D3 and DF1 functionals.

The rate constant (k), for diffusion of CH_4 in the 5^{12} and $5^{12}6^2$ cages is calculated using Arrhenius expression, where,

$$k = Ae^{-}\left(\frac{E_a}{k_b T}\right) \tag{4.1}$$

E_a is the activation energy, k_b is the Boltzmann constant. The k for diffusion of CH_4 molecule via the pentagonal gate of the 5^{12} cage is 10^8 times larger than the pentagonal gate of the $5^{12}6^2$ cage. The k for diffusion of CH_4 via the hexagonal gate is 10^2 times larger than the pentagonal gate in $5^{12}6^2$ cage. In the next section, the diffusion of CH_4 in various fused cages will be examined by the use of DF2 functional.

4.3.3 Activation energy of diffusion of CH_4 in fused water cages

A schematic representation of a fused cage is shown in Figure 4.6. The MEP for various fused cages is shown in Figure 4.7. The activation energy for the diffusion of CH_4

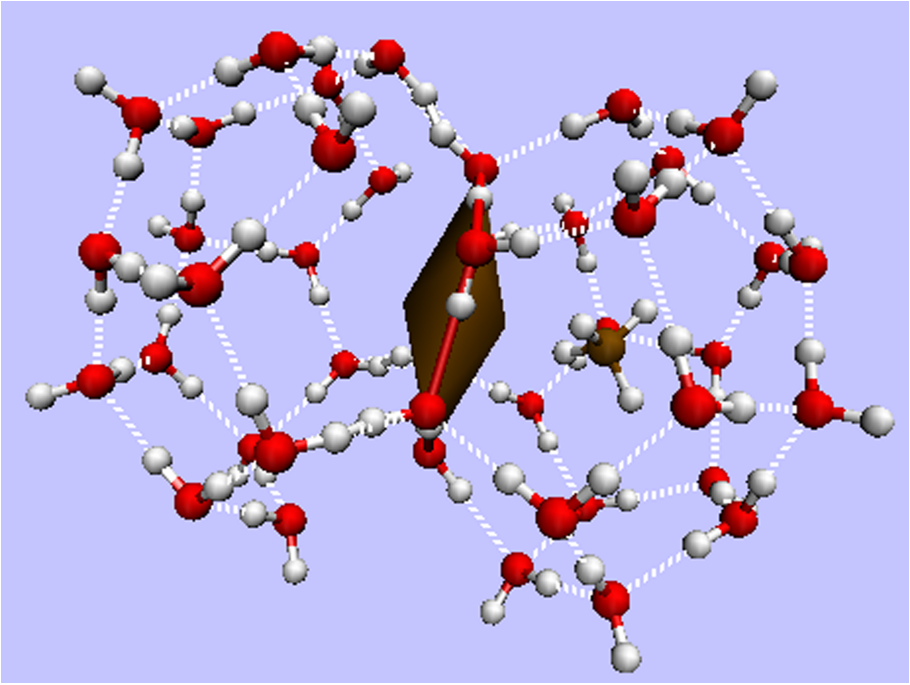

Figure 4.6: Schematic representation of fused water cages.

molecule via various gates in single and fused cages are shown in Table 4.7. A comparison of activation energy in fused cages shows the following features: the diffusion of CH_4 molecule via the pentagonal gate of the $5^{12}6^2$ cage to the 5^{12} cage ($5^{12}6^2 \overset{Pen}{\longleftrightarrow} 5^{12}$) results in the least activation energy (16.83 kcal/mol). However, the diffusion of CH_4 molecule via the hexagonal gate from one $5^{12}6^2$ cage to the adjacent $5^{12}6^2$ cage ($5^{12}6^2 \overset{Hex}{\longleftrightarrow} 5^{12}6^2$) shows a highest activation energy (20.98 kcal/mol). A comparison of activation energy between the fused and single cages shows the following trends: The activation energy for the diffusion of CH_4 in the $5^{12}6^2 \overset{Pen}{\longleftrightarrow} 5^{12}$ cage is 7.5 times higher than the 5^{12} cage (Pen). Similarly, activation energy for the diffusion of CH_4 in the $5^{12}6^2 \overset{Pen}{\longleftrightarrow} 5^{12}6^2$ cage is 1.8 times higher than the $5^{12}6^2$ cage (Pen). The activation energy for the diffusion of CH_4 in the $5^{12}6^2 \overset{Hex}{\longleftrightarrow} 5^{12}6^2$ cage is 3.3 times higher than the $5^{12}6^2$ cage (Hex). This illustrates that diffusion of CH_4 in the fused cages is lower compared to the corresponding single cages.

Table 4.7: Activation energy (kcal/mol) of diffusion of CH_4 in single and fused cages.

Cage	Activation energy	Fused cages	Activation energy
5^{12}(Pen)	2.24	$5^{12}6^2 \overset{\text{Pen}}{\longleftrightarrow} 5^{12}$	16.83
$5^{12}6^2$(Pen)	9.68	$5^{12}6^2 \overset{\text{Pen}}{\longleftrightarrow} 5^{12}6^2$	17.53
$5^{12}6^2$(Hex)	6.23	$5^{12}6^2 \overset{\text{Hex}}{\longleftrightarrow} 5^{12}6^2$	20.98

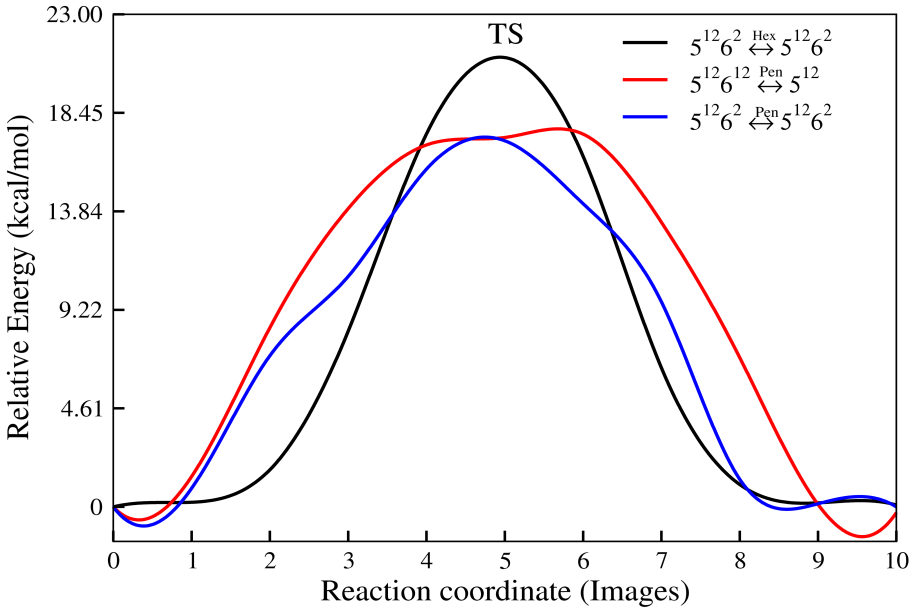

Figure 4.7: Activation energy of diffusion of CH_4 in fused water cages.

4.4 Conclusions

The various reaction pathways of diffusion of CH_4 in 5^{12} and $5^{12}6^2$ cages is characterized using CI-NEB method with three exchange correlation functionals (D3, DF1 and DF2). The adsorption energy shows that CH_4 molecule stabilizes 5^{12} and $5^{12}6^2$ cages. The activation energy is less when diffusion of CH_4 occurs via the hexagonal gate compared to the pentagonal gate of the $5^{12}6^2$ cage. The activation energy is less when diffusion of CH_4 occurs via the pentagonal gate in the 5^{12} cage compared to the pentagonal and hexagonal gate of $5^{12}6^2$ cage. A comparison of rate constants show that the fastest diffusion of CH_4 occurs via the pentagonal gate of the 5^{12} cage compared to other diffusion mechanisms.

The activation energy is least when diffusion of CH_4 occurs in $5^{12}6^2 \overset{Pen}{\longleftrightarrow} 5^{12}$ cages compared to $5^{12}6^2 \overset{Pen}{\longleftrightarrow} 5^{12}6^2$ and $5^{12}6^2 \overset{Hex}{\longleftrightarrow} 5^{12}6^2$ cages. The activation energy of the diffusion of CH_4 molecule in fused cages are higher than the single cages due to interfacial diffusion. The activation energies of fused cages can be considered as a reliable benchmark for diffusion of CH_4 in a hydrate lattice which comprised of several fused cages. In the next chapter, the thermodynamic stability and storage capacity of pure and THF doped cages of hydrogen clathrate hydrates is discussed.

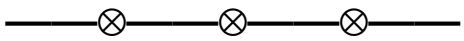

Chapter 5

Hydrogen storage in pure and tetrahydrofuran doped clathrate hydrates

5.1 Introduction

Hydrogen clathrate hydrates have attracted attention due to its ability to serve as a promising hydrogen storage material [158, 159]. Hydrogen clathrate hydrates form sII hydrate lattice. The characterization of storage of hydrogen has attracted several experimental investigations. For example, a first study performed by Mao et. al. [24, 25] showed a double occupancy of H_2 in the 5^{12} cage and a quadruple occupancy of H_2 in the $5^{12}6^4$ cage. Lokshin et. al. [160] synthesized hydrogen clathrate hydrates and characterized its stability using high pressure neutron diffraction techniques. The authors observed a single occupancy of H_2 in the 5^{12} cage and a quadruple occupancy of H_2 in the $5^{12}6^4$ cage at 220 Mpa and 200 K. While, the formation of pure hydrogen clathrate hydrates requires conditions of very high pressure, the addition of dopants like THF [161–163] was shown to reduce the thermodynamic conditions in which these clathrate hydrates can be formed (see Figure **5.1**). The general conclusions obtained from various experiments [164–169] show that depending on the concentration of THF, either a single or double occupancy

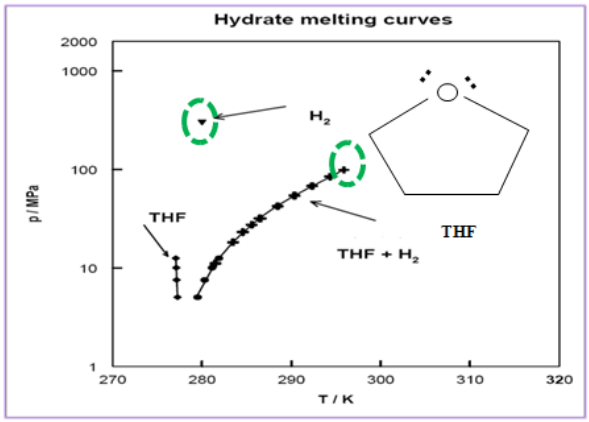

Figure 5.1: Phase diagram and stability regions of pure H_2 hydrate, pure THF hydrate and binary H_2/THF hydrate. (Adapted Florusse et. al. [163]. Copyright (2014) from Science)

of H_2 in the 5^{12} cage can be achieved. While, a maximum of quadruple occupancy of H_2 in the $5^{12}6^4$ cage was possible, the occupancy was found to decrease with increasing concentration of THF.

Computational methods based on MP2 and DFT has been employed to calculate hydrogen occupancies in 5^{12} and $5^{12}6^4$ cages. Calculations performed using *ab initio* calculations of Patchkovskii et. al. [41], Yedlapalli et. al. [170], Chattaraj et. al. [42] and Sotiris and co-workers [171] revealed a maximum of double occupancy in the 5^{12} cage and quadruple occupancy in the $5^{12}6^4$ cage. Alavi et. al. [172] employed MD simulations on pure hydrogen clathrate hydrates and observed only a single occupancy of H_2 in the 5^{12} cage and quadruple occupancy of H_2 in the $5^{12}6^4$ cage to be the most stable. Katsumasa et. al. [173] performed Monte Carlo (MC) simulations to investigate the thermodynamic stability of pure hydrogen clathrate hydrates. The authors observed a single occupancy of H_2 in the 5^{12} cage, though they could not observe a double occupancy of H_2 even at 500 Mpa. However, the authors observed a quadruple occupancy of H_2 in the $5^{12}6^4$ cage. A review of hydrogen storage in clathrate hydrates from experiments and theory is seen in the work of Struzhkin et. al. [16], Frankcombe et. al. [174] and Koh et. al. [175]

While, various theoretical studies have attempted to calculate hydrogen occupancy in the cages of pure hydrogen clathrate hydrates, the stability of single vs. double oc-

cupancy of H_2 in the 5^{12} cage still remains a contentious issue. Previous calculations [41, 42, 170, 171] on interaction energies have employed the exchange correlation functional which excludes dispersion required for the characterization of weak intermolecular interactions in water cages. Further, these studies have employed a frozen core approximation or a constrained geometry optimization on the cages. Except for the work of Xantheas and co-workers [171], other calculations have employed relatively small or modest basis sets. Ramya et. al. [176] compared interaction energy in methane clathrate hydrates using different DFT functionals and basis sets. The authors concluded that very large basis sets with a dispersion corrected B97-D [66] exchange correlation functional is required for accurate characterization of interaction energy and spectra. Further, the authors observed that the calculated spectral properties [177, 178] were in excellent agreement with experiment. In the present chapter, the interaction energy, free energy and storage capacity of hydrogen occupied pure and THF doped 5^{12} and $5^{12}6^4$ cages using the B97-D functional and a cc-pVTZ basis set is presented. The computational details are presented in Section 5.2. The interaction energy and free energy results are described in Section 5.3. A summary of important results concludes this chapter.

5.2 Computational details

All the calculations were performed using B97-D functional and cc-pVTZ basis set. The 5^{12} and $5^{12}6^4$ cages were chosen where varying amount of hydrogen molecules can be encapsulated. The input configurations of these cages were obtained as follows: Four configurations of 5^{12} cages which differ in symmetry Ci (Structure S1), C5 (Structure S2), S10 (Structure S3) and dodecahedral min (Structure S4) were created using the cage coordinates of Ojamae and co-workers [129, 179]. The fifth configuration (Structure S5) was created by a random orientation of non-hydrogen bonded protons of the 5^{12} cage. In the $5^{12}6^4$ cages (since symmetry information is unknown), we created five structures (S1-S5) which differ in proton orientation using the cage coordinates of Sloan et. al. [7] For each structure, the input geometry of multiple occupancy of H_2 in 5^{12} and $5^{12}6^4$ cages (pure and THF doped) was created as follows: The input geometry of the $5^{12}(H_2)_{n=1,2}$ cages

were generated by an inclusion of a single H_2 molecule in the optimized $5^{12}(H_2)_{n=0,1}$ cages respectively. The input geometry of the $5^{12}6^4(H_2)$ cage was obtained by an inclusion of a single H_2 molecule in the optimized $5^{12}6^4$ cage. The input geometry of the $5^{12}6^4(H_2)_{n=2-4}$ cages were obtained by an inclusion of a single H_2 molecule in the optimized $5^{12}6^4(H_2)_{n=1-3}$ cages respectively. The input geometry of the $5^{12}6^4$.THF cage was created by an inclusion of THF in the $5^{12}6^4$ cage and re-optimized. The input geometry of the $5^{12}6^4(H_2)_{n=1,2}$.THF cages were obtained by an inclusion of a single H_2 molecule in optimized $5^{12}6^4(H_2)_{n=0,1}$.THF cages, respectively. Further, increasing H_2 occupancy in pure and THF doped 5^{12} and $5^{12}6^4$ cages leads to a disintegration of the cage structure. The structure of multiple occupancy of H_2 in 5^{12} and $5^{12}6^4$ cages are shown in Figures **5.2**, **5.3** and **5.4** respectively. The interaction energy in the cages of pure and THF doped hydrogen clathrate hydrates is calculated as:

$$\begin{aligned} IE &= E[cage.(H_2)_n] - E[cage] - nE[H_2] \\ IE &= E[5^{12}6^4.THF] - E[5^{12}6^4] - E[THF] \\ IE &= E[5^{12}6^4(H_2)_n.THF] - E[5^{12}6^4.THF] - nE[H_2] \end{aligned} \tag{5.1}$$

where, n is the number of hydrogen molecules, $E[H_2]$ is the total energy of an isolated hydrogen molecule. $E[cage.(H_2)_n]$ is the total energy of 5^{12} or $5^{12}6^4$ cage containing the encapsulated hydrogen molecule(s). E[cage] is the total energy of 5^{12} or $5^{12}6^4$ cage. $E[5^{12}6^4.THF]$ is the total energy of the $5^{12}6^4$.THF cage respectively. E[THF] and $E[5^{12}6^4(H_2)_n.THF]$ is the total energy of the THF molecule and $5^{12}6^4$.THF cage containing the encapsulated hydrogen molecule(s). For each cage and structure (S1- S5), the total energy (corrected for BSSE) is shown in Table **B5.1.**

The interaction energies calculated from the total energy are corrected for BSSE [132, 133] and ZPVE. We perform free energy calculations (at the optimized geometry) to characterize the spontaneity of formation of hydrogen occupied pure and THF doped cages at various temperatures (T = 1 K, 100 K, 200 K, 270 K) and pressure (P = 1 Mpa, 50 Mpa, 100 Mpa, 200 Mpa and 250 Mpa). The change in free energy which denotes the

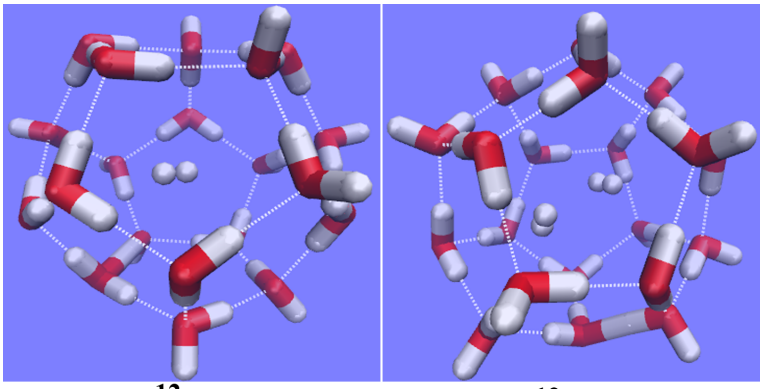

Figure 5.2: Structure of multiple occupancy of H_2 in the 5^{12} cage.

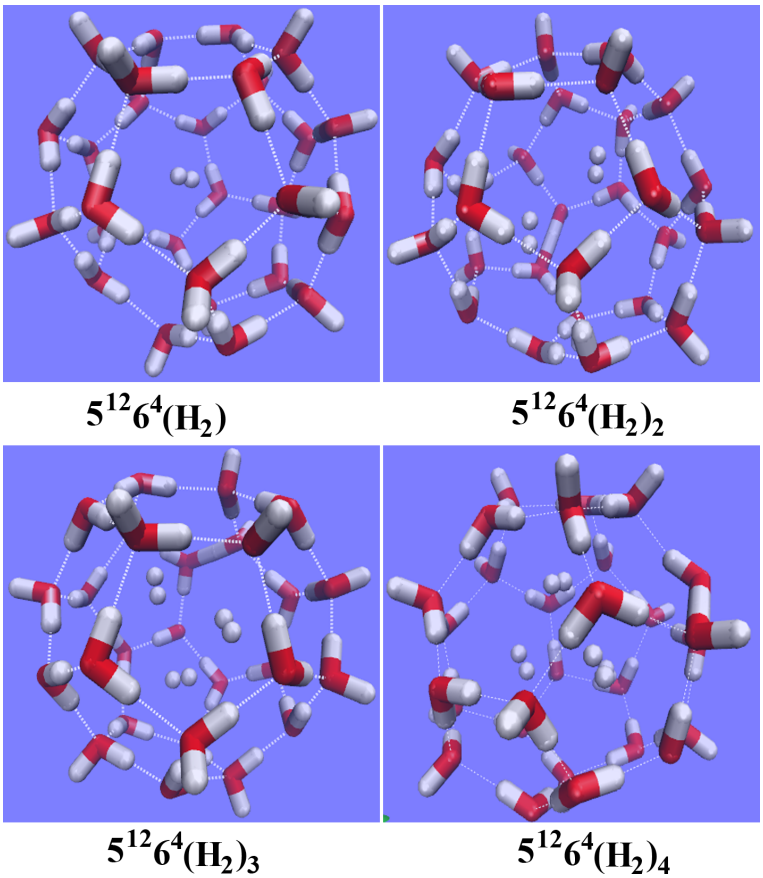

Figure 5.3: Structure of multiple occupancy of H_2 in $5^{12}6^4$ cages.

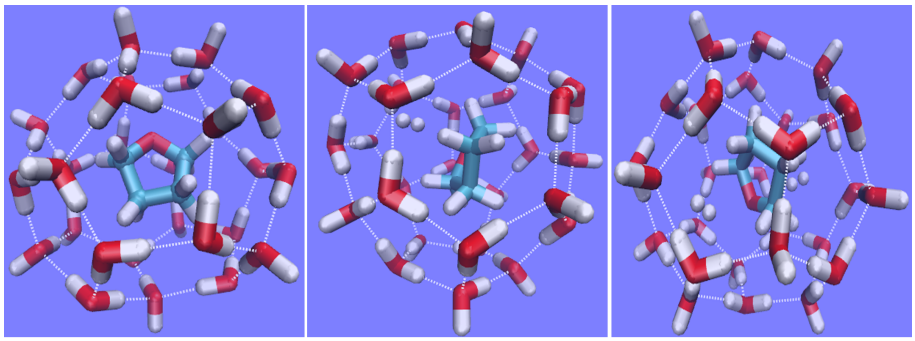

$5^{12}6^4$.THF $5^{12}6^4(H_2)$.THF $5^{12}6^4(H_2)_2$ .THF

Figure 5.4: Structure of multiple occupancy of THF in pure and H_2 doped $5^{12}6^4$ cages.

spontaneity of formation is written as:

$$\begin{aligned} \Delta G &= G[\text{cage}.(H_2)_n] - G[\text{cage}] - nG[H_2] \\ \Delta G &= G[5^{12}6^4.\text{THF}] - G[5^{12}6^4] - G[\text{THF}] \\ \Delta G &= G[5^{12}6^4(H_2)_n.\text{THF}] - G[5^{12}6^4.\text{THF}] - nG[H_2] \end{aligned} \tag{5.2}$$

where, n is the number of hydrogen molecules. $G[H_2]$ is the free energy of an isolated H_2 molecule. G[cage] is the free energy of the 5^{12} or $5^{12}6^4$ cages. $G[\text{cage}.(H_2)_n]$ is the free energy of the 5^{12} or $5^{12}6^4$ cages containing the encapsulated hydrogen molecule(s). $G[5^{12}6^4.\text{THF}]$ is the free energy of the $5^{12}6^4$.THF cage respectively. $G[5^{12}6^4(H_2)_n.\text{THF}]$ is the free energy of the $5^{12}6^4$.THF cage containing the encapsulated hydrogen molecule(s). G[THF] is the free energy of the THF molecule. The weight percentage of hydrogen in pure and THF doped hydrogen clathrate hydrates is calculated as:

$$wt\ \% = \left(\frac{M_H}{M_W + M_H}\right) \tag{5.3}$$

where, M_H is the total mass of occupied hydrogen molecules in the water cages ((p*16 + q*8)*2). p and q represents the maximum occupancy of H_2 which shows spontaneity of formation (obtained from free energy) in 5^{12} and $5^{12}6^4$ cages respectively. M_W is the total mass of the water molecules (136*18).

5.3 Results and Discussion

5.3.1 Interaction energy

For each cage and structure (S1- S5), the interaction energy and ZPVE contributions is shown in Table **B5.2**. A large negative and positive value of interaction energy denotes more stability and unstability, respectively. The average interaction energy and ZPVE contributions (calculated using Table **B5.2**) is shown in Table **5.1**. The interaction energy in the $5^{12}(H_2)$ cage shows the following trends: The interaction energy in the $5^{12}(H_2)$ cage is -2.09 kcal/mol, whereas the interaction energy in the $5^{12}(H_2)_2$ cage is 0.35 kcal/mol, which show that the $5^{12}(H_2)$ cage is more stable compared to the $5^{12}(H_2)_2$ cage. As seen from Table **5.1**, the trends in our calculated interaction energy are in qualitative agreement with the DFT calculations of Patchkovskii et. al. [41] and Chattaraj et. al. [42] The quantitative differences arise due to the dispersion corrected B97-D functional employed in this study. A triple occupancy of H_2 in the 5^{12} cage could not be achieved due to the deformation of the 5^{12} cage.

The interaction energy in the $5^{12}6^4(H_2)$ cage is -1.65 kcal/mol. The interaction energy increases with occupancy of H_2 molecules in the $5^{12}6^4$ cage, where the $5^{12}6^4(H_2)_4$ cage (-4.80 kcal/mol) was found to be the most stable. A quintiple occupancy of H_2 in the $5^{12}6^4$ cage could not be achieved due to the deformation of the $5^{12}6^4$ cage. The maximum stability of the $5^{12}6^4(H_2)_4$ cage is consistent with the experimental observations of Mao et. al. [24, 25], MD simulations of Alavi et. al. [172] and MP2 calculations (see Table **5.1**) of Patchkovskii et. al. [41] In order to investigate the effect of THF, we have calculated the interaction energy in pure and H_2 occupied (single and double occupied) $5^{12}6^4$.THF cages. An examination of the interaction energy shows the $5^{12}6^4$.THF cage is most stable compared to $5^{12}6^4(H_2)$.THF and $5^{12}6^4(H_2)_2$.THF cages (see Table **5.1**). This suggests that inclusion of THF is essential to stabilize the $5^{12}6^4$ cage before hydrogen molecules can be encapsulated. A comparison of interaction energy shows that the $5^{12}6^4(H_2)$.THF cage is more stable compared to the $5^{12}6^4(H_2)$ cage, which also illustrates THF enhances the stability of the cage. However, the $5^{12}6^4(H_2)_2$.THF cage show lower stability compared

to the $5^{12}6^4(H_2)_2$ cage, which demonstrate that the double occupancy of (H_2) is less stable in THF doped $5^{12}6^4$ cages. As expected, the contributions from ZPVE increases with increasing hydrogen occupancy in pure and THF doped 5^{12} and $5^{12}6^4$ cages. Our calculated ZPVEs are in agreement with the ZPVEs reported from the Diffusion Monte Carlo simulations of Bacic and co-workers [180].

5.3.2 Free energy

An examination of thermodynamic stability is seen from the free energy of formation of the hydrogen occupied cages. For each cage, we choose the optimized geometry of structure S5 for performing free energy calculations. The change in free energy with temperature (P = 250 Mpa) and pressure (T = 270 K) on encapsulation of hydrogen in various cages is shown in Figure **5.5**. The temperature dependence (at P = 250 Mpa) on free energies is shown in Figure **5.5(d-f)**. The free energy shows that the $5^{12}(H_2)$ cage is spontaneously formed at T ≤ 270 K. However, the less stable $5^{12}(H_2)_2$ cage is spontaneous only at T ≤ 100 K. Similarly, the free energy of formation of $5^{12}6^4(H_2)_{n=1-4}$ and $5^{12}6^4(H_2)$.THF cages shows spontaneity at T less than 270 K. However, the less stable $5^{12}6^4(H_2)_2$.THF cage is spontaneous only at T ≤ 100 K. The pressure dependence study (at T = 270 K) on free energies is shown in Figure **5.5(a-c)**. The $5^{12}(H_2)$ cage shows a spontaneous formation at P ≥ 50 Mpa and supports experimental observations at low pressure where a single occupancy of H_2 in the 5^{12} cage cannot be achieved due to structural peculiarities of the hydrate lattice. The formation of the $5^{12}(H_2)_2$ cage is non-spontaneous even at 250 Mpa and is consistent with the observations of Katsumasa et. al. [173] The $5^{12}6^4(H_2)_{n=1,2}$ cages show spontaneity of formation at P ≥ 50 Mpa, whereas the $5^{12}6^4(H_2)_{n=3,4}$ cages shows spontaneity at P ≥ 100 Mpa. An examination of the free energy shows the $5^{12}6^4$.THF cage is most stable compared to $5^{12}6^4(H_2)$.THF and $5^{12}6^4(H_2)_2$.THF cages (see Figure **5.5**). A comparison of free energy shows that the $5^{12}6^4(H_2)$.THF cage shows spontaneity of formation at P ≥ 1 Mpa which shows inclusion of THF leads to spontaneity at lower pressure. However, the formation of the $5^{12}6^4(H_2)_2$.THF cage is non-spontaneous even at 250 Mpa which shows inclusion of THF shows a double occupancy of H_2 is not feasible.

Table 5.1: Average interaction energy (includes BSSE and ZPVE) in kcal/mol for each occupancy of hydrogen in 5^{12} and $5^{12}6^4$ cages. ZPVE (kcal/mol) contributions to interaction energy in parenthesis.

Cage	Interaction energy (ZPVE)	Previous work DFT	MP2	(ZPVE[c])
$5^{12}(H_2)$	-2.09 (0.83)	-0.49[a], -1.08[b]	-1.84[a], -1.60[b]	-
$5^{12}(H_2)_2$	0.35 (3.23)	3.56[a],0.91[b]	-9.00[a],0.39[b]	-
$5^{12}6^4(H_2)$	-1.65 (0.92)	-0.87[a]	-0.54[a]	- (0.31)
$5^{12}6^4(H_2)_2$	-2.70 (1.29)	0.73[a]	-3.90[a]	- (1.16)
$5^{12}6^4(H_2)_3$	-3.46 (2.20)	3.41[a]	-5.77[a]	- (2.53)
$5^{12}6^4(H_2)_4$	-4.35 (2.84)	5.42[a]	-11.00[a]	- (3.67)
$5^{12}6^4$.THF	-19.38 (1.87)	-	-	- -
$5^{12}6^4(H_2)$.THF	-5.45 (1.39)	-	-	-
$5^{12}6^4(H_2)_2$.THF	-1.39 (3.86)	-	-	-

[a]Ref [41] (DFT/revPBE and MP2, 3-21G basis set).
[b]Ref [42] (DFT/B3LYP and MP2, 6-31G(d) basis set).
[c]Ref [180] (Diffusion Monte Carlo).

In order to compare with experiments, we have chosen the free energies of formation of various hydrogen occupied cages at 270 K to calculate the weight percentage of hydrogen storage in clathrate hydrates (see Eqn. **5.3**) and a comparison with experimental observations is shown in Table **5.2**. For example, the $5^{12}(H_2)$ and $5^{12}6^4(H_2)_4$ cages show

spontaneity of formation at P ≥ 100 Mpa. This results in a 3.77 wt % of hydrogen in pure hydrogen clathrate hydrates and is in agreement with the results of Florusse et. al. [163] (PXRD, Raman, NMR) and Lee et. al. [164] (Raman, NMR). Similarly, the formation of the $5^{12}(H_2)$ and $5^{12}6^4(H_2)$.THF cages is spontaneous at P ≥ 35 Mpa. This results in a 1.92 wt % of hydrogen in THF doped hydrogen clathrate hydrates and is in agreement with the observations of Lee et. al. [164] (Raman, NMR) and Sughara et. al. [169] (PXRD, Raman).

While hydrogen storage in clathrate hydrates is lower than DOE targets [181], these clathrate hydrates continue to attract attention due to facile synthesis at moderate pressure [24, 25] by appropriate choice of dopants, fast kinetics and ease of capture and retrieval of hydrogen [168] with minimal impact on environment (where only water is a by-product on release of hydrogen). Further, the quest for new dopants leading to enhanced hydrogen storage at moderate thermodynamic conditions can be one focus of future activities.

Table 5.2: Weight percentage of hydrogen in pure and THF doped hydrogen clathrate hydrates.

Literature	Method	Pure	THF doped
Mao et. al. [24]	Expt	5.3 % (220 Mpa, 249 K)	-
Florusse et. al. [163]	Expt	4 % (300 Mpa, 280 K)	1 % (5 Mpa, 280 K)
Lee et.al. [164]	Expt	4 % (200 Mpa, 270 K)	2.1 % (12 Mpa, 277 K)
Strobel et. al. [167]	Expt	-	1 % (13.8 Mpa, 270 K)
Rovetto et. al. [168]	Expt	-	1 % (70 Mpa, 20 K)
Sughara et. al. [169]	Expt	3.4 % (72 Mpa, 255 K)	2.2 % (72 Mpa, 255 K)
This work	DFT	3.77 % (100 Mpa,270 K)	1.92 % (35 Mpa, 270 K)

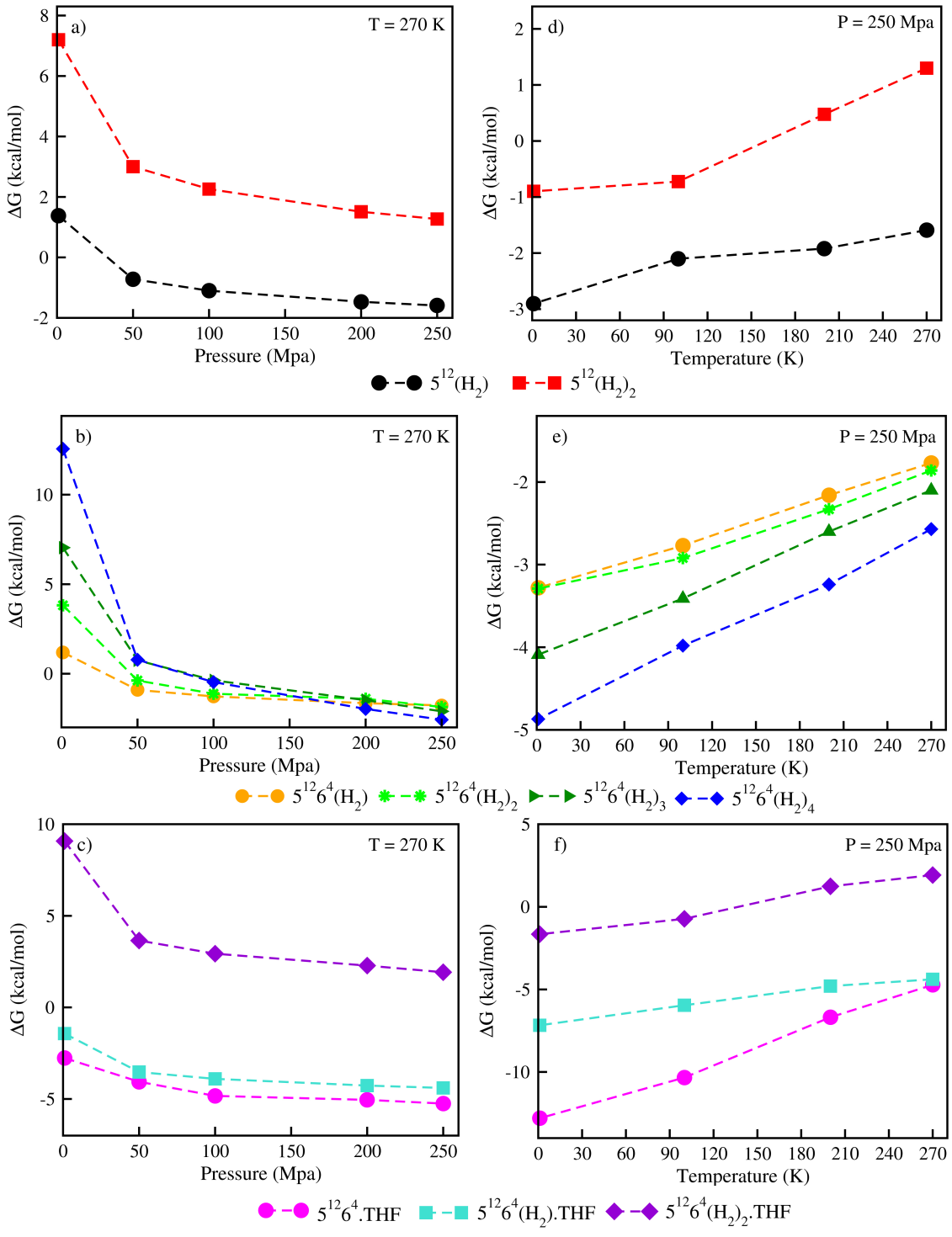

Figure 5.5: Change in free energies of formation of hydrogen occupied (a, d) 5^{12} cage, (b, e) $5^{12}6^4$ cage, (c, f) THF doped $5^{12}6^4$ cage.

5.4 Conclusions

The interaction energy, free energy and storage capacity of hydrogen in pure and THF doped hydrogen clathrate hydrates is calculated. The interaction energies show that the $5^{12}(H_2)$, $5^{12}6^4(H_2)_4$, $5^{12}6^4$.THF and $5^{12}6^4(H_2)$.THF cages have maximum stability, though higher occupancies with less stability are also found. At P = 250 Mpa, the $5^{12}(H_2)$, $5^{12}6^4(H_2)_{n=1-4}$ and $5^{12}6^4(H_2)$.THF cages are spontaneously formed at T $\leq$ 270 K. At T = 270 K, the $5^{12}(H_2)$ and $5^{12}6^4(H_2)_{n=1,2}$ cages are spontaneously formed at P $\geq$ 50 Mpa and the $5^{12}6^4(H_2)_{n=3,4}$ cage is spontaneously formed at P $\geq$ 100 Mpa. An examination of the interaction energy and free energy calculations suggest that the $5^{12}6^4$.THF cage is most stable compared to $5^{12}6^4(H_2)$.THF and $5^{12}6^4(H_2)_2$.THF cages. This suggests that inclusion of THF is essential to stabilize the $5^{12}6^4$ cage before hydrogen molecules can be encapsulated. The inclusion of THF in the $5^{12}6^4(H_2)$ cage reduces the pressure required for spontaneity of formation by two orders of magnitude. While, gas-phase thermo-chemistry in this study provides qualitative trends in free energies, an accurate determination of free energy using AIMD simulations on the hydrate lattice can be the focus of future activities. In the next chapter, the vibrational raman spectra associated with the single and multiple occupancy of pure and THF doped cages of hydrogen clathrate hydrates is discussed.

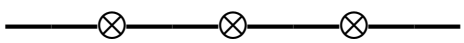

Chapter 6

Raman spectroscopy of pure and tetrahydrofuran doped hydrogen clathrate hydrates

6.1 Introduction

Raman spectroscopy techniques have been employed to determine the cage structures, hydrate composition and occupancy of hydrogen molecules in the cages of clathrate hydrates. For example, Mao et. al. [24, 25] synthesized pure hydrogen clathrate hydrates at high pressure (200-300 Mpa) and low temperature (240 K -249 K) and employed Raman spectroscopy to characterize spectral properties with multiple occupancy of H_2. The authors observed (from Raman vibronic spectra) a double occupancy of H_2 in the 5^{12} cage and quadruple occupancy of H_2 in the $5^{12}6^4$ cage. Strobel et. al. [182] employed Raman spectroscopy and observed that the encapsulation of H_2 in the 5^{12} and $5^{12}6^4$ cages leads to higher vibrational Raman frequencies of H_2, compared to free H_2 molecule. Similarly, Zaghloul et. al. [183] employed Raman spectroscopy and observed higher vibrational Raman shifts on encapsulation of H_2 in 5^{12} and $5^{12}6^4$ cages.

Experimental work have also focused on the spectroscopy of THF doped hydrogen clathrate hydrates [161–163]. This is due to the formation of stable hydrogen clathrate

hydrates at lower pressure by inclusion of THF. For example, Florusse et. al. [163] characterized THF doped hydrogen clathrate hydrates using PXRD, Raman and NMR spectroscopy techniques. The authors concluded that on inclusion of THF, the Raman vibronic peak for H_2 was seen only in the 5^{12} cages, whereas frequencies corresponding to the THF molecule were observed only in $5^{12}6^4$ cages. The occupancy of H_2 in THF doped hydrogen clathrate hydrates have also been investigated by several experiments [164–167, 169]. The general conclusions from these experiments suggest that depending on the concentration of THF and thermodynamic conditions, a single or a double occupancy of H_2 in the 5^{12} cage can be achieved. Further, a maximum of quadruple occupancy of H_2 in the $5^{12}6^4$ cage was possible, where the occupancy of H_2 decreases with increasing concentration of THF.

Bacic and co-workers [180] employed Diffusion Monte Carlo (DMC) simulations to study the quantum dynamics of H_2 in the $5^{12}6^4$ cages of the sII clathrate hydrate. The authors considered a rigid water cage framework and observed that ZPVE increase with increasing hydrogen occupancy in the cages. The authors characterized the translational and rotational (T-R) motions of H_2 molecules and concluded that a quadruple occupancy of H_2 in the $5^{12}6^4$ cage was most stable. Wang et. al. [184] performed DFT calculations using a B3LYP functional coupled with an ONIOM model to characterize spectral properties and cage occupancy in pure hydrogen clathrate hydrates. The authors observed that the calculated frequencies deviate significantly from experiments due to the limitations of the B3LYP functional in describing the weak inter-molecular interactions which exist in these cages.

While experimental investigations have provided insights into the thermodynamic conditions associated with the formation of these hydrates, the characterization of various vibrational Raman modes which occur on the encapsulation of H_2 and THF molecules in the cages of the sII hydrate lattice has never been attempted. Though, experiments have been performed on the hydrate lattice, the individual cages has been examined in this chapter which serve as constituent building blocks of the hydrate lattice. The choice of individual cages makes it computationally viable to accurately characterize various vibra-

tional modes by quantum chemistry methods and this is the objective of the present study. In this chapter, we have employed DFT using B97-1 [185] (uncorrected for dispersion) and B97-D [66] functionals. While, experiments have characterized the H-H vibrations in the cages of the hydrate lattice there has been hardly any insights on the effect of THF confinement with multiple occupancy of H_2 on the vibrational modes of water molecules. The objective of the present work is to characterize the vibrational Raman modes on encapsulation of multiple occupancy of H_2 in pure and THF doped 5^{12} and $5^{12}6^4$ cages using DFT (B97-D functional and cc-pVTZ basis set). Such a computational study can corroborate spectroscopic measurements performed to investigate the stability associated with multiple occupancy of H_2 in pure and THF doped hydrogen clathrate hydrates. Since, Raman spectroscopy [25, 182] have shown that change in pressure does not result in change in peak positions, the calculated gas-phase frequencies (in this study) can be considered as a reliable benchmark for comparison with experiments. The computational details are described in Section 6.2. The summary of salient results are described in Section 6.3. A summary of important results concludes this chapter.

6.2 Computational details

The details of input configurations, geometry optimization of single and multiple occupancy of pure and THF doped 5^{12} and $5^{12}6^4$ cages are presented in Chapter 5 (see section 5.2). Vibrational Raman frequencies were calculated for the geometry optimized single and multiple occupancy of pure and THF doped 5^{12} and $5^{12}6^4$ cages. The deformation energies for these cages which predict the structural integrity after encapsulation is calculated. The deformation energy for the multiple occupancy of H_2 in the pure and THF doped 5^{12} and $5^{12}6^4$ polyhedral water cages is calculated as follows:

$$E_{def} = [E_{cage}] - E[cage]^{enc} \tag{6.1}$$

For example, the deformation energy of single occupancy of H_2 in the 5^{12} cage is calculated as: $[E_{cage}]$ is the total energy of the optimized 5^{12} and $5^{12}6^4$ cages, $E[cage]^{enc}$ is ob-

tained by removal of the H_2 molecule(s) from the optimized geometry of the $5^{12}(H_2)_{n=1,2}$, $5^{12}6^4(H_2)_{n=1-4}$ and $5^{12}6^4(H_2)_{n=1-2}$.THF followed by a single point energy calculation.

6.3 Results and Discussion

6.3.1 Geometry

The structural analysis of the multiple occupancy of H_2 molecules in the 5^{12} and $5^{12}6^4$ cages shows the following trends: The geometries of the optimized guest free cages are in agreement with the 5^{12} and $5^{12}6^4$ cage geometries obtained from X-ray crystallographic structures [7]. The arrangement of H_2 molecules in 5^{12} and $5^{12}6^4$ cages has the following features: The single occupancy of H_2 in 5^{12} and $5^{12}6^4$ cages prefers to stay in the center of the cage. The average H_2-H_2 distance in the $5^{12}(H_2)_2$ cage is 2.56 Å and is in agreement with DMC [180] and DFT [41] calculations performed on the 5^{12} cage. The average H_2-H_2 distance in the $5^{12}6^4(H_2)_2$ is 2.78 Å and the H_2 molecules are located near the hexagon networks of the $5^{12}6^4$ cage. The triple occupancy of H_2 in the $5^{12}6^4$ cage forms a triangular network having an average distance of 2.97 Å. However, in quadruple occupancy, the H_2 molecules are located at the faces of the hexagon network separated by an average distance of 3.03 Å. Our calculations were in agreement with the neutron diffraction study performed on D_2 clathrate hydrates by Lokshin et. al. [160] and with DFT calculations performed by Tse et. al. [41] on the individual cages.

6.3.2 Spectral properties of single occupancy

We have considered only single configuration for study in this section to examine the change in vibrational modes which occur on encapsulation of H_2 and THF in the 5^{12} and $5^{12}6^4$ cages.

6.3.2.1 Effect of dispersion on spectral properties

To investigate the effect of dispersion on spectral properties, we have considered two different functionals, B97-1 [185] functional (excludes the dispersion term from the B97-D

functional) and B97-D functional. A comparison of Raman frequencies calculated from the use of B97-D and B97-1 functionals is shown in Table **6.1**. The vibrational mode (ν_1) of an isolated H_2 molecule calculated using the B97-1 functional is in agreement with the results of Wang et. al. [184] from a B3LYP functional. However, the ν_1 mode of an isolated H_2 molecule obtained using the B97-D functional shows a deviation from the ν_1 mode calculated using the B97-1 functional and B3LYP functional of Wang et. al. [184] which suggest a significant effect of dispersion on the calculated frequencies. Similar difference in frequencies calculated from the B97-D and B97-1 functional are seen in the ν_1 mode of H_2 in the $5^{12}(H_2)$, $5^{12}6^4(H_2)$, $5^{12}6^4$THF and $5^{12}6^4(H_2)$.THF cages. Further, differences in peak frequencies calculated using the B97-D and the B97-1 functionals are seen in various vibrational modes of water molecules present in the 5^{12}, $5^{12}(H_2)$, $5^{12}6^4(H_2)$, $5^{12}6^4$THF and $5^{12}6^4(H_2)$.THF cages. Further, the peak frequencies obtained from the B97-D functional shows excellent agreement with experimental data. Hence, the B97-D functional has been chosen for further analysis of various vibrational modes which occur in the cages of the hydrate lattice.

6.3.2.2 High frequency modes

The vibrational modes which appear between 2900 and 4400 cm^{-1} represents the high frequency modes. The vibrational mode of H_2 molecule which appears in the high frequency region is shown in Figure **6.1** and the peak frequency is shown in Table **6.1**. Strobel et al. [167] employed Raman spectroscopy and characterized vibron bands in pure and THF doped hydrogen clathrate hydrates. The authors observed that the vibrational frequencies of H_2 in the cages of the clathrate hydrates were red-shifted compared to the gas phase H_2 molecule. Similar to the observations of Strobel et. al. [167], we observe that the ν_1 mode of H_2 in the $5^{12}(H_2)$ cage show a 15 cm^{-1} red shift compared to the isolated H_2 molecule. Similarly, the ν_1 mode of H_2 in the $5^{12}6^4(H_2)$ and $5^{12}6^4(H_2)$.THF cages show a red-shift of 10 cm^{-1} and 6 cm^{-1} respectively, compared to isolated H_2 molecule. The observed red-shift can be attributed to the confinement of H_2 molecule in the nano-cavity of the water cages. The nano-confinement results in dispersive interactions between the

Table 6.1: Raman peak assignments (cm^{-1}) in 5^{12}, $5^{12}(H_2)$, $5^{12}6^4$, $5^{12}6^4(H_2)$ and $5^{12}6^4(H_2)$.THF cages (reference: isolated H_2). Frequencies are calculated using the B97-D and B97-1 functionals (in parenthesis).

Modes	H_2	5^{12}	$5^{12}(H_2)$	$5^{12}6^4$	$5^{12}6^4(H_2)$	$5^{12}6^4(H_2)$.THF	Expt
ν_1	4376	-	4361	-	4366	4370	-
	(4435)		(4399)		(4417)	(4427)	
	4436[a]						
ν_2	-	3637	3629	3604	3600	3584	3630[b,c]
	-	(3736)	(3734)	(3737)	(3731)	(3702)	
ν_3	-	3484	3482	3486	3476	3457	3450[b,c]
		(3686)	(3633)	(3623)	(3622)	(3615)	
ν_4	-	3324	3304	3297	3291	3231	3225[b,c]
	-	(3256)	(3253)	(3247)	(3249)	(3191)	
ν_5	-	1647	1638	1645	1642	1632	1645[b]
		(1668)	(1661)	(1664)	(1662)	(1653)	
ν_6	-	40-809	37-800	33-867	30-862	24-899	-
	-	(42-828)	(39-792)	(34-864)	(33-863)	(27-853)	

[a]Ref [184], [b]Ref [186] , [c]Ref [187]

encapsulated H_2 molecule and the water molecules of these cages. The ν_1 mode of H_2 in the $5^{12}6^4(H_2)$.THF cage shows a blue-shift of 4 cm^{-1} compared to the $5^{12}6^4(H_2)$ cage. This suggests that an inclusion of a THF molecule ($5^{12}6^4(H_2)$.THF cage) reduces the interaction of H_2 molecule with water molecules of the cages. The ν_1 mode of H_2 in the $5^{12}6^4(H_2)$ and $5^{12}6^4(H_2)$.THF cages appears at a higher frequency than the $5^{12}(H_2)$ cage which is consistent with the trends seen from the work of Strobel et. al. [167]

The asymmetric stretch (ν_2), symmetric stretch (ν_3) and bending overtone (ν_4) modes of water molecules in various cages is displayed in Figure **6.2**. The calculated peak frequencies from the ν_2, ν_3 and ν_4 modes resemble closely with the experimental Raman spectra of Walrafen et. al. [186] on liquid water and Schicks et. al. [187] on mixed

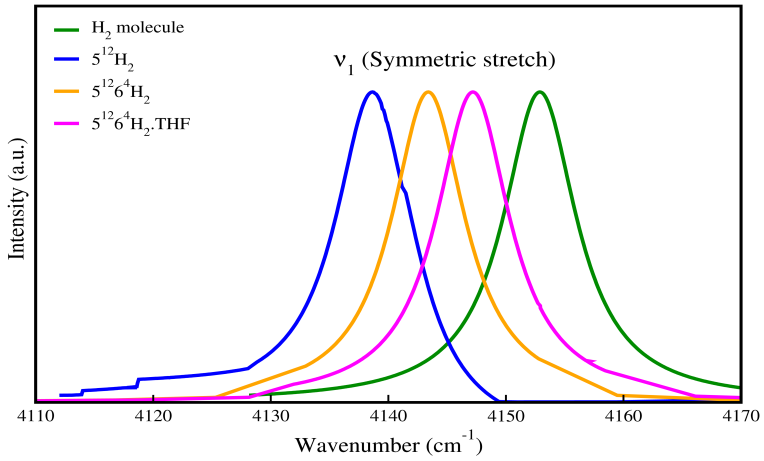

Figure 6.1: Symmetric stretch of pure and THF doped 5^{12} and $5^{12}6^4$ cages.

clathrate hydrates. The ν_2, ν_3 and ν_4 modes in the $5^{12}(H_2)$ cage show a red-shift compared to the 5^{12} cage. Similarly, red-shifts in vibrational modes are seen in the $5^{12}6^4(H_2)$ and $5^{12}6^4(H_2)$.THF cages compared to the $5^{12}6^4$ cage. The red-shifts are due to interactions between H_2 and THF molecules with water molecules of these cages. Compared to the $5^{12}6^4(H_2)$ cage, the ν_2 and ν_3 mode in the $5^{12}6^4(H_2)$.THF cages show a red-shift by 16 cm^{-1} and 19 cm^{-1} respectively, whereas the ν_4 mode shows a red-shift of 60 cm^{-1}. The influence of THF is seen by an examination of the CH_2 vibrational modes (Table **6.2**). The calculated vibrational modes in the $5^{12}6^4$.THF cage show excellent agreement with the experimental Raman spectra of Tulk et. al. [188] The THF modes in the $5^{12}6^4(H_2)$.THF cage shows that the CH_2 asymmetric (2957 cm^{-1}) and symmetric (2933 cm^{-1}) stretching modes shows a red-shift compared to the CH_2 modes in the $5^{12}6^4$.THF cage. The red-shifts can be attributed to the interactions of H_2 with the water molecules of the cages, and H_2 molecule with THF molecules. Further, the red-shift from the CH_2 asymmetric stretch is larger compared to the corresponding CH_2 symmetric stretch.

6.3.2.3 Mid and low frequency modes

The mid-frequency (1000 - 2000 cm^{-1}) and low frequency (<1000 cm^{-1}) modes is shown in Figure **6.3**. The modes of vibration observed in the mid frequency region is the bending (ν_5) mode of water molecules. The peak frequency of the ν_5 mode is in agreement

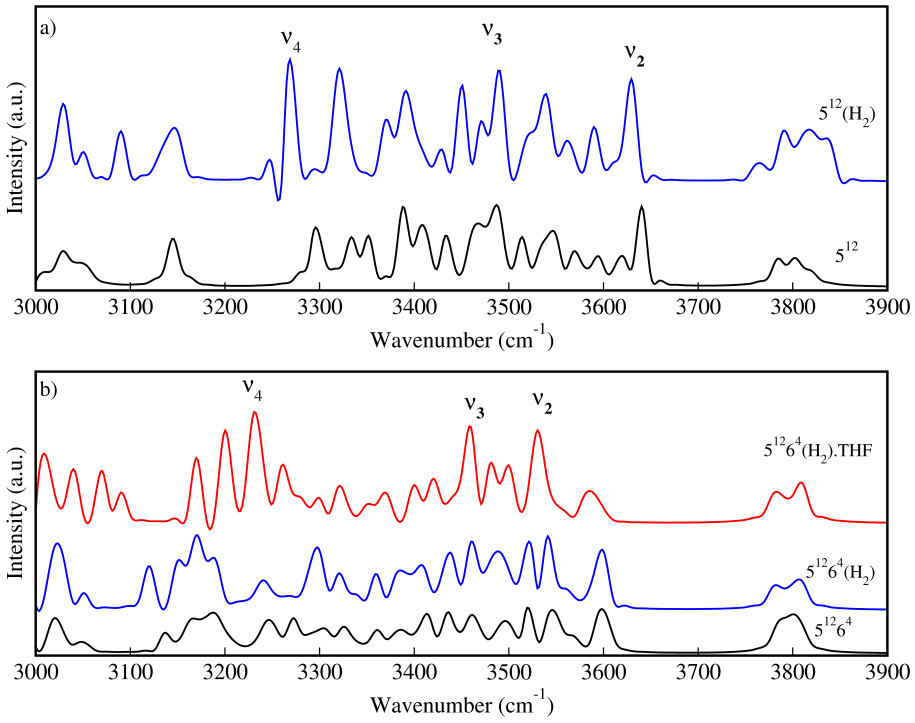

Figure 6.2: The symmetric and asymmetric stretch vibrations in a) 5^{12} and $5^{12}(H_2)$ cages, b) $5^{12}6^4$, $5^{12}6^4(H_2)$ and $5^{12}6^4(H_2)$.THF cages.

with the work of Walrafen et. al. [186] The ν_5 mode in the $5^{12}(H_2)$ cage shows a 9 cm^{-1} red-shift compared to the 5^{12} cage. The ν_5 mode in the $5^{12}6^4(H_2)$ cage show a 3 cm^{-1} red-shift compared to the $5^{12}6^4$ cage. The $5^{12}6^4(H_2)$.THF cage shows a 10 cm^{-1} red shift compared to the $5^{12}6^4(H_2)$ cage. It is observed that the red-shifts in the ν_4 mode is much larger compared to the corresponding ν_5 mode which suggests that the bending overtone modes changes significantly compared to the bending modes.

The low frequency vibrational modes also known as librational modes in all cages (Table **6.1**) show the following features: The lowest librational mode represents a contraction and expansion of the cages which is characterized by a collective and synchronized motion of water molecules. The librational mode from 250 - 400 cm^{-1} represents the dangling motion of the water molecules of the cages. This arises due to the O-O stretching vibrations and is consistent with the experimental observations of Walrafen et. al. [186] The librational modes from 400 – 700 cm^{-1} corresponds to hydrogen bonding interactions in water molecules. The low frequency vibrational modes of the encapsulated THF

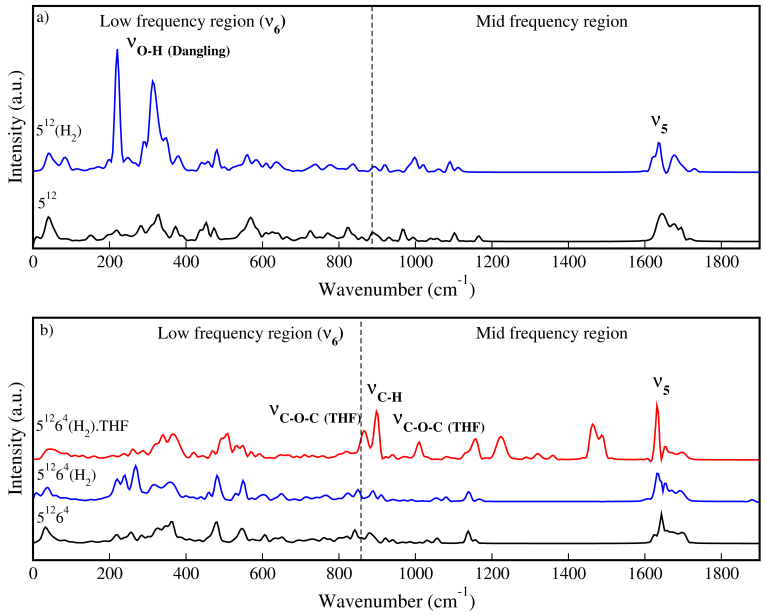

Figure 6.3: Mid-frequency and low frequency Raman spectra in a) 5^{12} and $5^{12}(H_2)$ cages, b) $5^{12}6^4$, $5^{12}6^4(H_2)$ and $5^{12}6^4(H_2)$.THF cages.

in the $5^{12}6^4(H_2)$.THF cage appear between 880 cm^{-1} and 1020 cm^{-1} (Table **6.2**). The symmetric C-O-C stretching in the $5^{12}6^4(H_2)$.THF cage appear at ~ 886 cm^{-1} and shows a 6 cm^{-1} red shift compared to the $5^{12}6^4$.THF cage. The C-H ring breathing mode in the $5^{12}6^4(H_2)$.THF cage appears at ~ 900 cm^{-1} and shows a 10 cm^{-1} red-shift compared to the $5^{12}6^4$.THF cage. Similarly, the C-O-C asymmetric stretch in the $5^{12}6^4(H_2)$.THF cage appears at ~ 1019 cm^{-1} and shows a 6 cm^{-1} red-shift compared to the $5^{12}6^4$.THF cage. The red-shifts of various vibrational modes of the THF molecule in the $5^{12}6^4(H_2)$.THF cage (compared to the $5^{12}6^4$.THF cage) are due to the interaction of the H_2 molecule with THF and water molecules of the cages.

6.3.3 Spectral properties on multiple occupancy

In order to present an accurate characterization of spectral properties, five configurations which differ in proton orientations are chosen. The details of these configuration for each occupancy of H_2 pure and THF doped 5^{12} and $5^{12}6^4$ cages are described in Chapter 5 (Section 5.2). The Raman peak frequency corresponding to each configuration of $5^{12}(H_2)_{n=0-2}$, $5^{12}6^4(H_2)_{n=0-4}$ and $5^{12}6^4(H_2)_{n=1,2}$.THF cages are shown in Table **B6-1(a-j)**. In the next sub

Table 6.2: Raman peak assignments (cm^{-1}) in $5^{12}6^4$.THF and $5^{12}6^4(H_2)$.THF cages.

Modes	$5^{12}6^4$.THF	$5^{12}6^4$.THF (Experiment)	$5^{12}6^4(H_2)$.THF
C-O-C symmetric stretch	892	891[c]	886
C-H ring breathing mode	910	913c	900
C-O-C asymmetric stretch	1025	1034[d]	1019
CH_2 symmetric stretch	2935	2935[c]	2933
CH_2 asymmetric stretch	2994	2989[c]	2957

[c]Ref [188], [d]Ref [103]

sections, the bond lengths and spectral properties are calculated as an average using five configurations of each cage.

6.3.3.1 H-H symmetric stretch

The average H-H bond lengths of H_2 molecules in the pure and THF doped 5^{12} and $5^{12}6^4$ cages (see Figure **6.4**) shows the following trends. The H-H bond length in the $5^{12}(H_2)$ cage is 0.7451 Å compared to 0.7448 Å of free H_2 molecule. However, the average H-H bond length in the $5^{12}(H_2)_2$ cage is 0.7419 Å. The average H-H bond length varies from 0.7449 Å to 0.7434 Å in the $5^{12}6^4(H_2)_{n=1-4}$ cages. Similar trends in H-H bond length are also observed for the THF doped $5^{12}6^4$ cages. The trends observed in the bond length with encapsulation of H_2 are correlated with the shifts of vibrational spectra. The statistically averaged Raman spectra is shown in Figure **6.5** and **6.6** with the corresponding average peak frequency in Table **6.3**.

The ν_1 mode in the $5^{12}(H_2)_2$ cage show a blue-shift of 33 cm^{-1}, relative to the $5^{12}(H_2)$ cage. These blue-shifts are due to the encapsulation of two H_2 molecules in the $5^{12}(H_2)_2$ cage which leads to an expansion of the cage radii to 4 Å, compared to the $5^{12}(H_2)$ cage radii of 3.78 Å. However, the ν_1 mode in the $5^{12}6^4(H_2)_2$ cages show a blue-shift of 8 cm^{-1}, respectively, relative to the $5^{12}6^4(H_2)$ cage. Similarly, the ν_1 mode in the $5^{12}6^4(H_2)_{n=3,4}$

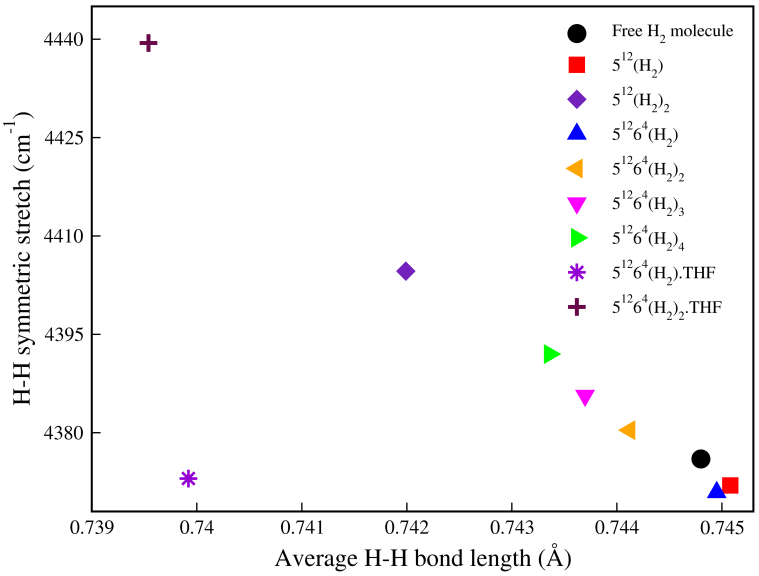

Figure 6.4: Hydrogen bond length vs. Raman vibrational H-H symmetric stretching frequency.

cages also show a blue-shift of 6 cm^{-1} and 6 cm^{-1}, relative to the $5^{12}6^4(H_2)_{n=2,3}$ cages. The blue-shifts seen with increasing H_2 occupancy may be due to repulsive interactions between multiple H_2 molecules leading to an expansion of $5^{12}6^4$ cage. The ν_1 mode in the $5^{12}6^4(H_2)_2$.THF cage shows a blue-shift of 65 cm^{-1}, relative to the $5^{12}6^4(H_2)$.THF cage.

The observed blue-shift in the $5^{12}6^4(H_2)_2$.THF cage is larger than the observed blue-shifts seen from the $5^{12}(H_2)_2$ and $5^{12}6^4(H_2)_{n=2-4}$ cages. The blue-shifts in the $5^{12}6^4(H_2)_2$.THF cage is due to the enhanced repulsive interactions of two H_2 molecules with the THF molecule, thereby causing an increase in the cage radii. To compare with experimental observations, our calculated quantum mechanical harmonic vibrational frequencies for H-H stretching mode are corrected by a scaling factor proposed by Wong et. al. [189] and Merrick et. al. [190] The scaling factor is calculated as a ratio between the observed frequencies of H_2 gas (4155 cm^{-1}) [184] and the calculated harmonic H-H stretch of an isolated H_2 molecule (4376 cm^{-1}).

6.3.3.2 Water vibrational modes

The ν_2, ν_3 and ν_4 water modes in the $5^{12}(H_2)_2$ cage shows a blue-shift of 15 cm^{-1}, 26 cm^{-1} and 33 cm^{-1} respectively, relative to the $5^{12}(H_2)$ cage. The ν_2, ν_3 and ν_4 water modes in the

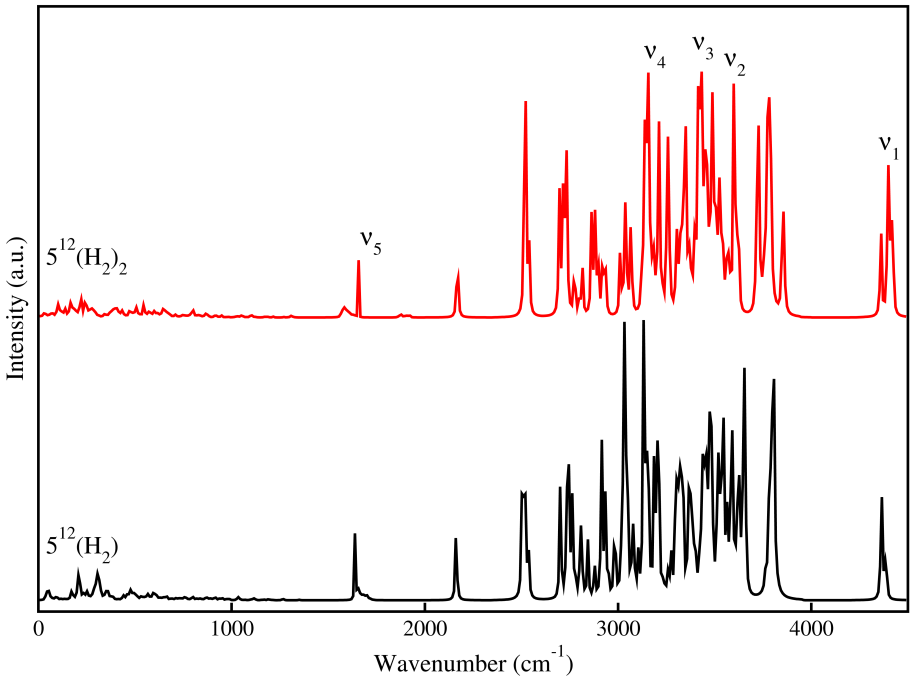

Figure 6.5: Statistically averaged Raman spectra of $5^{12}(H_2)_{n=0-2}$ cages.

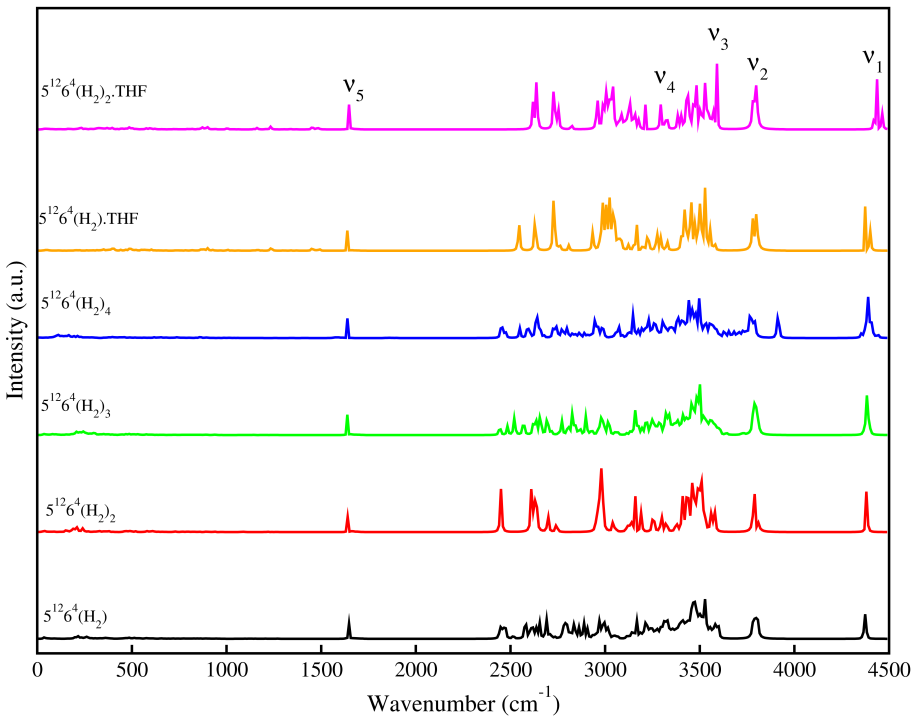

Figure 6.6: Statistically averaged Raman spectra of $5^{12}6^4(H_2)_{n=0-4}$ and $5^{12}6^4(H_2)_{n=1,2}$.THF cages.

Table 6.3: Statistically averaged Raman peak assignments (cm^{-1}) in $5^{12}(H_2)_{n=0-2}$, $5^{12}6^4(H_2)_{n=0-4}$ and $5^{12}6^4(H_2)_{n=1,2}$.THF cages. (Values in parenthesis represent the scaled frequencies only for the H-H symmetric stretch).

Structure	ν_1	ν_2	ν_3	ν_4	ν_5
H_2	4376	-	-	-	-
5^{12}	-	3580	3493	3201	1646
$5^{12}(H_2)$	4372	3576	3461	3175	1640
	(4149)				
$5^{12}(H_2)$	4405	3591	3487	3208	1650
	(4180)				
$5^{12}6^4$	-	3578	3483	3195	1643
$5^{12}6^4(H_2)$	4372	3523	3474	3166	1642
	(4149)				
$5^{12}6^4(H_2)_2$	4380	3513	3464	3161	1639
	(4157)				
$5^{12}6^4(H_2)_3$	4386	3502	3454	3160	1638
	(4162)				
$5^{12}6^4(H_2)_4$	4392	3499	3445	3142	1635
	(4168)				
$5^{12}6^4(H_2)$.THF	4374	3533	3458	3169	1637
	(4151)				
$5^{12}6^4(H_2)_2$.THF	4439	3588	3507	3209	1653
	(4213)				
Experiment	-	3630[a]	3450[b]	3225[b]	1645[c]

[a]Ref [178], [b]Ref [187],[c] Ref [103]

ν_1: H-H symmetric stretch, ν_2: O-H asymm stretch, ν_3: O-H symm stretch, ν_4: bending mode overtone, ν_5: bending mode. Only H-H symmetric stretch frequencies are scaled by a factor of 0.949 (the ratio between 4155 cm^{-1} of H_2 gas [184] and 4376 cm^{-1} of the H-H symmetric stretch of free isolated single H_2.

$5^{12}6^4(H_2)_{n=2-4}$ cages show a red-shift relative to the $5^{12}6^4(H_2)_{n=1-3}$ cages. These red-shifts are due to increase in attractive interaction between the hydrogen and water molecules of the cages. Compared to the $5^{12}6^4(H_2)_3$ cage, there are additional peaks seen between 3500-3900 cm^{-1} in the $5^{12}6^4(H_2)_4$ cage. These additional peaks are O-H stretching vibrations which span a broad range of frequencies due to the enhanced dispersive interactions between multiple H_2 molecules and water molecules of the cage. The ν_2, ν_3 and ν_4 modes in the $5^{12}6^4(H_2)_2$.THF cage shows a blue-shift of 55 cm^{-1}, 49 cm^{-1} and 40 cm^{-1} respectively, relative to the $5^{12}6^4(H_2)$.THF cage. This is due to repulsive interaction between the hydrogen molecules, which reduces the interaction with the water molecules of the cages. The observed red-shifts and blue-shifts are consistent with the loose-cage tight-cage water model proposed by Buckingham et. al. [191] and Subramanian et. al. [192]

The bending (ν_5) mode of water molecules shows trends similar to ν_2, ν_3 and ν_4 water modes in the $5^{12}(H_2)_{n=1,2}$, $5^{12}6^4(H_2)_{n=1-4}$ and $5^{12}6^4(H_2)_{n=1,2}$.THF cages. Further, compared to other vibrational modes, the shifts seen from the ν_5 mode of water molecules are significantly small. Since, experimental data on vibrational modes of water molecules in pure and THF doped hydrogen clathrate hydrates are not available, a comparison of calculated vibrational modes of water molecules agree with Raman spectroscopy measurements performed on similar clathrate hydrates [187]. In order to characterize the influence of configurations on spectral properties, we have calculated the spectral peak frequencies using ten configurations of 5^{12} and $5^{12}(H_2)$ cages. Our calculations show that the average spectral peak frequency and standard deviation does not result any significant change with inclusion of more configurations. A comparison of standard deviations of average frequency from various vibrational modes from all cages shows no particular trend. However, the magnitude of standard deviation arises from various configurations which differ in proton arrangement of water cages.

6.3.4 Deformation Energies

To gain insights into the structural changes which occur with the encapsulation of multiple occupancies of H_2 in pure and THF doped 5^{12} and $5^{12}6^4$ cages; the deformation energies

(see Eqn. 6.1) are shown in Table 6.4. Further examination of the deformation energy shows that the encapsulation of single H_2 molecule in the 5^{12} cage does not distort the cage significantly. The deformation energy for the $5^{12}(H_2)$ cage is in good agreement with the results reported by Kumar et. al. [43, 45]. However, the encapsulation of second H_2 in the $5^{12}(H_2)$ shows a large deformation energy of 6.17 kcal/mol. The large deformation energy is because the double occupancy of H_2 in the 5^{12} cage is not preferred (as seen from the positive value of our calculated interaction energy). The deformation energy vary from 0.05 kcal/mol for the $5^{12}6^4(H_2)$ cage to 0.27 kcal/mol for the $5^{12}6^4(H_2)_4$ cage. This suggests that the structural integrity of the $5^{12}6^4$ cage remains intact till the quadruple occupancy of H_2 molecule. The small deformation energy of 0.88 kcal/mol suggests that a single occupancy of H_2 with THF does not distort the $5^{12}6^4(H_2)$ cage. However, relatively large deformation energy of 3.62 kcal/mol shows a double occupancy of H_2 with a THF molecule in the $5^{12}6^4(H_2)$ cage is less preferred.

Table 6.4: Deformation energies (kcal/mol) of pure and THF doped 5^{12} and $5^{12}6^4$ cages of hydrogen clathrate hydrates.

Cage	Deformation Energy
$5^{12}(H_2)$	0.06, 0.03[a], 0.07[b]
$5^{12}(H_2)_2$	6.17
$5^{12}6^4(H_2)$	0.05
$5^{12}6^4(H_2)_2$	0.14
$5^{12}6^4(H_2)_3$	0.17
$5^{12}6^4(H_2)_4$	0.27
$5^{12}6^4(H_2)$.THF	0.88
$5^{12}6^4(H_2)_2$.THF	3.62

[a]Ref [43], [b]Ref [45]

6.4 Conclusions

The symmetric stretch of H_2 in the $5^{12}(H_2)_2$, $5^{12}6^4(H_2)_{2-4}$ and $5^{12}6^4(H_2)_2$.THF cages show a blue-shift, compared to the $5^{12}(H_2)$, $5^{12}6^4(H_2)_{1-3}$ and $5^{12}6^4(H_2)$.THF cages, respectively. The vibrational modes of water molecules in the $5^{12}(H_2)_2$ and $5^{12}6^4(H_2)_2$.THF cages are blue-shifted, compared to the $5^{12}(H_2)$ and $5^{12}6^4(H_2)$.THF cage, respectively. An examination of all water vibrational modes show that the $5^{12}(H_2)$, $5^{12}6^4(H_2)_4$ and $5^{12}6^4(H_2)$.THF cages are red-shifted compared to $5^{12}(H_2)_2$, $5^{12}6^4(H_2)_{1-3}$ and $5^{12}6^4(H_2)_2$.THF cages, respectively. These spectral shifts suggest that the $5^{12}(H_2)$, $5^{12}6^4(H_2)_4$ and $5^{12}6^4(H_2)$.THF cages to be most stable and is consistent with Raman spectroscopy [24, 167, 184, 193] on multiple occupancy of hydrogen in pure and THF doped polyhedral water cages. In the next chapter, the interaction and vibrational Raman spectra of multiple occupancy of nitrogen clathrate hydrates is discussed.

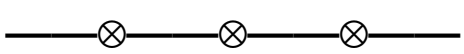

Chapter 7

Interaction energy and vibrational Raman spectra of nitrogen clathrate hydrates

7.1 Introduction

Nitrogen clathrate hydrates [7] are cage compounds where nitrogen gas molecules are encapsulated in various polyhedral water cages of a sII hydrate lattice. These hydrates exist in abundance in the solar system and in interstellar space [194, 195]. Recently, an inclusion of hydrogen molecules in the cages of nitrogen clathrate hydrates was explored as potential candidates for hydrogen storage at moderate pressure [196]. Experimental and computational methods have been employed to determine the cage occupancy and thermodynamic stability of these clathrate hydrates. For example, Dyadin et. al. [197] synthesized N_2 clathrate hydrates and found that extremely high pressures (1500 MPa) were required for the formation of these clathrate hydrates. Similarly, Sugahara et. al. [198] observed the spontaneous formation of N_2 clathrate hydrates at high pressure (440 MPa). Sasaki et. al. [199] employed Raman spectroscopy to determine the phase transformation of N_2 clathrate hydrates and observed a spontaneous formation at high pressure (6000 MPa) at T=296 K. The Raman spectroscopy measurements of Champagnon et. al. [200],

neutron diffraction studies of Chazollon et. al. [201] and MD simulations of Horikawa et. al. [202], and van Klaveren et. al. [203, 204] revealed the $5^{12}(N_2)$ and $5^{12}6^4(N_2)_2$ cages to be the most stable. Hinsberg et. al. [205] employed high pressure Raman spectroscopy and observed that the encapsulation of N_2 in the cages of clathrate hydrates leads to a shift of vibrational modes to lower wave-numbers compared to free nitrogen molecule.

In the present chapter, characterization of interaction energy and vibrational Raman spectra associated with an encapsulation of N_2 in the 5^{12} and $5^{12}6^4$ cages is presented. The computational details are shown in Section 7.2. The interaction energies and vibrational Raman spectra is described in Section 7.3. A summary of salient results concludes this chapter.

7.2 Computational details

Calculations were performed using the 6-311++G(d,p) basis set and B97-D functional. The input configurations of the $5^{12}(N_2)_{n=1,2}$ cages was obtained by an encapsulation of a single N_2 molecule in the optimized $5^{12}(N_2)_{n=0,1}$ cages respectively. Similarly, the input configuration of the $5^{12}6^4(N_2)_{n=1-3}$ cages was obtained by an encapsulation of a single N_2 molecule in the optimized $5^{12}6^4(N_2)_{n=0-2}$ cages respectively. Geometry optimization on each cage was performed and the optimized configurations of multiple occupancy of N_2 in 5^{12} and $5^{12}6^4$ cages are shown in Figure **7.1** respectively. The total energy was calculated at the optimized geometry and corrected for BSSE [132, 133] and ZPVE. The interaction energy is calculated as:

$$IE = E[cage.(N_2)_n] - E[cage] - nE[N_2] \tag{7.1}$$

where, n is the number of nitrogen molecules, $E[N_2]$ is the total energy of an isolated nitrogen molecule. $E[cage.(N_2)_n]$ is the total energy of 5^{12} or $5^{12}6^4$ cage containing the encapsulated nitrogen molecules(s). E[cage] is the total energy of the 5^{12} or $5^{12}6^4$ cage. To examine the structural integrity of the cages, we have calculated the deformation energy [see Eqn. **6.4**] of the water cage associated with encapsulation of N_2 in the 5^{12} or $5^{12}6^4$

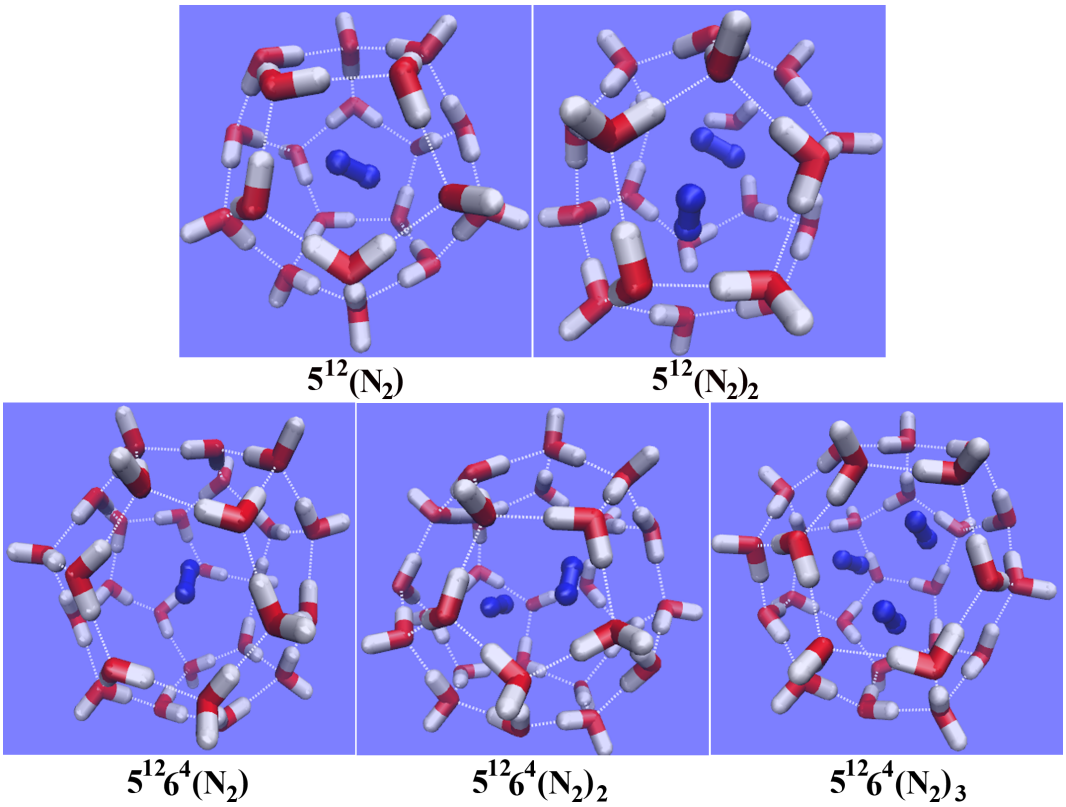

Figure 7.1: Structure of $5^{12}(N_2)_{n=1,2}$ and $5^{12}6^4(N_2)_{n=1-3}$ cages.

cages.

7.3 Results and discussion

7.3.1 Interaction Energy

The interaction energies, ZPVE contributions and deformation energy are shown in Table 7.1. The increasing negative value of interaction energy illustrates more stability, and a positive value of interaction energy suggests unstability. The interaction energy shows that the $5^{12}(N_2)$ cage (-3.27 kcal/mol) is more stable compared to the $5^{12}(N_2)_2$ cage (7.59 kcal/mol). The interaction energy in the $5^{12}(N_2)$ cage (in our study) show more stability compared to the interaction energy (-2.59 kcal/mol) reported by Kumar et. al. [43] This difference is due to the choice of method between these calculations. The interaction energy in the $5^{12}6^4(N_2)$ and $5^{12}6^4(N_2)_2$ cages are -3.00 kcal/mol and -3.76 kcal/mol,

Table 7.1: Interaction energy (kcal/mol) and Deformation energy (kcal/mol). Contributions from ZPVE to interaction energy is shown in parenthesis.

Cage	Cage radii (Å)	Interaction energy	Deformation energy
$5^{12}(N_2)$	3.9	-3.27 (0.49)	0.4
$5^{12}(N_2)_2$	4.2	7.59 (10.24)	4.9
$5^{12}6^4(N_2)$	4.6	-3.00 (0.52)	0.5
$5^{12}6^4(N_2)_2$	4.6	-3.76 (0.54)	0.7
$5^{12}6^4(N_2)_3$	4.7	-0.43 (5.40)	1.6

respectively, which illustrates that both cages are stable. The interaction energy in the $5^{12}6^4(N_2)_3$ cage is -0.43 kcal/mol which show less stability compared to the $5^{12}6^4(N_2)_{n=1,2}$ cages. Further, attempts to obtain triple and quadruple occupancy of N_2 in 5^{12} and $5^{12}6^4$ cages respectively, leads to a disintegration of the water cages. The maximum stability of the $5^{12}(N_2)$ and $5^{12}6^4(N_2)_2$ cages seen from the interaction energies validate the experimental observations of Champagnon et. al. [200] and Chazallon et. al. [201] and MD simulations of Horikawa et. al. [202] and van Klaveren et. al. [204]

The large ZPVE contributions to the interaction energy in the $5^{12}(N_2)_2$ and $5^{12}6^4(N_2)_3$ cages leads to meta-stability or less stability of these cages. The large ZPVEs with increasing occupancy is also consistent with the observations of Bacic and co-workers [180]. An examination of the deformation energy shows the following trends: The deformation energy in the $5^{12}(N_2)$ and $5^{12}(N_2)_2$ cages are 0.4 and 4.9 kcal/mol respectively. Similarly, the deformation energy in the $5^{12}6^4(N_2)$, $5^{12}6^4(N_2)_2$ and $5^{12}6^4(N_2)_3$ cages are 0.5, 0.7 and 1.6 kcal/mol, respectively. A comparison of deformation energy show that the $5^{12}(N_2)$ and $5^{12}6^4(N_2)_{n=1,2}$ cages are stable compared to the $5^{12}(N_2)_2$ and $5^{12}6^4(N_2)_3$ cages, respectively.

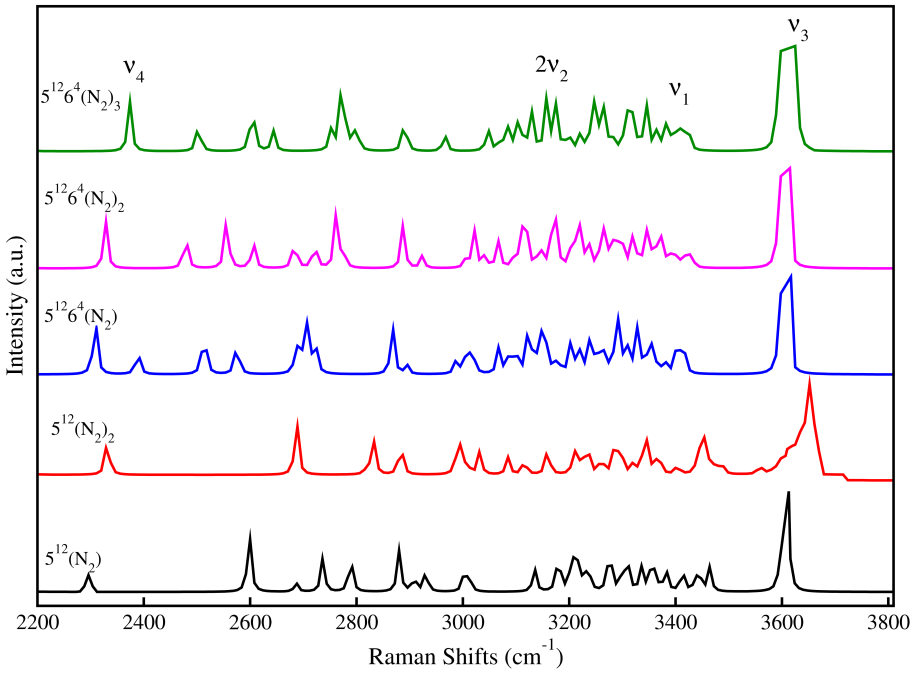

Figure 7.2: N-N symmetric stretch, asymmetric stretch, symmetric stretch and bending overtone modes of water molecules in $5^{12}(N_2)_{n=1,2}$ and $5^{12}6^4(N_2)_{n=1-3}$ cages.

7.3.2 Vibrational Raman Spectra

The effect of encapsulation of N_2 in 5^{12} and $5^{12}6^4$ cages can be seen by an examination of shift of vibrational modes. The vibrational Raman spectra are shown in Figure 7.2 with the corresponding peak frequency in Table 7.2. An examination of the N-N symmetric stretch (ν_4) mode in the $5^{12}(N_2)_{n=1,2}$ and $5^{12}6^4(N_2)_{n=1-3}$ cages show the following trends. The ν_4 mode in the $5^{12}(N_2)$ and $5^{12}6^4(N_2)$ cages show a red-shift, relative to the ν_4 mode of free N_2 molecule. The red-shift is due to the confinement of single N_2 molecule in the water cages. The spectral trends observed are in agreement with the results of Champagnon et. al. [200] and Hinsberg et. al. [205] The ν_4 mode in the $5^{12}(N_2)_2$ cage show a blue-shift of 7 cm^{-1}, relative to the $5^{12}(N_2)$ cage. Further, the ν_4 mode in the $5^{12}6^4(N_2)_2$ and $5^{12}6^4(N_2)_3$ cages also shows a blue-shift of 4 cm^{-1} and 1 cm^{-1}, relative to the $5^{12}6^4(N_2)$ and $5^{12}6^4(N_2)_2$ cages, respectively. The blue-shift occurs due to the repulsion between multiple N_2 molecules leading to an expansion of the water cage, thereby reducing the interactions with the water cages.

Table 7.2: Raman peak assignments (cm^{-1}) in $5^{12}(N_2)_{n=0-2}$ and $5^{12}6^4(N_2)_{n=0-3}$ cages.

Modes	**N_2**	**5^{12}**	**$5^{12}(N_2)$**	**$5^{12}(N_2)_2$**	**$5^{12}6^4$**	**$5^{12}6^4(N_2)$**	**$5^{12}6^4(N_2)_2$**	**$5^{12}6^4(N_2)_3$**
ν_4	2365	-	2364	2371	-	2363	2367	2368
			2335[a]			2331[a]		
			2324[b]			2327[b]		
ν_3	-	3647	3613	3655	3621	3617	3615	3625
ν_1	-	3488	3479	3487	3494	3490	3489	3514
$2\nu_2$	-	3375	3080	3192	3332	3094	3088	3247
ν_2	-	1643	1632	1648	1639	1636	1635	1641

[a]Ref [200],[b]Ref [205]

An examination of vibrational modes of water molecules shows the following trends: The asymmetric stretch (ν_3), symmetric stretch (ν_1), bending overtone ($2\nu_2$) and bending (ν_2) modes in the $5^{12}(N_2)$ cages shows a red-shift, relative to the 5^{12} cage. All the water modes of vibration (ν_1, ν_2, ν_3 and $2\nu_2$) in the $5^{12}(N_2)_2$ cage shows a blue-shift compared to the $5^{12}(N_2)$ cage. The blue-shifts arise due to repulsive interactions which exist between the two nitrogen molecules in the $5^{12}(N_2)_2$ cage leading to the expansion of the cage radius to 4.2 Å, compared to the 3.9 Å radius of the $5^{12}(N_2)$ cage. The ν_1, ν_2, ν_3 and $2\nu_2$ modes in the $5^{12}6^4(N_2)_{n=1,2}$ cages show a red-shift compared to the $5^{12}6^4(N_2)_{n=0,1}$ cages respectively. The water modes of vibration (ν_1, ν_2, ν_3 and $2\nu_2$) in the $5^{12}6^4(N_2)_3$ cage show a blue-shift compared to the $5^{12}6^4(N_2)_2$ cage. The blue-shift leads to the expansion of the cage radius to 4.7 Å due to repulsive interactions between three nitrogen molecules. The spectral trends show the $5^{12}6^4(N_2)_2$ cage to be most stable, relative to the $5^{12}6^4(N_2)$ and $5^{12}6^4(N_2)_3$ cages and is consistent with conclusions derived from interaction energy. Finally, we have examined the effect of input configuration on the spectral properties by choosing five input configurations which differ in proton orientations of multiple occupancy of N_2 in 5^{12} and $5^{12}6^4$ cages. Our calculations showed that the spectral trends were similar, where a difference in frequency obtained by choosing various input configurations was <10 cm^{-1}.

7.4 Conclusions

The interaction energy shows the $5^{12}(N_2)$ and $5^{12}6^4(N_2)_2$ cages to be the most stable compared to other occupancies. All vibrational modes of water molecules in the $5^{12}(N_2)$, and $5^{12}6^4(N_2)_2$ cages show a red-shift, relative to the $5^{12}(N_2)_2$, $5^{12}6^4(N_2)_{n=1,3}$ cages respectively. The deformation energy shows that the most stable occupancy of N_2 in the 5^{12} and $5^{12}6^4$ cages do not distort the cages significantly. The interaction energy and spectral properties presented in this study can guide experimental efforts in understanding the formation of multiple occupancy of nitrogen in the cages of clathrate hydrates. In the next chapter, the interaction energy vibrational raman spectra associated with the multiple occupancy of cages of oxygen clathrate hydrates is discussed.

Chapter 8

Interaction energy and vibrational Raman spectra of oxygen clathrate hydrates

8.1 Introduction

Oxygen clathrate hydrates are crystalline solids found in magnetized water and inhibit corrosion in pipes and boilers [206, 207]. These hydrates also exist in abundance in the solar system and in interstellar space [208]. Structurally, these hydrates are composed of oxygen molecules encapsulated in the 5^{12} and $5^{12}6^4$ cages of a sII hydrate lattice [209]. The stability of hydrates is determined by the number of oxygen molecules which stabilize the framework of water cages. Several experimental investigations have been performed on the thermodynamic stability of oxygen clathrate hydrates [210–216]. Hallbrucker et. al. [217] employed Raman spectroscopy to monitor the formation of oxygen clathrate hydrates and observed the presence of O_2 molecules only in $5^{12}6^4$ cages. Raman spectroscopy measurements of Champagnon et. al. [200] and MD simulations of Horikawa et. al. [202] suggested a single occupancy of O_2 in the 5^{12} cage and a doubly occupancy of O_2 in the $5^{12}6^4$ cage. Chazallon et. al. [201] employed neutron diffraction techniques and observed a double occupancy of O_2 in the $5^{12}6^4$ cage. Ikeda et. al. [218] recorded the

Raman spectra of oxygen clathrate hydrates and observed that that the peak intensities of O_2 stretching vibrational modes shift due to the distortion of the 5^{12} cages.

The stability and spectra of varying occupancies of O_2 molecules in the 5^{12} and $5^{12}6^4$ cages is the objective of the present study. The computational details are described in Section 8.2. The interaction energy and Raman spectra are presented in Section 8.3. A summary of salient results concludes this chapter.

8.2 Computational details

All calculations were performed using the B97-D [66] functional and the 6-311++G** basis set. The $5^{12}(O_2)$ cage was optimized by an inclusion of an O_2 molecule in the center of the optimized 5^{12} cage and re-optimized. The input geometry of the $5^{12}(O_2)_2$ cage was obtained by an inclusion of a single O_2 molecule in the optimized $5^{12}(O_2)$ cage and further optimized. The input configuration of the $5^{12}6^4(O_2)$ cage was created by an inclusion of a single O_2 molecule in the optimized $5^{12}6^4$ cage and re-optimized. The input geometry of the $5^{12}6^4(O_2)_2$ and $5^{12}6^4(O_2)_3$ cages were obtained by an inclusion of a single O_2 molecule in the optimized $5^{12}6^4(O_2)$ and $5^{12}6^4(O_2)_2$ cages respectively. The optimized configuration of varying occupancies of O_2 in the 5^{12} and $5^{12}6^4$ cages is shown in Figure **8.1** and **8.2**. The calculated total energies (at the optimized geometry) is further corrected to include BSSE. The interaction energy associated with the encapsulation of oxygen molecules in various cages is calculated as:

$$IE = E[cage.(O_2)_n] - E[cage] - nE[O_2] \tag{8.1}$$

where, n is the number of oxygen molecules, $E[O_2]$ is the total energy of an isolated oxygen molecule. $E[cage.(O_2)_n]$ is the total energy of 5^{12} or $5^{12}6^4$ cage containing the encapsulated oxygen molecules(s). E[cage] is the total energy of 5^{12} or $5^{12}6^4$ cage.

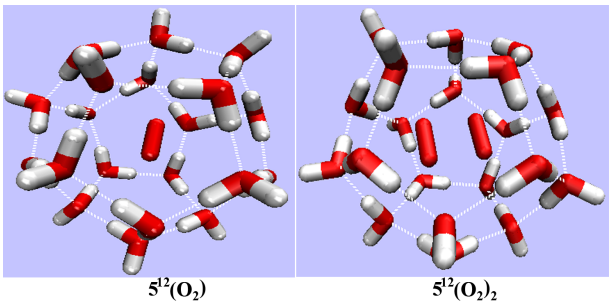

Figure 8.1: Optimized structures of $5^{12}(O_2)$, and $5^{12}(O_2)_2$ cages.

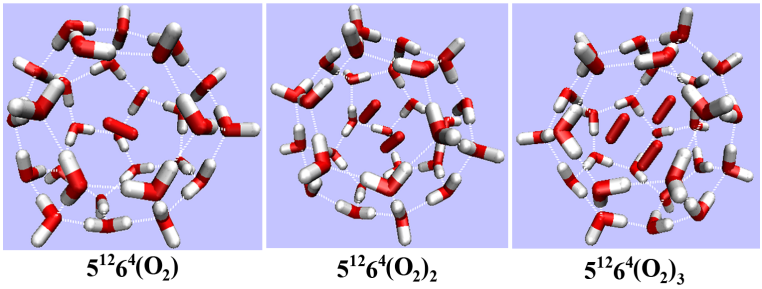

Figure 8.2: Optimized structures of $5^{12}6^4(O_2)$, $5^{12}6^4(O_2)_2$ and $5^{12}6^4(O_2)_3$ cages.

8.3 Results and discussion

8.3.1 Interaction Energy

The interaction energy associated with various occupancies of O_2 in the 5^{12} and $5^{12}6^4$ cages is shown in Table **8.1**. For example, the interaction energy calculations for the $5^{12}(O_2)$ cage is -7.70 kcal/mol which was found to be only possible occupancy of oxygen clathrate hydrates. However, the interaction energy calculations for the $5^{12}(O_2)_2$ cage shows instability (6.76 kcal/mol). Further increase in occupancy of O_2 molecules leads to the deformation of the 5^{12} cage. Kumar et. al. [43] employed second order MP2 method and 6-31G** basis set to perform a geometry optimization of the $5^{12}(O_2)$ cage. At the optimized geometry, the authors performed a single point energy calculations using the 6-311++G** basis set and reported an interaction energy of -7.88 kcal/mol for the $5^{12}(O_2)$ cage. The interaction energy calculations from our work in the $5^{12}(O_2)$ cage is in agreement with Kumar et. al. [43] In the $5^{12}6^4$ cage, the interaction energy from our work

is -3.72 kcal/mol ($5^{12}6^4(O_2)$) which shows stability with increasing occupancy, with the $5^{12}6^4(O_2)_2$ (-8.42 kcal/mol) to be the most stable. However, the interaction energies for the $5^{12}6^4(O_2)_3$ in the $5^{12}6^4$ cage shows lower stability (0.42 kcal/mol) compared to $5^{12}6^4(O_2)$ and $5^{12}6^4(O_2)_2$ cages. Similar to the 5^{12} cage, we increased the occupancy of O_2 inside the $5^{12}6^4$ cage which lead to the deformation of the $5^{12}6^4$ cages. The stability of oxygen occupancy in the 5^{12} and $5^{12}6^4$ cages are qualitatively consistent with the experimental observations and MD simulations.

Table 8.1: Interaction energies (IE) (kcal/mol) of varying occupancies of O_2 molecules in 5^{12} and $5^{12}6^4$ cages.

Cage	Cavity radii (Å)	IE
$5^{12}(O_2)$	4.00	-7.70
$5^{12}(O_2)_2$	4.20	6.76
$5^{12}6^4(O_2)$	4.50	-3.72
$5^{12}6^4(O_2)_2$	4.60	-8.42
$5^{12}6^4(O_2)_3$	4.70	0.42

8.3.2 Vibrational Raman spectra

The peak frequencies of O-O stretch (ν_1) in various oxygen encapsulated 5^{12} and $5^{12}6^4$ cages is shown in Table **8.2**. We observe that the ν_1 mode appears at 1532 cm^{-1} in isolated O_2, 1509 cm^{-1} for O_2 in the $5^{12}(O_2)$ cage and 1482 cm^{-1} for O_2 in the $5^{12}6^4(O_2)$ cage. These observations suggest that the ν_1 mode in the $5^{12}(O_2)$ and $5^{12}6^4(O_2)$ cages shows a red-shift relative to the ν_1 mode of free O_2 molecule. The observed red-shift can be attributed to the attractive interactions which exist between the O_2 and the water molecules. Champagnon et. al. [200] reported the ν_1 mode in the $5^{12}(O_2)$ and $5^{12}6^4(O_2)$ cages appears at 1511 cm^{-1} and 1509 cm^{-1} respectively. Horikawa et. al. [202] observed that the ν_1 mode in the $5^{12}(O_2)$ and $5^{12}6^4(O_2)$ cages appears at 1592 cm^{-1} and 1575 cm^{-1} respectively. The trends in the ν_1 mode (from our work) are in qualitatively agreement with the results of Champagnon et. al. [200] and Horikawa et. al. [202] on the hydrate lattice.

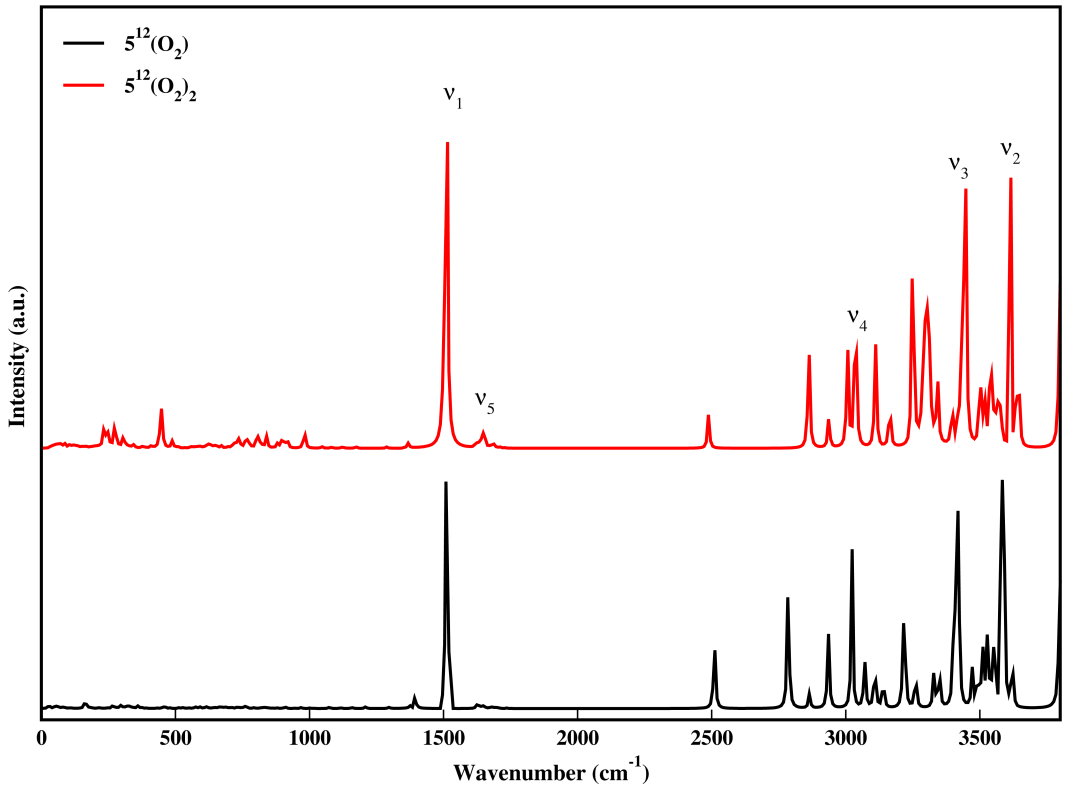

Figure 8.3: Vibrational Raman spectra in $5^{12}(O_2)$ and $5^{12}(O_2)_2$ cages.

However, for varying occupancies of O_2 molecules in the 5^{12} and $5^{12}6^4$ cages, the ν_1 mode shows blue-shift relative to the $5^{12}(O_2)$ and $5^{12}6^4(O_2)$ cages. The blue-shift occurs due to the repulsion which exists between the O_2 molecules which leads to the expansion of the cavity radii. The blue-shift is high for the $5^{12}6^4(O_2)_3$ compared to the $5^{12}6^4(O_2)_2$ cages.

The vibrational Raman spectra of water molecules in various cages are displayed in Figure **8.3** and Figure **8.4** and the corresponding peak intensities are shown in Table **8.2**. The peak frequencies from the ν_2, ν_3 and ν_4 modes in the $5^{12}(O_2)$ cage is red-shifted by 62 cm^{-1}, 69 cm^{-1} and 352 cm^{-1} respectively, relative to the 5^{12} cage. However, the ν_2, ν_3 and ν_4 modes for the $5^{12}(O_2)_2$ is blue-shifted by 29 cm^{-1}, 27 cm^{-1} and 221 cm^{-1} relative to the $5^{12}(O_2)$ cage. The blue-shift suggest that there exist repulsive interactions between the two oxygen molecules resulting in an increase in the cavity radii of 4.20 Å, compared to the 4 Å, radius of the $5^{12}(O_2)$ cage. The spectral shifts validate the interaction energy that the $5^{12}(O_2)$ cage is most stable.

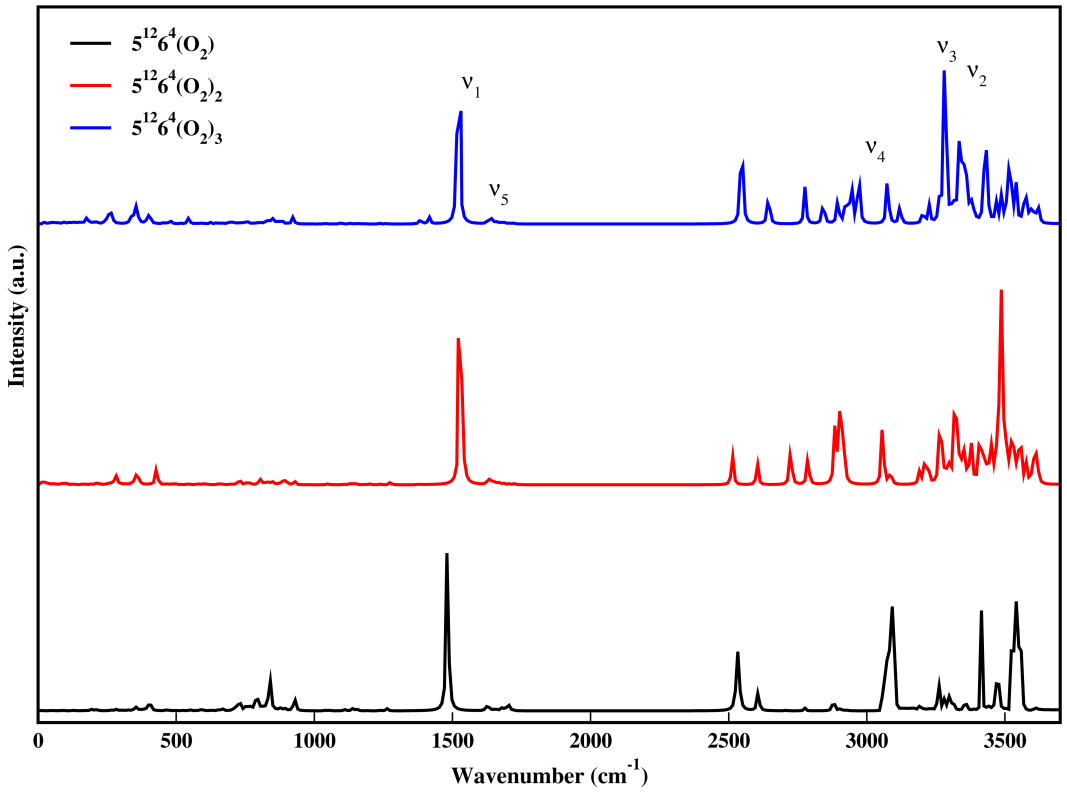

Figure 8.4: Vibrational Raman spectra in $5^{12}6^4(O_2)$, $5^{12}6^4(O_2)_2$ and $5^{12}6^4(O_2)_3$ cages.

Table 8.2: Raman frequencies (cm^{-1}) peak assignment in the $5^{12}(O_2n = 0-2)$ and $5^{12}6^4(O_2)_{n=0-3}$ cages (reference: isolated O_2).

Modes	**O_2**	**5^{12}**	**$5^{12}(O_2)$**	**$5^{12}(O_2)_2$**	**$5^{12}6^4$**	**$5^{12}6^4(O_2)$**	**$5^{12}6^4(O_2)_2$**	**$5^{12}6^4(O_2)_3$**
ν_1	1532	-	1509 1511[a] 1592[b]	1515	-	1482 1509[a] 1575[b]	1521	1531
ν_2	-	3647[c]	3585	3614	3621[c]	3546	3527	3599
ν_3	-	3488[c]	3419	3446	3494[c]	3416	3407	3512
ν_4	-	3375[c]	3023	3244	3332[c]	3092	3057	3281
ν_5	-	1643[c]	1642	1651	1639[c]	1637	1632	1661

[a]Ref [200],[b]Ref [202], [c]Ref [219]

Similarly, the peak frequencies from the ν_2, ν_3 and ν_4 modes in the $5^{12}6^4(O_2)$ cage is red-shifted by 75 cm^{-1}, 78 cm^{-1} and 240 cm^{-1} respectively, relative to the $5^{12}6^4$ cage.

Further, the ν_2, ν_3 and ν_4 modes in the $5^{12}6^4(O_2)_2$ cage is red-shifted by 19 cm^{-1}, 9 cm^{-1} and 35 cm^{-1} respectively, relative to the $5^{12}6^4$ (O_2) cage. In contrast, the ν_2, ν_3 and ν_4 modes in the $5^{12}6^4(O_2)_3$ cage is blue-shifted by 72 cm^{-1}, 105 cm^{-1} and 224 cm^{-1} respectively, relative to the $5^{12}6^4(O_2)_2$ cage. This is due to repulsive interaction between the three oxygen molecules which leads to the expansion of the cavity radii (4.7 Å) and hence reduced interaction with the water molecules of the cages. It is seen that the bending overtone (ν_4) modes are significantly affected with the encapsulation of oxygen molecules in the 5^{12} and $5^{12}6^4$ cages relative to the ground state vibrational modes (ν_2 and ν_3) of water molecules. The bending (ν_5) mode of water molecules also shows trends similar to other vibrational modes of water molecules, though the shifts are very small. The ν_1 mode in the $5^{12}(O_2)$ cage shows very small red-shift by 1 cm^{-1} relative to the 5^{12} cage. However, the $5^{12}(O_2)_2$ cage shows blue-shift by 9 cm^{-1} relative to the $5^{12}(O_2)$ cage. Similarly, the ν_5 mode of vibration in the $5^{12}6^4(O_2)$ shows a 2 cm^{-1} red-shifted relative to the $5^{12}6^4$ cage and $5^{12}6^4(O_2)_2$ cages shows a 5 cm^{-1} red-shifted relative to the $5^{12}6^4(O_2)$ cage. However, the $5^{12}6^4(O_2)_3$ cage shows a 29 cm^{-1} blue-shifted relative to the $5^{12}6^4(O_2)_2$ cage.

8.4 Conclusions

The interaction energies shows that $5^{12}(O_2)$ cage and $5^{12}6^4(O_2)_2$ cage to be the most stable. The trends observed for the varying occupancies of O_2 in the 5^{12} and $5^{12}6^4$ cages are as follows: the O_2 stretch, asymmetric and symmetric stretch, bending overtone and bending modes of water molecules in the $5^{12}(O_2)$, $5^{12}6^4(O_2)$ and $5^{12}6^4(O_2)_2$ cages are red-shifted relative to the 5^{12}, $5^{12}6^4$ and $5^{12}6^4(O_2)$ cages whereas, the modes in the $5^{12}(O_2)_2$ and $5^{12}6^4(O_2)_3$ was found to be blue-shifted relative to the $5^{12}(O_2)$ and $5^{12}6^4(O_2)_2$ cages. A characterization of CH_4 replacement by CO_2 in the cages of clathrate hydrates using AIMD simulations and an examination of H_2 clathrate hydrate formation and nucleation can be the focus of future activities and is discussed in the next chapter.

Chapter 9

Summary

9.1 Conclusions

The salient features of the thesis are as follows:

- In **Chapter 1**, an overview and background of clathrate hydrates is discussed. A brief description of DFT and various properties used for characterization of cages of clathrate hydrates is also presented.

- In **Chapter 2**, the thermodynamic stability and computed reactivity indices of cages of methane clathrate hydrates is characterized. The interaction energies are very sensitive to the choice of basis set, functionals and method. The interaction energy and free energy calculations show that CH_4 is more spontaneous and stable in the 5^{12} cage compared to $5^{12}6^2$ cage. The computed reactivity indices show that $5^{12}6^2CH_4$ cage is more electrophilic compared to the $5^{12}CH_4$ cage.

- In **Chapter 3**, the vibrational Raman spectra associated with the encapsulation of CH_4 in 5^{12} and $5^{12}6^2$ cages is investigated. The symmetric and asymmetric C-H stretch in the $5^{12}CH_4$ cage is blue-shifted due to dispersion interaction of the encapsulated CH_4 molecule with the water molecules of the cages. However, the symmetric and asymmetric O-H stretch of water molecules in $5^{12}CH_4$ and $5^{12}6^2CH_4$ cages are red-shifted due to hydrogen bonding interactions with the encapsulated

CH_4 molecule. The CH_4 bending modes in the $5^{12}CH_4$ and $5^{12}6^2CH_4$ cages are blue shifted, though the magnitude of the shifts are lower compared to modes in the high frequency region which suggest bending modes are less affected on encapsulation of CH_4. The low frequency librational modes which are collective motion of the water molecules and CH_4 in these cages show a broad range of frequencies which suggests that these modes largely contribute to the formation of the hydrate lattice.

- In **Chapter 4**, the various reaction pathways of diffusion of CH_4 in 5^{12} and $5^{12}6^2$ cages is characterized using CI-NEB method with three exchange correlation functionals (D3, DF1 and DF2). The adsorption energy shows that CH_4 molecule stabilizes 5^{12} and $5^{12}6^2$ cages. The activation energy is less when diffusion of CH_4 occurs via the hexagonal gate compared to the pentagonal gate of the $5^{12}6^2$ cage. The activation energy is less when diffusion of CH_4 occurs via the pentagonal gate in the 5^{12} cage compared to the pentagonal and hexagonal gate of $5^{12}6^2$ cage. The rate constant for diffusion of CH_4 via the pentagonal gate of the 5^{12} cage is 10^8 times larger than the pentagonal gate of the $5^{12}6^2$ cage. The rate constant for diffusion of CH_4 via the hexagonal gate is 10^2 times larger than the pentagonal gate in $5^{12}6^2$ cage. The activation energy is least when diffusion of CH_4 occurs in $5^{12}6^2 \overset{Pen}{\longleftrightarrow} 5^{12}$ cages compared to $5^{12}6^2 \overset{Pen}{\longleftrightarrow} 5^{12}6^2$ and $5^{12}6^2 \overset{Hex}{\longleftrightarrow} 5^{12}6^2$ cages. The activation energy of the diffusion of CH_4 in fused cages are higher than the single cages due to interfacial diffusion.

- In **Chapter 5**, the thermodynamic stability and hydrogen storage capacity of cages of pure and THF doped hydrogen clathrate hydrates is investigated. The free energy shows that a single occupancy in 5^{12} and quadruple occupancy of H_2 in the $5^{12}6^4$ cages is stable compared to other occupancies. However, with the encapsulation of THF in the $5^{12}6^4$ cage, only a single occupancy of H_2 in the $5^{12}6^4$ cage is stable. The calculations predict a 3.77 wt % and 1.92 wt % of hydrogen in the cages of pure and THF doped hydrogen clathrate hydrates and is consistent with experimental observations.

- In **Chapter 6**, the vibrational Raman spectra of cages of pure and THF doped hydrogen clathrate hydrates is determined. The spectral shifts suggest that the $5^{12}(H_2)$, $5^{12}6^4(H_2)_4$ and $5^{12}6^4(H_2)$.THF cages is more stable compared to $5^{12}(H_2)_2$, $5^{12}6^4(H_2)_{n=1-3}$ and $5^{12}6^4(H_2)_2$.THF cages respectively. The trends observed from the calculated Raman vibrational modes are in agreement with previous experimental findings.

- In **Chapter 7** and **8**, stability and vibrational Raman spectra of cages of nitrogen and oxygen clathrate hydrates are discussed. The interaction energy and spectral shifts suggest the $5^{12}(N_2)$ and $5^{12}6^4(N_2)_2$ cages are more stable compared to the $5^{12}(N_2)_2$ and $5^{12}6^4(N_2)_{n=1,3}$ cages. Similar trends are observed for oxygen clathrate hydrates.

The work presented in this thesis describes the structure, energy, stability and spectral properties of cages of clathrate hydrates characterized using Density Functional Theory.

9.2 Future directions

A molecular level understanding on the mechanism of formation and decomposition of clathrate hydrates can assist in the synthesis and characterization of these materials for various technological applications. The possible objectives of future study are:

9.2.1 Extraction of methane from clathrate hydrates using replacement mechanism of CO_2: Insights from *ab initio* MD simulations

The extraction of CH_4 from clathrate hydrates can lead to geological disasters like earthquakes, submarine landslides, etc [7]. On the other hand, the emission of CO_2 into the atmosphere from fossil fuels increases and is considered as the main cause of global warming [220, 221]. However, CO_2 emissions can be reduced by an appropriate selection of materials which can provide and enhance CO_2 sequestration [222]. In order to address the

issues of CH_4 extraction from clathrate hydrates and CO_2 sequestration, Ebinuma [223] and Ohgaki et. al. [224] proposed a replacement of CH_4 in clathrate hydrates by CO_2. This method has the following advantages: i) The CO_2 sequestration occurs in an environmentally friendly material. ii) The extraction of CH_4 can serve as an alternative energy fuel. The authors concluded that such a replacement mechanism avoids traditional mining methods and sequestration of CO_2 could stabilize the stratum above the ocean floor [224, 225].

Experimental methods based on NMR spectroscopy of Lee et. al. [226] have shown that CO_2 prefers to occupy the $5^{12}6^2$ cage compared to the 5^{12} cage of the sI hydrate. However, the authors observed the destabilization of the hydrate lattice, when CH_4 was replaced by CO_2. Further, the authors concluded that the reaction rate of the replacement mechanism depends on the degree of hydrate dispersion in sediment, particle size of the hydrate, and the diffusion of CH_4 and CO_2. Yoon et. al. [227] employed Raman spectroscopy and observed a 60 % recovery of CH_4 from clathrate hydrates using CO_2. Uchida et. al. [228] employed Raman spectroscopy and gas chromatography to investigate the kinetics and stability of CH_4 - CO_2 binary clathrate hydrates. The authors observed that long-term storage of these binary clathrate hydrates is less effective as CO_2 prefers $5^{12}6^2$ cage, and CH_4 prefers 5^{12} cage under suitable thermodynamic conditions. Park et. al. [229] employed NMR and Raman spectroscopy to investigate the replacement of CH_4 by using CO_2 and a binary mixture of C_2H_6 + CO_2. The authors observed a 85 % recovery of CH_4, when binary mixture of C_2H_6 + CO_2 is used, whereas a 65% recovery of CH_4 is observed in the case of CO_2. The authors observed that during the replacement, the sI clathrate hydrate transforms to an sII form (see Figure **9.1**). However, the authors failed to observe a complete replacement of CH_4 by CO_2.

MD simulations also been employed to study the replacement mechanism. Yezdimer et. al. [230] performed MD simulations and concluded that the replacement of CH_4 by CO_2 is thermodynamically favorable. Dornan et. al. [231] employed MD simulations to observe the replacement of CH_4 using CO_2 and a binary mixture of CO_2 + N_2 in sI hydrate. The authors observed that CH_4 in 5^{12} cages and CO_2 in $5^{12}6^2$ cages to be most

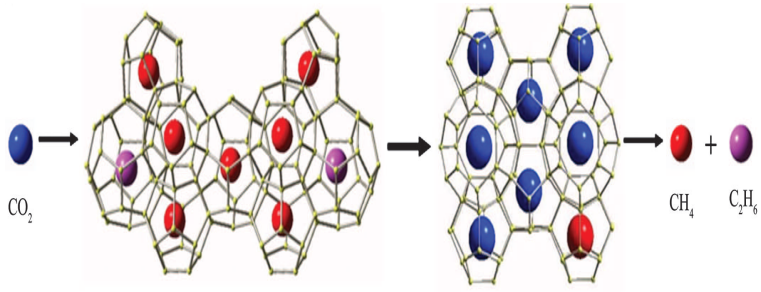

Figure 9.1: Schematic diagram of CH_4 + C_2H_6 hydrate replaced with CO_2. (Adapted from Park et. al. [229]. Copyright (2014) from Proc. Natl. Acad. Sci.)

stable (see Figure **9.2**).

While, experimental and theoretical studies have attempted to investigate the re-

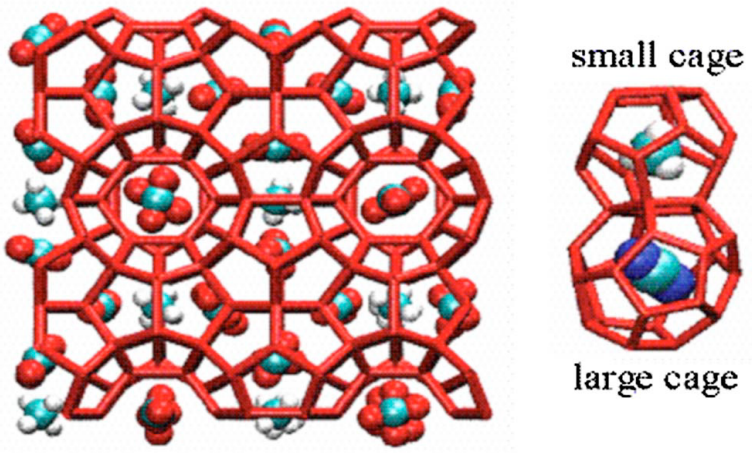

Figure 9.2: A snapshot of the 2x2x2 unit cell replica of the sI CO_2L/CH_4S mixed clathrate hydrates left. A close-up of a small cage with the CH_4 guest and large cage with CO_2 guest are also shown right. The oxygen atoms of the clathrate water framework are connected by lines. (Adapted from Dorman et. al. [231]. Copyright (2014) from American Physics Society)

placement mechanism, the fundamental understanding of the reaction pathways, energy barriers and kinetics of these reactions remains poorly understood. The objective of the proposed work is to employ AIMD and CI-NEB to characterize the diffusion of CH_4 and CO_2 during the replacement mechanism. The mechanism of CH_4 replacement by CO_2, structural changes and amount of CH_4 released can be calculated using the AIMD method.

9.2.2 Tuning storage capacity of hydrogen clathrate hydrates

Hydrogen clathrate hydrates continue to attract attention due to its minimal impact on environment (where only water is a by-product on release of hydrogen). The synthesis of hydrogen clathrate hydrates requires extreme thermodynamic conditions and is known to reduce with the addition of secondary dopants such as N_2, THF, methyl-cyclohexane (MCH) and methyl-tert-butyl-ether (MTBE). However, the addition of dopants reduces the storage capacity. A schematic representation of hydrogen storage in pure and THF doped clathrate hydrates is shown in Figure **9.3** [164]. As seen, the hydrogen storage capacity reduces with an increase in THF concentration [164] (see Figure **9.3**). The objective of the proposed work is to employ *ab initio* methods (DFT, AIMD) to characterize storage capacity by inclusion of alternate dopants which can provide enhanced hydrogen storage. Further, understanding the mechanism of formation of stable hydrogen clathrate hydrates with other dopants can be characterized using the CI-NEB method.

9.2.3 Nucleation mechanism of clathrate hydrates

An understanding of nucleation mechanism of clathrate hydrates continues to generate interest as they play a key role in the design and synthesis of novel clathrate hydrates. Experimental efforts to understand the process of nucleation have remained limited due to the small size of the clathrate hydrate nuclei [7, 9]. However, MD simulations have attained popularity to investigate the mechanism of nucleation. Computationally, nucleation is considered as a rare event due to its occurrence at long simulation time scales (For example, the nucleation event occurs after $\sim$ 300 ns). As a result, investigation of nucleation using MD simulations is a computationally challenging task. Nevertheless, several MD simulations have been performed to observe nucleation of clathrate hydrates [31–36, 121, 122, 232–235]. For example, Moon et. al. [31–33] observed the process of nucleation at the water-methane interface at 300 ns. However, Molinero and coworkers [121, 122, 232] observed nucleation mechanism using inhibitors in water-methane interface at 200 ns. Pirzadeh et. al. [235] investigated the water-methane interface nucle-

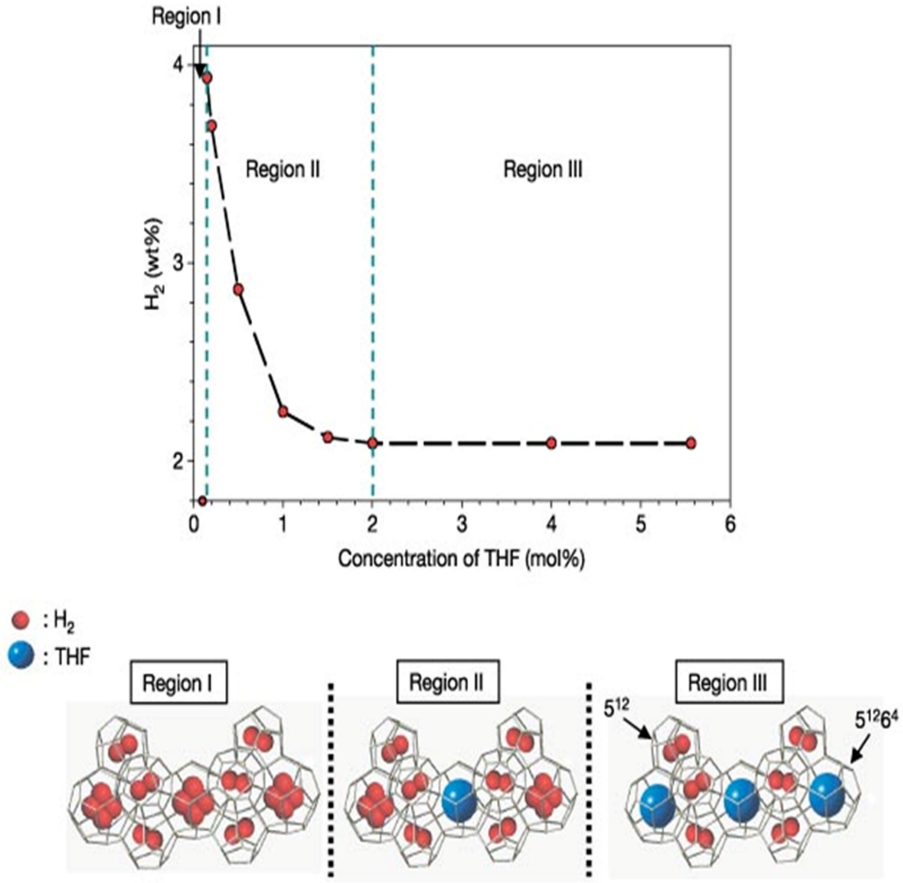

Figure 9.3: H_2 gas content as a function of THF concentration and schematic diagram of H_2 distribution in the cages of THF+H_2 hydrate. In region III, H_2 gas is stored only in small cages and THF is stored in large cages. In region I and II H_2 can be stored in small and large cages. (Adapted from Lee et. al. [164]. Copyright (2014) from Nature)

.

ation mechanism and observed an amorphous form of methane clathrate hydrates. Contrary to previous work, Walsh et. al. [233] observed nucleation using a random mixing of methane and water molecules. Similarly, Sarupria et. al. [234] observed nucleation using microsecond simulations in the absence of water-methane interface (see Figure **9.4**). The authors observed the initial stages of formation at 400 ns and a more crystalline phase at 1000 ns.

A summary of the work performed using MD simulations invokes the following unanswered questions.

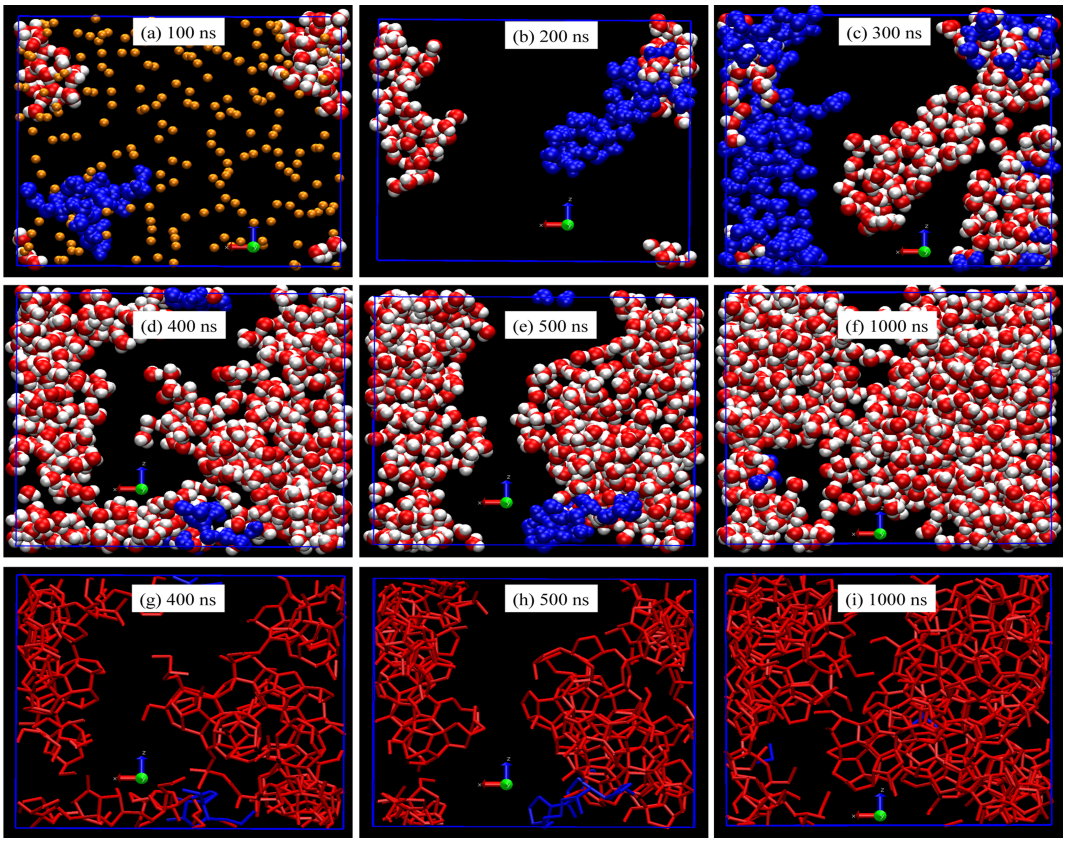

Figure 9.4: (a-f) Snapshots at different times from one nucleation trajectory. Water molecules belonging to the largest cluster are shown in red and white (for oxygen and hydrogen, respectively), and those in the second largest cluster are shown in blue. The orange spheres in panel a are methane molecules. (g-i) Snapshots in g, h, and i panels are the same as d, e, and f shown in a different rendering. The largest cluster is shown in red and the second largest cluster is in blue. (Adapted from Sarupria et. al. [234]. Copyright (2014) from American Chemical Society)

- What is the mechanism of nucleation in the presence and absence of water-methane interface?
- How does an interface facilitate the process of nucleation?
- Can a secondary dopant enhance or inhibit the process of nucleation?

The objective of the proposed work is to provide a systematic understanding on the mechanism of nucleation which can answer the above questions. This can be done by a development of a flexible water force field (based on TIPnP/ice water models) required for the

examination of nucleation at various thermodynamic conditions.

Appendix A

Optimized geometry of the 5^{12} cage			
H	11.74546	6.54652	17.52049
H	11.23346	5.16032	18.05682
H	12.10756	10.22074	21.18290
H	13.23381	9.25931	21.72057
H	7.11350	7.88349	19.49585
H	6.45529	8.71373	18.32727
H	12.54553	11.95956	15.84110
H	12.43768	12.21420	14.29022
H	7.90108	9.73008	14.88532
H	6.95206	10.78217	14.19653
H	7.64747	12.96245	18.89046
H	6.59751	11.82199	18.70395
H	8.87120	7.74021	20.99390
H	8.01850	9.03760	21.20966
H	13.56646	11.20148	17.77624
H	14.25970	12.57457	17.39691
H	8.68542	7.67269	15.57567
H	8.63306	7.69855	13.98239
H	12.46752	8.09622	15.90384
H	13.70555	7.15450	16.19485
H	9.13546	13.53523	17.03805
H	8.85230	14.86630	17.83553
H	11.27505	12.31676	20.58044
H	11.11530	12.18793	22.14886
H	10.81679	6.82589	19.84262
H	11.33342	7.89864	20.84565
H	13.53034	8.94107	17.85619
H	13.42130	9.55366	19.31127
H	9.26671	6.50908	17.29393
H	7.80053	7.11066	17.49662
H	11.69606	9.92841	14.81777
H	10.64651	8.74794	14.72940
H	10.19479	12.43754	15.31509
H	8.68220	12.00821	15.34818
H	6.37221	10.50964	16.57324
H	4.98536	10.45553	17.30455

Appendix A

H	10.71645	13.59587	18.79881
H	12.15712	12.98806	18.59245
H	7.74995	11.43585	20.72618
H	9.17123	11.11322	21.28332
O	11.01202	6.10489	18.01458
O	12.96176	7.60366	16.62892
O	11.61069	8.95326	14.73878
O	8.84414	8.26149	14.74577
O	8.44264	6.74244	16.81768
O	6.69633	7.80437	18.59180
O	7.42594	10.59742	15.02423
O	7.94565	8.06909	21.03301
O	5.94401	10.46190	17.45937
O	8.22717	10.88498	21.39060
O	6.95649	12.45246	19.36204
O	13.81588	9.69449	18.41878
O	13.40269	12.11748	17.38236
O	11.97731	11.80211	15.03955
O	12.62796	9.39856	20.97447
O	11.11396	11.66837	21.32841
O	11.55182	13.36319	19.26688
O	9.08740	13.93146	17.95333
O	9.28804	12.76640	15.49713
O	10.69875	7.15907	20.75515

Appendix A

Optimized geometry of the $5^{12}6^2$ cage			
H	12.03697	8.87942	20.52128
H	13.26932	9.44235	19.70746
H	12.10145	11.20762	20.58641
H	12.16447	12.51993	21.46171
H	11.07521	6.87944	21.48207
H	9.93400	7.57341	20.64276
H	11.36530	6.39829	19.09722
H	10.77976	5.75679	17.79175
H	7.84647	7.38381	19.76811
H	7.92536	8.72241	20.59509
H	6.72504	10.62855	21.44187
H	7.91443	11.18085	20.56919
H	6.13481	10.62026	19.07781
H	5.88060	11.47153	17.78589
H	8.81604	13.09790	19.69911
H	9.94543	12.35145	20.51063
H	12.50402	13.02659	19.08839
H	13.34011	12.79667	17.78229
H	14.44090	10.66780	17.28838
H	15.17679	11.78280	16.45745
H	14.11364	8.44886	17.68966
H	15.34698	8.88405	18.59646
H	12.80363	6.76625	17.27475
H	13.04438	7.59030	15.94098
H	6.39304	5.92365	18.54160
H	6.64481	7.23157	17.67762
H	8.40417	5.81337	17.26441
H	9.02509	4.61422	16.45404
H	5.78068	9.20878	17.27307
H	6.40557	8.60306	15.94852
H	8.27627	15.18303	18.56623
H	9.26849	14.30442	17.68787
H	7.15050	13.50686	17.27544
H	5.81545	13.57798	16.44397
H	9.45929	6.71947	15.24952
H	10.43825	7.67830	14.46251

Appendix A

H	13.14634	11.15635	15.25003
H	11.83600	11.53127	14.45188
H	7.41599	12.15512	15.25419
H	7.76262	10.83243	14.46241
H	11.42223	14.02036	17.29069
H	10.58400	13.79598	15.96377
H	10.47623	13.31484	13.58012
H	9.51168	12.37142	14.39783
H	12.64382	7.94569	13.56045
H	12.31853	9.25630	14.37984
H	8.22113	8.41688	14.40540
H	6.92995	8.76904	13.57010
O	12.66913	9.63168	20.46222
O	11.79825	12.16380	20.63563
O	10.92068	7.39089	20.67089
O	11.61603	5.91494	18.27886
O	8.26216	7.79753	20.55698
O	7.22942	10.44960	20.63113
O	5.58685	10.66682	18.26282
O	8.97215	12.49039	20.45529
O	12.80145	13.46315	18.25956
O	14.29649	11.48373	16.73785
O	14.48613	9.19560	18.27151
O	13.48290	7.28118	16.76435
O	7.09989	6.52032	18.24505
O	9.18849	5.53353	16.72104
O	5.91868	8.36421	16.76817
O	8.42104	14.27624	18.24965
O	6.51484	12.96885	16.73158
O	9.51665	7.33248	14.48461
O	12.60403	10.91540	14.46752
O	7.91974	11.80445	14.48768
O	10.61944	14.32539	16.79103
O	10.43533	12.76314	14.37867
O	12.20388	8.25837	14.36791
O	7.40970	9.00776	14.38035

Appendix B

Table B2-1: Total energies (a.u.) using the DFT/M05-2X functional.

Basis set	E(5^{12})	E($5^{12}CH_2$)	E($5^{12}6^2$)	E($5^{12}CH_4$)	E(H_2O)	E(CH_4)
6-31G	-1527.4500	-1567.8922	-1832.9972	-1873.4382	-76.3460	-40.4341
6-31G(d,p)	-1527.9395	-1568.3992	-1833.5509	-1874.0095	-76.3802	-40.4509
6-31++G(d,p)	-1528.1884	-1568.6485	-1833.8301	-1874.2892	-76.3935	-40.4508
6-311G(d,p)	-1528.4743	-1568.9458	-1834.1725	-1874.6428	-76.4087	-40.4611
6-311++G(d,p)	-1528.6371	-1569.1112	-1834.3854	-1874.8583	-76.4190	-40.4613
cc-pVDZ	-1527.9556	-1568.4110	-1833.5684	-1874.0227	-76.3820	-40.4467
cc-pVTZ	-1528.7366	-1569.2167	-1834.5036	-1874.9833	-76.4241	-40.4708
cc-pVQZ	-1528.7895	-1569.2775	-1834.5689	-1875.0551	-76.4295	-40.4747
aug-cc-pVDZ	-1528.3698	-1568.8330	-1834.0629	-1874.5245	-76.4065	-40.4512

Appendix B

Table B3-1: Raman frequencies (cm^{-1}) peak assignments from B97-D and M05-2X (in parenthesis).

Modes	**H_2O**	**CH_4**	**5^{12}**	**$5^{12}CH_4$**	**$5^{12}6^2$**	**$5^{12}6^2CH_4$**
Libration (ν_1)	-	-	27-859	14-876	37-897	20-941
	-	-	(41-784)	(18-825)	(39-909)	(31-913)
Bend (ν_2)	-	1306	-	1315	-	1308
	-	(1362)	-	(1346)	-	(1354)
Rock (ν_3)	-	1518	-	1526	-	1517
	-	(1583)	-	(1585)	-	(1578)
Bend (ν_4)	1587	-	1629	1627	1626	1625
	(1653)	-	(1638)	(1635)	(1632)	(1630)
Symmetric stretch (ν_5)	-	2928	-	2939	-	2918
	-	(3077)	-	(3067)	-	(3061)
Asymmetric stretch (ν_6)	-	3055	-	3071	-	3066
	-	(3189)	-	(3172)	-	(3169)
Symmetric stretch (ν_7)	3739	-	3643	3572	3484	3449
	(3856)	-	(3680)	(3673)	(3653)	(3647)
Asymmetric stretch (ν_8)	3855	-	3811	3808	3802	3797
	(3976)	-	(3956)	(3952)	(3954)	(3949)

Appendix B

Table B5-1: Total energies (a.u.) from five structures of 5^{12} and $5^{12}6^4$ cages.

Cage	S1	S2	S3	S4	S5
$5^{12}(H_2)$	-1529.9318	-1529.9343	-1529.9367	-1529.9443	-1529.9491
$5^{12}(H_2)_2$	-1531.0981	-1531.1096	-1531.1157	-1531.1275	-1531.1317
$5^{12}6^4(H_2)$	-2141.4458	-2141.4480	-2141.4481	-2141.4488	-2141.4640
$5^{12}6^4(H_2)_2$	-2142.6328	-2142.6348	-2142.6350	-2142.6355	-2142.6492
$5^{12}6^4(H_2)_3$	-2143.8195	-2143.8215	-2143.8221	-2143.8223	-2143.8226
$5^{12}6^4(H_2)_4$	-2144.9493	-2145.0026	-2145.0072	-2145.0076	-2145.0077
$5^{12}6^4(H_2)$.THF	-2373.8484	-2373.8512	-2373.8523	-2373.8525	-2373.8586
$5^{12}6^4(H_2)_2$.THF	-2375.0300	-2375.0323	-2375.0339	-2375.0473	-2375.0498
$5^{12}6^4$.THF	-2372.6386	-2372.6686	-2372.6705	-2372.6811	-2372.6848

Appendix B

Table B5-2: Interaction energy (includes BSSE and ZPVE) in kcal/mol for each occupancy of hydrogen in 5^{12} and $5^{12}6^4$ cages. For each cage, structures S1 - S5 differ in the orientation of protons. ZPVE (kcal/mol) contributions to interaction energy in parenthesis.

Cage	S1	S2	S3	S4	S5
$5^{12}(H_2)$	-1.91	-1.98	-2.02	-2.25	-2.30
	(0.52)	(0.64)	(1.11)	(0.89)	(0.98)
$5^{12}(H_2)_2$	3.07	0.34	0.27	-0.74	-1.21
	(2.69)	(3.09)	(3.21)	(3.86)	(3.33)
$5^{12}6^4(H_2)$	-1.31	-1.52	-1.55	-1.58	-2.29
	(0.86)	(0.69)	(0.94)	(0.98)	(1.12)
$5^{12}6^4(H_2)_2$	-2.30	-2.57	-2.59	-2.61	-3.42
	(1.10)	(1.32)	(1.37)	(1.35)	(1.30)
$5^{12}6^4(H_2)_3$	-3.10	-3.25	-3.37	-3.68	-3.89
	(2.12)	(2.11)	(2.08)	(2.37)	(2.30)
$5^{12}6^4(H_2)_4$	-4.10	-4.24	-4.29	-4.30	-4.80
	(2.81)	(2.80)	(2.91)	(2.89)	(2.78)
$5^{12}6^4(H_2)$.THF	-5.16	-5.28	-5.48	-5.50	-5.92
	(1.48)	(1.38)	(1.00)	(1.23)	(1.84)
$5^{12}6^4(H_2)_2$.THF	-1.23	-1.30	-1.42	-1.45	-1.56
	(3.91)	(3.80)	(3.89)	(3.79)	(3.92)

Appendix B

Table B6-1a: Raman peak assignments (cm^{-1}) of 5^{12} cage.

Assignments	S1	S2	S3	S4	S5	Average and standard deviation
ν_2	3584	3581	3608	3592	3539	3580 [23]
ν_3	3489	3480	3492	3526	3476	3484 [5.8]
ν_4	3186	3208	3200	3211	3200	3197 [8.5]
ν_5	1642	1642	1650	1649	1645	1645 [3.4]

Table B6-1b: Raman peak assignments (cm^{-1}) of $5^{12}(H_2)$ cage.

Assignments	S1	S2	S3	S4	S5	Average and standard deviation
ν_1	4388	4380	4363	4361	4366	4372 [11]
ν_2	3566	3545	3593	3590	3586	3576 [18]
ν_3	3474	3454	3469	3449	3460	3461 [9.2]
ν_4	3184	3191	3292	3156	3123	3183 [15]
ν_5	1638	1637	1649	1638	1639	1640 [4.4]

Table B6-1c: Raman peak assignments (cm^{-1}) of $5^{12}(H_2)_2$ cage.

Assignments	S1	S2	S3	S4	S5	Average and standard deviation
ν_1	4418	4401	4402	4398	4404	4405 [7.0]
ν_2	3560	3587	3637	3604	3566	3591 [28]
ν_3	3473	3482	3495	3499	3485	3487 [9.3]
ν_4	3198	3199	3240	3242	3168	3208 [29]
ν_5	1648	1652	1649	1648	1655	1654 [2.7]

Appendix B

Table B6-1d: Raman peak assignments (cm^{-1}) of $5^{12}6^4$ cage.

Assignments	S1	S2	S3	S4	S5	Average and standard deviation
ν_2	3563	3587	3590	3581	3569	3578 [10]
ν_3	3488	3466	3486	3491	3486	3482 [9.0]
ν_4	3196	3195	3199	3192	3194	3195 [2.3]
ν_5	1644	1643	1642	1645	1642	1643 [1.2]

Table B6-1e : Raman peak assignments (cm^{-1}) of $5^{12}6^4(H_2)$ cage.

Assignments	S1	S2	S3	S4	S5	Average and standard deviation
ν_1	4362	4368	4376	4369	4383	4372 [7.2]
ν_2	3525	3514	3526	3520	3532	3523 [6]
ν_3	3472	3456	3454	3486	3452	3464 [13]
ν_4	3144	3162	3156	3182	3185	3166 [15]
ν_5	1644	1645	1642	1642	1640	1643 [1.7]

Table B6-1f : Raman peak assignments (cm^{-1}) of $5^{12}6^4(H_2)_2$ cage.

Assignments	S1	S2	S3	S4	S5	Average and standard deviation
ν_1	4382	4379	4376	4381	4381	4380 [2.1]
ν_2	3501	3517	3522	3521	3505	3513 [8.6]
ν_3	3472	3478	3475	3473	3474	3464 [2.0]
ν_4	3141	3160	3149	3165	3192	3161 [17]
ν_5	1636	1641	1642	1639	1637	1639 [2.3]

Appendix B

Table B6-1g : Raman peak assignments (cm^{-1}) of $5^{12}6^4(H_2)_3$ cage.

Assignments	S1	S2	S3	S4	S5	Average and standard deviation
ν_1	4382	4384	4385	4384	4393	4386 [3.8]
ν_2	3498	3515	3502	3500	3493	3502 [7.3]
ν_3	3463	3442	3465	3466	3435	3454 [13]
ν_4	3133	3165	3177	3176	3162	3160 [15]
ν_5	1637	1641	1639	1638	1634	1637 [2.3]

Table B6-1h: Raman peak assignments (cm^{-1}) of $5^{12}6^4(H_2)_4$ cage.

Assignments	S1	S2	S3	S4	S5	Average and standard deviation
ν_1	4389	4392	4392	4388	4398	4392 [3.5]
ν_2	3497	3492	3516	3502	3491	3499 [9.1]
ν_3	3434	3445	3451	3467	3427	3445 [14]
ν_4	3147	3124	3154	3182	3103	3142 [26]
ν_5	1636	1632	1638	1637	1631	1635 [2.8]

Table B6-1i : Raman peak assignments (cm^{-1}) of $5^{12}6^4(H_2)$.THF cage.

Assignments	S1	S2	S3	S4	S5	Average and standard deviation
ν_1	4372	4368	4380	4376	4374	4374 [4.0]
ν_2	3527	3535	3548	3526	3530	3533 [8.0]
ν_3	3456	3457	3450	3467	3460	3458 [5.5]
ν_4	3155	3165	3185	3174	3170	3169 [9.9]
ν_5	1640	1632	1638	1644	1634	1637 [4.3]

Appendix B

Table B6-1j: Raman peak assignments (cm^{-1}) of $5^{12}6^4(H_2)_2$.THF cage.

Assignments	S1	S2	S3	S4	S5	Average and standard deviation
ν_1	4436	4443	4440	4442	4434	4439 [3.5]
ν_2	3591	3584	3596	3590	3580	3588 [5.6]
ν_3	3502	3516	3508	3512	3500	3507 [6.0]
ν_4	3204	3225	3192	3208	3216	3209 [11]
ν_5	1657	1649	1652	1655	1650	1652 [3.0]

Bibliography

[1] G. A. Jeffrey, Hydrate inclusion compounds. In Inclusion Compounds; J. L. Atwood, J. E. D. Davies, D. D. McNicol, Eds.; Academic Press: London. **1**, 135 (1984).

[2] K. A. Kvenvolden, Proc. Natl. Acad. Sci. **96**, 3420 (1999).

[3] K. A. Kvenvolden, Ann NY Acad Sci. **912**, 17 (2000).

[4] C. A. Koh, Chem. Soc. Rev. **31**, 157 (2002).

[5] E. D. Sloan, Jr, Nature. **426**, 353 (2003).

[6] K. Nath, J. Surface. Sci. Technol. **23**, 59 (2007).

[7] E. D. Sloan, C. A. Koh, Clathrate Hydrates of Natural Gases, 3rd ed. CRC, Boca Raton, FL, (2007).

[8] R. Boswell, Science. **325**, 957 (2009).

[9] A. K. Sum, C. A. Koh, E. D. Sloan, Ind. Eng. Chem. Res. **48**, 7457 (2009).

[10] a) H. Davy, Philos. Trans. R. Soc. London. **101**, 1 (1811); b) M. Faraday, Philos. Trans. R. Soc. London. **113**, 160 (1823).

[11] E. G. Hammerschmidt, Ind. Eng. Chem. **26**, 851 (1934).

[12] Y. F. Makogon, *Hydrates of natural gas* Tulsa, Oklahoma, USA, Penwell Books, (1981).

[13] P. G. Brewer, F. M. Orr, Jr, G. Friederich, K. A. Kvenvolden, D. L. Orange, Energy Fuels. **12**, 183 (1998).

[14] O. Mousis, E. Chassefiere, J. Lasue, V. Chevrier, M. E. Elwood Madden, A. Lakhlifi, J. I. Lunine, F. Montmessin, S. Picaud, F. Schmidt, T. D. Swindle, Space. Sci. Rev. (2012).

[15] a) M. v. Stackelberg, Naturwiss. **36**, 359 (1949); b) M. Z. v. Stackelberg, Electrochem. **58**, 104 (1954); c) M. Von Stackelberg, H. R. Müller, J. Chem. Phys. **19**, 1319 (1951).

[16] V. V. Struzhkin, B. Militzer, W. L. Mao, H. K. Mao, R. J. Hemley, Chem. Rev. **107**, 4133 (2007).

[17] G. A. Jeffrey, R. K. McMullan J. Chem. Phys. **37**, 2231 (1962).

[18] K. A. Udachin, G. D. Enright, C. I. Ratcliffe, J. A. Ripmeester, J. Am. Chem. Soc. **119**, 11481 (1997).

[19] J. D. Bernal, R. H. Fowler, J. Chem. Phys. **1**, 515 (1933).

[20] E. D. Isaacs, A. Shukla, P. M. Platzman, D. R. Hamann, B. Barbiellini, C. A. Tulk, Phys. Rev. Lett. **82**, 600 (1999).

[21] Q. Sun, Ti-Yu. Duan, H. F. Zheng, Q. J. Jian, X. Y. Wu, J. Chem. Phys. **122**, 024714 (2005).

[22] A. K. Sum, R. C. Buruss, E. D. Sloan, Jr, J. Phys. Chem. B. **101**, 7371 (1997).

[23] K. C. Hester, R. M. Dunk, S. N. White, P. G. Brewer, E. T. Peltzer, E. D. Sloan, Geochim. Cosmochim. Acta. **71**, 2947 (2007).

[24] W. L. Mao, H.-K. Mao, A. F. Goncharov, V. V. Struzhkin, Q. Guo, J. Hu, J. Shu, R. J. Hemley, M. Somayazulu, Y. Zhao, Science. **297**, 2247 (2002).

[25] W. L. Mao, H.-K. Mao, Proc. Natl. Acad. Sci. **101**, 708 (2004).

[26] D. Y. Koh, H. Kang, J. Jeon, Y. H. Ahn, Y. Park, H. Kim, H. Lee, J. Phys. Chem. C. **118**, 3324 (2014).

[27] A. Hallbrucker, E. Mayer, J. Chem. Soc. Faraday. Trans. **90**, 293 (1994).

[28] D. W. Davidson, M. A. Desando, S. R. Gough, Y. P. Handa, C. I. Ratcliffe, J. A. Ripmeester, J. S. Tse, Nature. **328**, 418 (1987).

[29] M. A. Desando, Y. P. Handa, R. E. Hawkins, C. I. Ratcliffe, J. A. Ripmeester, J. Inclusion Phenom. Mol. Recog. Chem. **8**, 3 (1990).

[30] E. Dartois, Icarus. **212**, 950 (2011).

[31] C. Moon, P. C. Taylor, P. M. Rodger, Can. J. Phys. **81**, 451 (2003).

[32] C. Moon, P. C. Taylor, P. M. Rodger, J. Am. Chem. Soc. **125**, 4706 (2003).

[33] C. Moon, R. W. Hawtin, P. M. Rodger, Faraday Discuss. **136**, 367 (2007).

[34] R. W. Hawtin, D. Quigley, P. M. Rodger, Phys. Chem. Chem. Phys. **10**, 4853 (2008).

[35] G. J. Guo, M. Li, Y. G. Zhang, C. H. Wu, Phys. Chem. Chem. Phys. **11**, 10427 (2009).

[36] M. R. Walsh, C. A. Koh, E. D. Sloan, A. K. Sum, D. T. Wu, Science. **326**, 1095 (2009).

[37] S. Alavi, J. A. Ripmeester, J. Chem. Phys. **137**, 054712 (2012).

[38] M. Uddin, D. Coombe, J. Phys. Chem. A. **118**, 1971 (2014).

[39] M. Hiratsuka, R. Ohmura, A. K. Sum, K. Yasuoka, J. Chem. Phys. **137**, 144306 (2012).

[40] N. Plattner, M. Meuwly, J. Chem. Phys. **140**, 024311 (2014).

[41] S. Patchkovskii, J. S. Tse, Proc. Natl. Acad. Sci. **100**, 14645 (2003).

[42] P. K. Chattaraj, S. Bandaru, S. Mondal, J. Phys. Chem. A. **115**, 187 (2011).

[43] P. Kumar, N. Sathyamurthy, J. Phys. Chem. A. **115**, 14276 (2011).

[44] H. K. Srivatsava, G. N. Sastry, J. Phys. Chem. A. **115**, 7633 (2011).

[45] P. Kumar, B. K. Mishra, N. Sathyamurthy, Comput. Theor. Chem. **1029**, 26 (2014).

[46] X. Cao, Y. Su, Y. Liu, J. Zhao, C. Lu, J. Phys. Chem. A. **118**, 215 (2013).

[47] A. Szabo, S. N. Ostlund, *Modern Quantum Chemistry, Dover Publications, Inc*. (1996).

[48] R. G. Parr, W. Yang, Density Functional theory for atoms and molecules; Oxford University press: New York. (1989).

[49] F. Jensen, *Introduction to Computational Chemistry. 2nd ed.; (John Wiley and Sons Ltd, England)*. (2007).

[50] W. Kohn, A. D. Becke, R. G. Parr, J. Phys. Chem. **100**, 12974 (1996).

[51] P. Hohenberg, W. Kohn, Phys. Rev B. **136**, B864 (1964).

[52] W. Kohn, L. J. Sham, Phys. Rev A. **140**, A1133 (1965).

[53] Y. Wang, Phys. Rev. B. **54**, 16533 (1996).

[54] J. P. Perdew, A. Zunger, Phys. Rev. B. **23**, 5048 (1981).

[55] D. M. Ceperley, B. J. Alder, Phys. Rev. Lett. **45**, 566 (1980).

[56] L. Hedin, B. I. Lundqvist, J. Phys. C. **4**, 2064 (1971).

[57] E. Wigner, Phys. Rev. **46**, 1002 (1934).

[58] A. H. MacDonald, S. H. Vosko, J. Phys. C. **12**, 2977 (1979).

[59] J. P. Perdew, K. Burke, Y. Wang, Phys. Rev. B. **54**, 16533 (1996).

[60] J. P. Perdew, K. Burke, M. Ernzerhof, Phys. Rev. Lett. **77**, 3865 (1996).

[61] A. D. Becke, Phys. Rev. A. **38**, 3098 (1998).

[62] J. P. Perdew, Phys. Rev. B. **33**, 8822 (1986).

[63] A. D. Becke, J. Chem. Phys. **98**, 5648 (1993).

[64] Y. Zhao, N. E. Schultz, D. G. Truhlar, J. Chem. Theory. Comput. **2**, 364 (2006).

[65] Y. Zhao, D. G. Truhlar, Acc. Chem. Res. **41**, 157 (2008).

[66] S. Grimme, J. Comput. Chem. **27**, 1787 (2006).

[67] S. Grimme, J. Antony, S. Ehrlich, H. Krieg, J. Chem. Phys. **132**, 154104 (2010).

[68] M. Dion, H. Rydberg, E. SchrÖder, D. C. Langreth, B. I. Lundqvist, Phys. Rev. Lett. **92**, 246401 (2004).

[69] K. Lee, E. D. Murray, L. Z. Kong, B. I. Lundqvist, D. C. Langreth, Phys. Rev. B. **82**, 081101 (2010).

[70] , B. Peters, A. Heyden, A. T. Bell, A. Chakraborty, J. Chem. Phys. **120**, 7877 (2004).

[71] S. Alavi, K. Udachin, J. A. Ripmeester, Chem. Eur. J. **16**, 1017 (2010).

[72] V. Buch, J. P. Devlin, I. A. Monreal, B. J. Cwiklik, N. U. Aytemiz, L. Cwiklik, Phys. Chem. Chem. Phys. **11**, 10245 (2009).

[73] C. J. Cerjan, W. H. Miller, J. Chem. Phys. **75**, 2800 (1981).

[74] A. Banerjee, N. Adams, J. Simons, R. Shepard, J. Phys. Chem. **89**, 52 (1985).

[75] J. Baker, J. Comput. Chem. **7**, 385 (1986).

[76] G. Henkelman, H. Jonsson, J. Chem. Phys. **111**, 7010 (1999).

[77] P. Bolhuis, D. Chandler, C. Dellago, Annu. Rev. Phys. Chem. Phys. **59**, 291 (2002).

[78] P. Geissler, C. Dellago, P. G. Bolhuis, D. Chandler, Adv. Chem. Phys. **123**, 1 (2002).

[79] R. Elber, M. Karplus, Chem. Phys. Lett. **139**, 375 (1987).

[80] P. Margakis, S. A. Andreev, Y. Brumer, D. R. Reichman, E. Kaxiras, J. Chem. Phys. **117**, 4651 (2002).

[81] S. Fischer, M. Karplus, J. Chem. Phys. **194**, 252 (1992).

[82] P. Y. Ayala, H. B. Schlegel, J. Chem. Phys. **107**, 375 (1997).

[83] G. Henkelman, H. Jonsson, J. Chem. Phys. **113**, 9978 (2000).

[84] G. Mills, H. Jonsson, Phys. Rev. Lett. **72**, 1124 (2003).

[85] H. Jonsson, G. Mills, and K. W. Jacobsen, Classical and Quantum Dynamics in Condensed Phase Simulations, edited by B. J. Berne, G. Ciccotti, D. F. Coker, World Scientific, Singapore, 385-404 (1998).

[86] G. Henkelman, B. P. Uberuaga, H. Jonsson, J. Chem. Phys. **113**, 9901 (2000).

[87] L. R. Pratt, J. Chem. Phys. **85**, 5045 (1986).

[88] L. Xie, H. Liu, W. Yang, J. Chem. Phys. **120**, 8039 (2004).

[89] Gaussian 03, Revision C.01, M. J. Frisch et. al., Gaussian, Inc., Wallingford CT, (2003).

[90] Gaussian 09, Revision C.01, M. J. Frisch, et. al., Gaussian, Inc., Wallingford CT, (2010).

[91] G. Kresse, J. Hafner, Phys. Rev. B. **47**, 558 (1993); G. Kresse, J. Furthmüller, Phys. Rev. B. **54**, 11169 (1996).

[92] R. K. McMullan, G. A. Jeffrey, J. Chem. Phys. **42**, 2725 (1965).

[93] C. Peng, H. B. Schlegel, Israel. J. Chem. **33**, 449 (1993).

[94] C. Peng, P. Y. Ayala, H. B. Schlegel, M. J. Frisch, J. Comput. Chem. **17**, 49 (1996).

[95] a) S. Alavi, R. Susilo, J. A. Ripmeester, J. Chem. Phys. **130**, 174501 (2009); R. Susilo, S. Alavi, I. L. Moudrakovski, P. Englezos, J. A. Ripmeester, Chem. Phys. Chem. **10**, 824 (2009).

[96] N. Bjerrum, Science. **115**, 385 (1952).

[97] D. A. McQuarrie, Statistical Mechanics. 1st ed.; (Viva Books Private Ltd, India). (2003).

[98] R. G. Parr, R. A. Donnelly, M. Levy, W. E. Palke, J. Chem. Phys. **68**, 3801 (1978).

[99] R. G. Parr, R. G. Pearson, J. Am. Chem. Soc. **105**, 7512 (1983).

[100] P. K. Chattaraj, D. R. Roy, Chem. Rev. **107**, PR46 (2007).

[101] M. J. Frisch, Y. Yamaguchi, J. F. Gaw, H. F. Schaefer, J. S. Binkley, J. Chem. Phys. **84**, 531 (1986).

[102] F. Fleyfel, J. P. Devlin, J. Phys. Chem. **92**, 631 (1988).

[103] F. Fleyfel, J. P. Devlin, J. Phys. Chem. **95**, 3811 (1991).

[104] J. A. Ripmeester, S. Alavi, Chem. Phys. Chem. **11**, 978 (2010).

[105] a) P. A. Montano, J. Linton, V. Thieu, Y. J. Halpern, Synchroton. Radiat. **8**, 972, (2001); b) H. Oyama, T. Ebinuma, W. Shimada, S. Takeya, J. Nagao, T. Uchida, H. Narita, Can. J. Phys. **81**, 485 (2003); c) J. A. Ripmeester, in Physics and Chemistry of Ice (Ed.: W. F. Kuhs), RSC Publishing, Cambridge, 59 (2006).

[106] R. M. Barrer, W. I. Stuart, Proc. R. Soc. (London). **A243**, 172 (1958).

[107] R. M. Barrer, D. J. Ruzicka, Trans. Faraday Soc. **58**, 2262 (1962).

[108] R. M. Barrer, A. V. J. Edge, Proc. R. Soc. (London). **A300**, 1 (1967).

[109] W. G. Knox, M. Hess, G. E. Jones, H. B. Smith, Chem. Eng. Prog. **57**, 66 (1961).

[110] A. Vysniauskas, P. R. Bishnoi, Chem. Eng. Sci. **38**, 1061 (1983).

[111] E. D. Sloan, F. Fleyfel, AIChE J. **37**, 1281 (1991).

[112] R. L. Christiansen, E. D. Jr. Sloan, Ann. N. Y. Acad. Sci. **715**, 282 (1994).

[113] W. Smith, T. R. Forester, J. Mol. Graphics. **14**, 136 (1996).

[114] a)L. A. Baez, P. Clancy, Ann. N. Y. Acad. Sci. **715**, 177 (1994); b) M. Ota, Y. X. Qi, JSME Int. J. Ser. B. **43**, 719 (2000).

[115] a) J. F. Huang, L. S. Bartell, J. Phys. Chem. A. **106**, 2404 (2002); b) S. Toxvaerd, J. Chem. Phys. **115**, 8913 (2001).

[116] M. Matsumoto, S. Saito, I. Ohmine, Nature. **416**, 409 (2002).

[117] a) T. Pietrass, H. C. Gaede, A. Bifone, A. Pines, J. A. Ripmeester, J. Am. Chem. Soc. **117**, 7520 (1995); b) D. K. Staykova, T. Hansen, A. N. Salamatin, W. F. Kuhs, Proc. 4th Int. Conf. Clathrate hydrates. 537 (2002).

[118] R. Radhakrishnan, B. L. Trout, J. Chem. Phys. **117**, 1786 (2002).

[119] J. Zhang, R. W. Hawtin, Y. Yang, E. Nakagava, M. Rivero, S. K. Choi, P. M. Rodger, J. Phys. Chem. B. **112**, 10608 (2008).

[120] G. J. Guo, Y. G. Zhang, M. Li, C. H. Wu, J. Chem. Phys. **128**, 194504 (2008).

[121] L. C. Jacobson, W. Hujo, V. Molinero, J. Phys. Chem. B. **113**, 10298 (2009).

[122] L. C. Jacobson, W. Hujo, V. Molinero, J. Am. Chem. Soc. **132**, 11806 (2010).

[123] J. Vatamanu, P. G. Kusalik, Phys. Chem. Chem. Phys. **12**, 15065 (2010).

[124] A. Khan, J. Chem. Phys. **110**, 11884 (1999).

[125] Q. S. Du, D. P. Li, P. J. Liu, R. B. Huang, J. Mol. Graph. Model. **27**, 140 (2008).

[126] C. Y. Geng, H. Wen, H. Zhou, J. Phys. Chem. A. **113**, 5463 (2009).

[127] G. Roman-Perez, M. Moaied, J. M. Soler, F. Yndurain, Phys. Rev. Lett. **105**, 145901 (2010).

[128] Q. Li, B. Kolb, G. Roman- Perez, J. M. Soler, F. Yndurain, L. Kong, D. C. Langreth, T. Thonhauser, Phys. Rev. B. **84**, 153103 (2011).

[129] S. McDonald, L. Ojamae, S. J. Singer, J. Phys. Chem. A. **102**, 2824 (1998).

[130] M. V. Kirkov, G. S. Fanourgakis, S. S. Xantheas, Chem. Phys. Lett. **461**, 180 (2008).

[131] S. Yoo, M. V. Kirov, S. S. Xantheas, J. Am. Chem. Soc. **131**, 7564 (2009).

[132] S. F. Boys, F. Bernardi, Mol. Phys. **19**, 553 (1970).

[133] S. Simon, M. Duran, J. J. Dannenberg, J. Chem. Phys. **105**, 11024 (1996).

[134] K. C. Hester, S. N. White, E. T. Peltzer, P. G. Brewer, E. D. Sloan, Mar. Chem. **98**, 304 (2006).

[135] J. L. Kuo, C. V. Ciobanu, L. Ojamae, I. Shavitt, S. J. Singer, J. Chem. Phys. **118**, 3583 (2003).

[136] V. S. Bryantsev, M. S. Diallo, A. C. T. van Duin, W. A. Goddard III, J. Chem. Theory. Comput. **5**, 1016 (2009).

[137] G. S. Fanourgakis, E. Apra, S. S. Xantheas, J. Chem. Phys. **121**, 2655 (2004).

[138] O. Loboda, V. Goncharuk, Chem. Phys. Lett. **484**, 144 (2010).

[139] R. J. Meier, Vib. Spectrosc. **43**, 26 (2007).

[140] J. van der Elsken, D. W. Robinson, Spectrochimica. Acta. **17**, 1249 (1961).

[141] Q. Huang, Q. Long, B. Zheng, Progress in Chemistry. **19**, 165 (2007).

[142] A. Kudelski, Talanta. **76**, 1 (2008).

[143] M. Schmitt, J. Popp, J. Raman. Spect. **37**, 20 (2006).

[144] P. P. Knops-Gerrits, D. E. De Vos, E. J. P. Feijen, P. A. Jacobs, Microporous Mater. **8**, 3 (1997).

[145] G. Kavitha, C. Narayana, J. Phys. Chem. B. **111**, 7003 (2007).

[146] G. Kavitha, C. Narayana, J. Phys. Chem. B. **111**, 14130 (2007).

[147] M. Motin Seikh, L. Sudheendra, C. Narayana, C. N. R. Rao, J. Mol. Struct. **706**, 121 (2004).

[148] H. Ohno, M. Kida, T. Sakurai, Y. Lizuka, T. Hondoh, H. Narita, J. Nagao, Chem. Phys. Chem. **11**, 3070, (2010).

[149] H. Itoh, K. Kawamura, Ann. N. Y. Acad Sci. **912**, 693 (2000).

[150] J. A. Greathouse, R. T. Cygan, B. A. Simmons, J. Phys. Chem. B. **110**, 6428 (2006).

[151] a) T. H. Dunning, Jr, J. Chem. Phys. **90**, 1007 (1989); b) T. H. Dunning, Jr, K. A. Peterson, A. K. Wilson, J. Chem. Phys. **114**, 9244 (2001).

[152] B. Kolb, T. Thonhauser, Phys. Rev. B. **84**, 045116 (2011).

[153] J. Ceponkus, P. Uvdal, B. Nelander, J. Chem. Phys. **129**, 194306 (2008).

[154] M. A. Ricci, G. Signorelli, V. Mazzacurati, J. Phys. Condens. Matter. **2**, SA183 (1990).

[155] I. M. Svishchev, P. G. Kusalik, J. Chem. Soc. Faraday Trans. **90**, 1405 (1994).

[156] P. E. Blöchl, Phys. Rev. B. **50**, 17953, (1994).

[157] M. T. Kirchner, R. Boese, W. E. Billups, L. R. Norman, J. Am. Chem. Soc. **126**, 9407 (2004).

[158] Y. A. Dyadin, I. S. Terekhova, T. V. Rodionova, D. V. Soldatov, J. Struct. Chem. **40**, 645 (1999).

[159] Y. H. Hu, E. Ruckenstein, Angew. Chem. Int. Ed. **45**, 2011 (2006).

[160] K. A. Lokshin, Y. Zhao, D. He, W. L. Mao, H. K. Mao, R. J. Hemley, M. V. Lobanov, M. Greenblatt, Phys. Rev. Lett. **93**, 125503 (2004).

[161] G. D. Holder, J. L. Stephenson, J. J. Joyce, V. T. John, V. A. Kamath, S. Malekar, Ind. Eng. Chem. Process. Des. Dev. **22**, 170 (1983).

[162] S. X. Zhang, G. J. Chen, C. F. Ma, L. Y. Yang, T. M. Guo, J. Chem. Eng. Data. **45**, 908 (2000).

[163] L. J. Florusse, C. J. Peters, J. Schoonman, K. C. Hester, C. A. Koh, S. F. Dec, K. N. Marsh, E. D. Sloan, Science. **306**, 469 (2004).

[164] H. Lee, J. W. Lee, D. Y. Kim, J. Park, Y. T. Seo, H. Zeng, I. L. Moudrakovski, C. I. Ratcliffe, J. A. Ripmeester, Nature. **434**, 743 (2005).

[165] K. C. Hester, T. A. Strobel, E. D. Sloan, C. A. Koh, A. Huq, A. J. Schultz, J. Phys. Chem. B. **110**, 14024 (2006).

[166] S. Hashimoto, S. Murayama, T. Sugahara, H. Sato, K. Ohgaki, Chem. Eng. Sci. **61**, 7884 (2006).

[167] T. A. Strobel, C. J. Taylor, K. C. Hester, S. F. Dec, C. A. Koh, K. T. Miller, E. D. Sloan, J. Phys. Chem. B. **110**, 17121 (2006).

[168] L. J.; Rovetto, T. A. Strobel, K. C. Hester, S. F. Dec, C. A. Koh, K. T. Miller, E. D. Sloan, Fy Annual Progress Report. 629 (2006).

[169] T. Sugahara, J. C. Haag, P. S. R. Prasad, A. A. Warntjes, E. D. Sloan, A. K. Sum, C. A. Koh, J. Am. Chem. Soc. **131**, 14616 (2009).

[170] P. Yedlapalli, S. Lee, J. W. Lee, J. Thermodynamics. **2010**, 1 (2010).

[171] S. Y. Willow, S. S. Xantheas, Chem. Phys. Lett. **525-526**, 13 (2012).

[172] S. Alavi, J. A. Ripmeester, D. D. Klug, J. Chem. Phys. **123**, 024507 (2005).

[173] K. Katsumasa, K. Koga, H. Tanaka, J. Chem. Phys. **127**, 044509 (2007).

[174] T. J. Frankcombe, G. J. Kroes, Phys. Chem. Chem. Phys. **13**, 13410 (2011).

[175] D. Y. Koh, H. Kang, H. Lee, Chem. Comm. **49**, 6782 (2013).

[176] K. R. Ramya, A. Venkatnathan, J. Phys. Chem. A. **116**, 7742 (2012).

[177] K. R. Ramya, G. V. Pavan Kumar, A. Venkatnathan, J. Chem. Phys. **136**, 174305 (2012).

[178] K. R. Ramya, A.Venkatnathan, J. Chem. Phys. **138**, 124305 (2013).

[179] A. Lenz, L. Ojamae, J. Phys. Chem. A. **110**, 13388 (2006).

[180] F. Sabastianelli, M. Xu, Z. Bacic, J. Chem. Phys. **129**, 244706 (2008).

[181] L. E. Klebanoff, J. O. Keller, Int. J. Hydrogen Energy. **38**, 4533 (2013).

[182] T. A. Strobel, E. D. Sloan, C. A. Koh, J. Chem. Phys. **130**, 014506 (2009).

[183] M. A. S. Zaghloul, M. Celli, N. M. Salem, S. M. Elsheikh, L. Ulivi, J. Chem. Phys. **137**, 164320 (2012).

[184] J. Wang, H. Lu, J. A. Ripmeester, J. Am. Chem. Soc. **131**, 14131 (2009).

[185] F. A. Hamprecht, A. J. Cohen, D. J. Tozer, N. C. Handy, J. Chem. Phys. **109**, 6264 (1998).

[186] G. E. Walrafen, J. Chem. Phys. **36**, 1035 (1962).

[187] J. M. Schicks, J. Erziger, M. A. Ziemann, Spectrochimica Acta Part A. **61**, 2399 (2005).

[188] C. A. Tulk, D. D. Klug, J. A. Ripmeester, J. Phys. Chem. A. **102**, 8734 (1998).

[189] M. W. Wong, Chem. Phys. Lett. **256**, 391 (1996).

[190] J. P. Merrick, D. Moran, L. Radom, J. Phys. Chem. A. **111**, 11683 (2007).

[191] A. D. Buckingham, Proc. R. Soc. London. Ser. A. **248**, 169 (1958).

[192] S. Subramanian, E. D. Sloan, Jr, J. Phys. Chem. B. **106**, 4348 (2002).

[193] A. Giannasi, M. Celli, L. Ulivi, M. Zoppi, J. Chem. Phys. **129**, 084705 (2008).

[194] H. Shoji, C. C. Langway, Jr, Nature. **298**, 548 (1982).

[195] T. Hondoh, H. Anzai, A. Goto, S. Mae, A. Higashi, C. C. Langway, Jr. J. Inclusion. Phenom. **8**, 17 (1990).

[196] H. Lu, J. Wang, C. Liu, C. I. Ratcliffe, U. Becker, R. Kumar, J. Ripmeester, J. Am. Chem. Soc. **134**, 9160 (2012).

[197] Y. A. Dyadin, E. G. Larionov, E. Y. Aladko, F. V. Zhurko, Doklady. Phys. Chem. **378**, 159 (2001).

[198] K. Sugahara, Y. Tanaka, T. Sugahara, K. Ohgaki, J. Supramol. Chem. **2**, 365 (2002).

[199] S. Sasaki, S. Hori, T. Kume, H. Shimizu, J. Chem. Phys. **118**, 7892 (2003).

[200] B. Champagnon, G. Panczer, B. Chazallon, L. Arnaud, P. Duval, V. Lipenkov, J. Raman. Spectrosc. **28**, 711 (1997).

[201] B. Chazallon, W. F. Kuhs, J. Chem. Phys. **117**, 308 (2002).

[202] S. Horikawa, H. Itoh, J. Tabata, K. Kawamura, T. Hondoh, J. Phys. Chem. B. **101**, 6290 (1997).

[203] E. P. van Klaveren, J. P. J. Michels, J. A. Schouten, Phys. Rev. B. **61**, 9237 (2000).

[204] (a) E. P. van Klaveren, J. P. J. Michels, J. A. Schouten, D. D. Klug, J. S. Tse, J. Chem. Phys. **114**, 5745 (2001). (b) E. P. van Klaveren, J. P. J. Michels, J. A. Schouten, D. D. Klug, J. S. Tse, J. Chem. Phys. **115**, 10500 (2001). (c) E. P. van Klaveren, J. P. J. Michels, J. A. Schouten, D. D. Klug, J. S. Tse, J. Chem. Phys. **117**, 6637 (2002).

[205] M. G. E. van Hinsberg, M. I. M. Scheerboom, J. A. Schouten, J. Chem. Phys. **99**, 752 (1993).

[206] S. Ozeki, I. Otsuka, J. Phys. Chem. B. **110**, 20067 (2006).

[207] I. Otsuka, S. Ozeki, J. Phys. Chem. B. **110**, 1509 (2006).

[208] J. Klinger, J. Phys. Chem. **87**, 4209 (1983).

[209] D. W. Davidson, S. R. Gough, Y. P. Handa, C. I. Ratcliffe, J. A. Ripmeester, J. S. Tse, J. Physique. **48**, C1-537 (1987).

[210] A. Hallbrucker, E. Mayer, J. Chem. Soc. Chem. Commun. 873 (1990).

[211] A. Hallbrucker, E. Mayer, J. Chem. Soc. Faraday. Trans. **86**, 3785 (1990).

[212] A. N. Salamatin, V. Y. Lipenkov, T. Ikeda - Fukazawa, T. Hondoh, J. Cryst. Growth. **223**, 285 (2001).

[213] A. N. Salamatin, V. Y. Lipenkov, T. Hondoh, J. Cryst. Growth. **257**, 412 (2003).

[214] A. H. Mohammadi, B. Tohidi, R. W. Burgass, J. Chem. Eng. Data. **48**, 612 (2003).

[215] G. A. Grieves, T. M. Orlando, Surf. Sci. **593**, 180 (2005).

[216] A. H. Mohammadi, D. Richon, Ind. Eng. Chem. Res. **49**, 3976 (2010).

[217] A. Hallbrucker, E. Mayer, J. Chem. Soc. Faraday. Trans. **90**, 293 (1994).

[218] T. Ikeda, H. Fukazawa, S. Mae, T. Hondoh, C. C. Langway, Jr, J. Phys. Chem. B. **101**, 6180 (1997).

[219] K. R. Ramya, A. Venkatnathan, Comput. Theor. Chem. **1023**, 1 (2013).

[220] C. R. Schwalm, A. R. Ek, Forest. Ecol. Mgmt. **150**, 241 (2001).

[221] R. Meyer, F. Joos, G. Esser, M. Heimann, G. Hooss, G. Kohlmaier, W. Sauf, R. Voss, U. Wittenberg, Global. Biogeochem. Cycl. **13**, 785 (1999).

[222] B. Hitchon, W. D. Gunter, T. Gentzis, R. T. Bailey, Energy. Convers. Mgmt. **40**, 825 (1999).

[223] T. Ebinuma, Method for dumping and disposing of Carbon dioxide gas and apparatus therefore. U. S. Patent 5,261,490, 16 November (1993).

[224] K. Ohgaki, K. Takano, H. Sangawa, T. Matsubara, S. Nakano, J. Chem. Eng. Jpn. **29**, 478 (1996).

[225] J. B. Wang, X. Q. Guo, G. J. Chen, Z. Z. Li, L. Y. Yang, J. Chem. Eng. Chin. Univ. **21**, 715 (2007).

[226] H. Lee, Y. Seo, Y. Taek. Seo, I. L. Moudrakovski, J. A. Ripmeester, Angew. Chem. Int. Ed. **42**, 5048 (2003).

[227] J. H. Yoon, T. Kawamura, Y. Yamamoto, T. Komai, J. Phys. Chem. A. **108**, 5057 (2004).

[228] T. Uchida, I. Y. Ikeda, S. Takeya, Y. Kamata, R. Ohmura, J. Nagao, O. Y. Zatsepina, B. A. Buffett, Chem. Phys. Chem. *6*, 646 (2005).

[229] Y. Park, D. Y, Kim, J. W. Lee, D. G. Huh, K. P. Park, J. Lee, H. Lee, Proc. Natl. Acad. Sci. **103**, 12690 (2006).

[230] E. M. Yezdimer, P. T. Cummings, A. A. Chialvo, J. Phys. Chem. A. **106**, 7982 (2002).

[231] P. Dornan, S. Alavi, T. K. Woo, J. Chem. Phys. **127**, 124510 (2007).

[232] L. C. Jacobson, V. Molinero, J. Am. Chem. Soc. **133**, 6458 (2011)

[233] M. R. Walsh, G. T. Beckham, C. A. Koh, E. D. Sloan, D. T. Wu, A. K. Sum, J. Phys. Chem. C. **115**, 21241 (2011).

[234] S. Sarupria, P. G. Debenedetti, J. Phys. Chem. Lett. **3**, 2942 (2012).

[235] P. Pirzadeh, P. G. Kusalik, J. Am. Chem. Soc. **135**, 7278 (2013).